Multi-Fidelity Aerodynamic and Aeroacoustic Sensitivity Study of Isolated Propellers

S. Burger

TU Delft

Multi-Fidelity Aerodynamic and Aeroacoustic Sensitivity Study of Isolated Propellers

by

S. Burger

to obtain the degree of Master of Science
at the Delft University of Technology,
to be defended publicly on Tuesday September 29, 2020 at 14:00.

Student number:	4213971	
Project duration:	March 17, 2019 – September 29, 2020	
Thesis committee:	Dr. ir. T. Sinnige,	TU Delft, supervisor
	Prof. dr. ing. G. Eitelberg,	TU Delft, chairman
	Dr. F. Avallone,	TU Delft
	Dr. R.P. Dwight,	TU Delft

An electronic version of this thesis is available at http://repository.tudelft.nl/.

TU Delft

Preface

I started this thesis project with some ambitious goals that required the use of various tools I had no prior experience with. In order to succeed, many subsequent steps had to be completed successfully before any results could be generated. I'm proud that the goals and objectives that were formulated at the very start of this project have in fact been achieved. I could not have done this on my own. First of all I would like to thank Tomas Sinnige, my daily supervisor, for providing continuous guidance and feedback for the complete duration of this thesis. I would also like to thank Georg Eitelberg for his valuable critical remarks at a later stage of this project.

The finalisation of this thesis not only concludes my Master of Science program, but it also marks the end of a chapter in my life. I'm looking back with joy at the many fond memories I have of the experiences and adventures I've had as a student. I want to thank my friends and roommates for these moments and their support during this thesis and my time as a student in general. A special thanks to everyone from Nuna9, for the friendships and incredible adventures that we have shared. Last but not least, I want to thank my parents for their relentless support and continuous encouragement.

S. Burger
Delft, September 2020

Summary

Despite of the efficiency advantage of propellers over jet engines, the latter has been the most popular propulsive system for decades. Jet engines allowed aircraft to reach higher velocities and altitudes than what was possible with propellers. Propellers do experience a renewed interest due to the global tendency towards sustainable developments and research in electric aircraft. Increasing the efficiency has been a driving factor for propeller blade design, but noise emissions have become more relevant as well. Combined aerodynamic and aeroacoustic studies for propeller blade design have been conducted to a much lesser extent than studies aiming for purely aerodynamic efficiency. As airport regulations regarding noise get stricter, noise reduction should be taken into account during propeller blade design.

The main objective of this thesis is to quantify the dependency between propeller efficiency and propeller noise emissions for an isolated, unducted propeller using a combination of low-order and high-order analysis tools. This objective is met in this study. In this thesis, two methods have been utilised for the flow analysis with a varying level of fidelity. These are a BEM method and a RANS implementation. For the aeroacoustic analysis, the frequency formation by Hanson is used. Next to these analysis tools, a Bezier implementation is used for the parametrisation of blades, and a kriging model is established as surrogate model.

The low order method is a BEM method which deviates from classical methods in the sense that a dependency to sweep is incorporated. Comparisons with RANS simulations show that the method can provide reasonable results, but that strong sweep gradients and large out of plane translation can severely degrade the results. For the high fidelity method, compressible RANS simulations are performed with a Spalart-Allmaras turbulence model. Validation indicates not a perfect agreement with experimental data, especially at higher advance ratios. This discrepancy may partially be caused by the low Reynolds number at which the propeller is operated in the experiment.

The noise is computed using the frequency formulation from Hanson. Notable from verification is that the directivity plots indicate that the blade thickness, or volume, seems to dominate the noise emissions at higher advance ratio. The results from BEM and RANS show reasonable agreement.

In this study, 1000 different random blade designs are generated. Bezier curves are used to parametrise radially distributed blade design variables. A design of experiments is performed to cover as much of the design space as possible within the parameter bounds. In this process, a sobol sequence is used to generate design points. Although the implementation allows for a complete blade to be parametrised, sweep is the only geometrical blade design parameter that is varied in this thesis. The collective pitch angle and advance ratio are the other parameters that are varied in this study.

A partly automated workflow has been created which computes the low and high fidelity propeller characteristics and noise without manual interference. Tedious processes and steps associated with CFD simulations such as meshing, submitting jobs to a computer cluster and processing the results do not require manual input once the workflow has been initiated. This meant that 4324 high fidelity data points and 25116 low fidelity points could be generated in this study.

All generated results are combined into one surrogate model by kriging. Comparing the kriging results with CFD evaluations shows that the average absolute kriging errors for C_T, η and TSSP are $2.19 \cdot 10^{-3}$, $5.40 \cdot 10^{-3}$ and $8.78 \cdot 10^{-1}$ respectively. The average values show excellent agreement, but some outliers were found when selecting some outstanding designs. Despite of this, kriging does show to be able to generate results which closely resemble CFD simulations on blade designs of which no CFD evaluations are provided in the training data. In theory, the kriging model can be used to evaluate blade designs of which also no BEM evaluation has been performed. This, however, is not done in this study. Only blade designs which have at least one BEM data point are evaluated through the kriging model.

Pitch and advance ratio are used in this study to achieve the required thrust. The constant thrust at which blades are compared in this study equals 27N. This value was obtained by ensuring that the Tc of the blade is the same as the Tc of a reference aircraft with propellers. The reference aircraft used is the ATR72-500. For minimum noise, it is beneficial for the Mach number at the tip to be as low as possible. The most counted pitch angle is therefore around 58 degrees, which results in a higher advance ratio than what is seen at the most efficient conditions. Increasing the pitch angle to limit noise emissions reduces the efficiency. A relation between efficiency and noise is found. This relation suggests that for a given blade design, there is a 0.26%

point penalty in efficiency for every dB reduction of noise, or thrust scaled sound pressure, by adjustment of the pitch and advance ratio. The results show that adjusting the pitch and advance ratio could potentially reduce the TSSP by more than 13 dB at the cost of 3.4% point efficiency. This means that the perceived sound can be reduced by more than a factor 2. Electrically propelled aircraft could benefit from this finding in that the operating conditions might be temporarily adjusted when flying in urban areas. Since this usually is only for a short duration, the fuel consumption of the overall flight will not increase much while noise emissions can be reduced when required.

When the advance ratio is fixed, the kriging model indicated a 9 dB difference between the best and worst performing blades for noise. However, performing CFD evaluations on these points showed only a maximum difference of approximately 3 dB for blades at a similar efficiency.

A Pareto front is also visualised for efficiency and noise. This is done by putting the data points of the blade designs operating at their maximum efficiency together with the same blade designs operating at the lowest noise settings. A difference of 19 dB is seen when comparing the most efficient point with the lowest noise point. This reduction of noise results in a 3.89% point reduction in efficiency.

Contents

List of Figures

List of Tables

Nomenclature

a	=	ratio of tip speed to flight speed
a_0	=	speed of sound, m/s
A_j	=	noise amplitude of blade section j
A_R	=	noise amplitude resultant over all blade sections
B	=	number of blades
c	=	chord length, m
C	=	correction factor/tuning factor for convergence in BEM
c_0	=	speed of sound, m/s
C_d	=	drag coefficient
C_f	=	friction coefficient
C_l	=	lift coefficient
C_P	=	$\frac{2\pi Q}{\rho n^2 D^5}$, power coefficient
C_p	=	pressure coefficient
C_T	=	$\frac{T}{\rho n^2 D^4}$, thrust coefficient
dl	=	segment length on a blade corrected for sweep, m
dr	=	radial segment length on a blade, m
D	=	propeller diameter, m
D'	=	drag per unit length, N/m
F	=	prandtl tip loss correction factor
h_i	=	relative grid cell size of grid i
J	=	$\frac{V_\infty}{nD}$, advance ratio
k	=	pressure ratio factor
k_x	=	dimensionless chord-wise wave number
k_y	=	dimensionless chord-wise wave number
l_{chord}	=	chord length, m
L'	=	lift per unit length, N/m
m	=	noise harmonic integer
$\dot{m}$	=	mass flow, kg/s
M	=	Mach number
M_r	=	section relative Mach number
M_t	=	tip rotational Mach number
M_x	=	flight Mach number
n	=	propeller rotational speed, Hz
n	=	degree of Bezier curve
n	=	$m \cdot B$,harmonic of the shaft frequency
n_g	=	number of grids in grid error estimation
$N_{cells,i}$	=	number of cells in grid for grid i
N_b	=	number of blades
p	=	order of convergence
p'	=	accoustic pressure at the far field, Pa
p_0	=	correction to the pressure at the actuator disk, Pa
p^-	=	upstream pressure infinitesimally close to actuator disk, Pa
p'	=	pressure in the wake of a propeller, Pa
p^+	=	downstream pressure infinitesimally close to actuator disk, Pa
p_∞	=	ambient pressure, Pa
p_{ref}	=	reference pressure, Pa
p_{rms}	=	accoustic pressure, Pa
$P_{F_\phi m}$	=	tangential force component of far field pressure harmonic

$P_{F_x m}$	=	axial force component of far field pressure harmonic
P_{mb}	=	total far field pressure harmonic
$P_{n,k}$	=	general far field pressure harmonic
P_{Vm}	=	volume component of far field pressure harmonic
$P_{ambient}$	=	ambient pressure, Pa
P_i	=	i'th control point of Bezier curve
P_s	=	static pressure, Pa
Q	=	torque, Nm
r	=	propeller radius, m
r'	=	radius of propeller wake, m
r_t	=	tip radius, m
R	=	specific gas constant, $\frac{J}{kg \cdot K}$
R	=	total propeller radius, m
Re	=	$\frac{\rho U l_{chord}}{\mu}$, Reynolds number
t	=	time, seconds
T	=	thrust, N
T_0	=	total temperature, K
T_1	=	lower time boundary, s
T_2	=	upper time boundary, s
T_C	=	thrust coefficient
T_s	=	static temperature, K
u_*	=	friction velocity, m/s
u_i	=	i component of velocity, m/s
$\langle u_i \rangle$	=	sum of the mean values of u_i
u_j	=	j component of velocity, m/s
u_n	=	velocity of a fluid normal to the surface, m/s
U	=	absolute velocity, m/s
U_s^*	=	standard deviation when theoretical order of convergence p = 2 is used
U_s	=	standard deviation
v_n	=	velocity of a surface normal to the surface,m/s
v_r	=	upstream or downstream radial velocity depending on + or - superscript, m/s
v_Φ	=	upstream or downstream angular velocity depending on + or - superscript, m/s
V	=	free stream velocity, m/s
V_∞	=	free stream velocity, m/s
w_r	=	induced radial velocity at actuator disk, m/s
w_z	=	induced axial velocity at actuator disk, m/s
w_z'	=	induced axial velocity in the wake of a propeller, m/s
w_Φ	=	induced angular velocity at actuator disk, m/s
w_ψ'	=	induced angular velocity in the wake of a propeller, m/s
$\mathbf{x}$	=	design vector for kriging
y	=	observer distance from the propeller axis
y^+	=	dimensionless height of first inflation layer from surface
$\hat{y}$	=	interpolation result of kriging
$y_{inflationlayer}$	=	height of first inflation layer from surface, m
z	=	axial location in stream tube, m
z	=	r/R, normalised radius
α	=	angle of attack, deg
α	=	grid fitting coefficient
$\beta_{0.7}$	=	collective pitch angle defined at 0.7R
β_i	=	linear regression coefficient for kriging
γ	=	ratio of specific heat of air
Δm	=	maximum difference between computed solutions during grid error estimation
Δp	=	pressure difference across actuator disk, Pa
$\Delta P_{0,gauge}$	=	gauge pressure, Pa
Δp_e	=	equivalent pressure difference across actuator disk, Pa

Δp_l	=	pressure difference between lower surface of an airfoil at a given condition and the pressure on the lower surface of an airfoil at zero lift, Pa
Δp_u	=	pressure difference between upper surface of an airfoil at a given condition and the pressure on the upper surface of an airfoil at zero lift, Pa
ΔV	=	change in velocity with respect to baseline, m/s
δ^*_{RE}	=	estimated grid error when a theoretical order of convergence of p = 2 is used
δ_{RE}	=	estimated grid error
ϵ	=	error tolerance
η	=	$J\frac{C_T}{C_P}$, propeller efficiency
θ	=	radiation angle from the propeller axis to the observer point, deg
θ	=	angle between two vectors, deg
θ_l	=	l'th hyperparameter for kriging
κ	=	input for complete elliptic integrals of the first and second kin
λ	=	midchord sweep, deg
μ	=	dynamic viscosity, $Pa \cdot s$
ρ	=	density, kg/m^3
ρ_0	=	ambient density, $\frac{kg}{m^3}$
σ	=	ratio of section helical speed to flight speed
σ	=	variance
τ_w	=	wall shear stress, Pa
φ	=	induced airfoil angle, deg
ϕ_0	=	estimated exact solution
ϕ_i	=	numerical solution for grid i
ϕ_j	=	phase delay of blade section j
ϕ_o	=	phase delay contribution due to lean
ϕ_{os}	=	combined phase delay contribution due to lean and sweep
ϕ_R	=	resultant phase delay of all blade sections
ϕ_s	=	phase delay contribution due to sweep
ω	=	rotational velocity, rad/s
ω_0	=	stationary phase, 1/deg
Ω	=	propeller rotational speed, rad/s

I

Background

1 Introduction

1.1. Propeller Research Interest

The very first aircraft by the Wright brothers in 1903 used propellers as propulsion. Propellers were the only feasible propulsive system up until the jet engine was engineered in 1941. Although propellers allowed for controlled flights, limitations to the flight velocity and altitude were soon encountered. Jet engines, and later on turbo fans, overcame these drawbacks enabling aircraft to reach higher velocities and higher altitudes. This has made jet engines the most popular type of propulsive system for most civil passenger aircraft and many military aircraft. Reasons for military aircraft to use propellers are amongst others are their robustness in a great range of conditions for take-off and landing, and the low speed performance. There is however another disadvantage of jet engines compared to propellers. A large drawback is the lower fuel efficiency of jet engines compared to propellers. Figure 1.1 illustrates the efficiency of different types of propulsive systems.

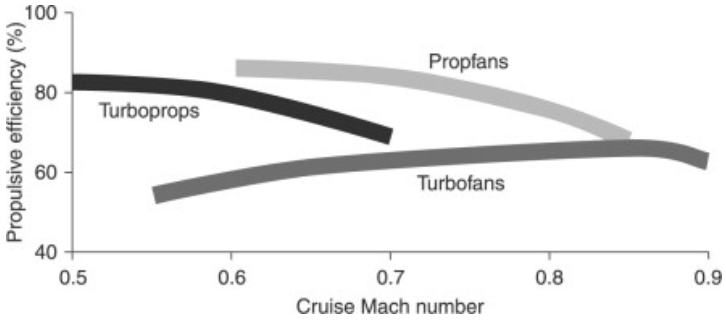

Figure 1.1: Efficiency of different propulsive systems [1]

The efficiency difference between jet engines and propellers can be explained by inspecting the equations for thrust and propulsive efficiency as shown in Equation 1.1 and Equation 1.2 respectively. The thrust is dependent on the mass flow and the velocity increment which is given to the flow. Increasing either of those increases the thrust. As can be seen, it is more beneficial in terms of fuel efficiency to increase the mass flow than to increase the velocity increment, as any increase in velocity increment reduces the propulsive efficiency. With this in mind, jet engines are less efficient compared to propellers by nature as they rely on giving a large velocity increment to a relatively low mass flow, whereas propellers provide a smaller velocity increment to a higher mass flow.

$$T = \dot{m}\Delta V \tag{1.1}$$

$$\eta = \frac{2}{1 + \frac{\Delta V}{V_\infty}} \tag{1.2}$$

Up to the 1970s, fuel was cheap, and due to that, research was focused mainly on forms of jet propulsion. Fuel efficiency was not deemed to be an important topic of research. However, the oil crisis in 1973 pulled

researchers back to propellers. It was around this time that more advanced propeller concepts were investigated which aimed to increase the mass flow while decreasing the velocity increment. Up to the late 1980s, turboprops were developed which combined both propeller blades and jet engines. This allowed for higher bypass ratios, which means the propulsive efficiency was increased compared to conventional jet engines. This research interest faded again in the years at the end of the 1980s as the oil price decreased again.

In the current economic situation and global search to more sustainable developments, research in the field of propeller propulsion systems is experiencing a renewed interest. The efficiency of propellers is unbeaten by jet engines, at least at lower speeds. As blade design methods have improved, new advanced blade designs allow for higher flight velocities for propeller aircraft, which means that one of the large drawbacks of propellers is diminished. The advanced propeller designs typically implement the addition of a varying sweep on the blade. Such blade design has been utilised for example on the Airbus A400M aircraft, shown in Figure 1.2.

Figure 1.2: Airbus A400M with swept blades [1]

Besides the potential fuel-saving possibilities for propeller aircraft, electric propulsion has become a more popular topic for research in the recent years. Drones in all sorts of sizes typically use an electric propulsive system with propellers, and even electrically propelled passenger and transport aircraft are being researched. As the available electrical power may be limited per electric engine, efficient distributed propulsive systems have become a serious subject of investigation. In such aircraft, the thrust would be generated by a series of propellers located on for example the wing. NASA's Maxwell X-57 is an example of such an aircraft in development, of which an artist impression is provided in Figure 1.3.

Figure 1.3: NASA X57 Maxwell artist impression [2]

Although the efficiency and thrust are important design goals, the challenges from noise emissions cannot be underestimated. The same phenomenon which results in thrust, an accelerated flow over a rotating blade, also causes noise. With airport regulations around the world getting stricter, noise emissions should be reduced by design. For military drones, high noise emissions may also be a very unwanted property of

[1] Credits: Julian Herzog, https://commons.wikimedia.org/wiki/File:A400M_outer_engine.jpg
[2] Credits: https://www.nasa.gov/centers/armstrong/news/FactSheets/FS-109.html

propellers due to stealth requirements. One can imagine that with introduction of distributed propulsive systems which include many propellers, the aspect of noise pollution can not be overlooked. Whereas ducted turbofans and pure jet engines can shield some of the generated noise, unducted propellers have no way of shielding the produced noise. For unducted propellers, noise must be reduced by incorporating it as an objective in the blade design, next to thrust and efficiency.

The first attempts on noise predictions were made over 100 years ago, from the 1919's onward [2][3]. Researchers at NASA's Langley have been actively involved in research on aircraft aeroacoustics since the 1930's [4] [2]. The search for better models to predict noise continued, and in 1952 great progression was made by Lighthill when he introduced the concept of the acoustic analogy. Current noise prediction methods still rely on this concept. Lighthill's jet noise formulation was extended in 1969 by Ffowcs Williams and Hawkings. This extension allowed to study the acoustics of rotating machinery, and is known as the Ffowcs Williams-Hawkings equation[2] [4] .

The propeller performance in terms of thrust and efficiency has been, and still is, subject of extensive research. The combined investigation to both aerodynamic and aeroacoustic performance, however, is done to a much lesser extent to the knowledge of the author of this thesis. Examples of such research are from Gur and Rosen [5], Marinus [3] and Pagano et al. [6]. In the above-mentioned research, both the aerodynamic and aeroacoustic effects were computed in various ways. Gur and Rosen [5] rely solemnly on a Blade Element Momentum (BEM) method, while Pagano [6] uses it in conjunction with a another aerodynamic analysis method. Although a BEM method is fast, it does have limitations due to several assumptions that are made. For example, classical BEM implementations cannot account for sweep. Contrary to the fast methods used by Gur and Rosen [5] and Pagano [6], Marinus [3] used a more high-fidelity approach for the aerodynamic computations. Marinus [3] performed Reynolds-Averaged Navier-Stokes (RANS) simulations to create a surrogate model to optimise for noise and efficiency. Although RANS should allows for more variables such as sweep to be taken into account and result in more accurate results, the tools suffered from automatic meshing and convergence failures. This led to only 81 evaluations for the initial model to succeed, while in the subsequent steps only 119 additional designs were processed with 252 originally submitted [3]. This means a failure rate of 53% was encountered, mainly caused by mesh failures.

As more than 30 design variables were used in the research, generally much more successful evaluations are required for satisfactory surrogate model performance. Some of the resulting blades from the research of Marinus and Pagano are shown in Figure 1.4 and Figure 1.5 respectively.

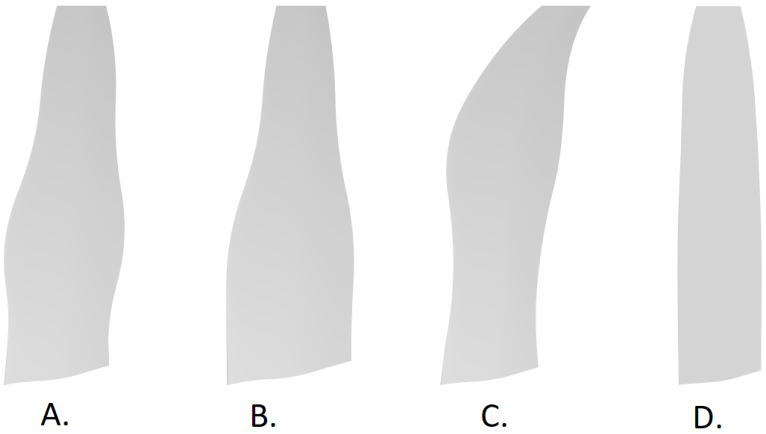

Figure 1.4: Optimised blades by Marinus [3]

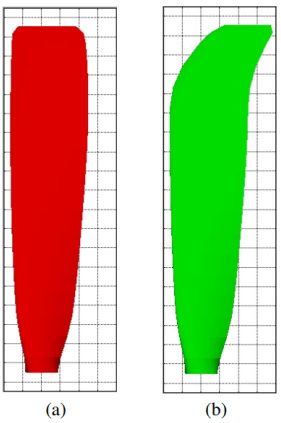

Figure 1.5: Reference blade and optimised blade by Pagano [6]

Regarding the blades from Marinus, each blade is chosen as optimum based on a separate criterion: blade A is the most efficient at multiple advance ratios in cruise and take-off conditions, blade B has the lowest Sound Pressure Level (SPL) in the propeller plane in cruise and take-off conditions, blade C has the best SPL at various receiver locations. All of the optimised blades of Marinus showed better aerodynamic and aeroacoustic performance compared to the benchmark, blade D. The mid chord sweep is low, but a leading edge sweep is obtained by chord and taper differences. All four blades have thin airfoils and high twist angles. The optimised blade of Pagano, blade B in Figure 1.5, also has a high leading edge sweep near the tip, and a smaller chord near the tip compared to the baseline geometry (blade A).

The above-mentioned combined aerodynamic and aeroacoustic research has been carried out between 2008 and 2011. With improved computational resources and tools, this research aims to perform more RANS evaluations with a higher success rate than was seen in for example the research of Marinus [3]. This allows for sweep to be taken into account in the investigation to the relation of propeller noise and performance.

1.2. Thesis Aim and Objectives

Although the propeller was the propulsion type that was used in the very first aircraft, the trade-off between performance and noise is still not understood completely.

The aim of this research is to create a better understanding of the relation between propeller performance and noise for future researchers and blade designers. The main objective is to quantify the dependency between propeller efficiency and propeller noise emissions for an isolated, unducted propeller using a combination of low-order and high-order analysis tools. The following sub-objectives are formulated:

1. Create an automated CFD workflow tool for propeller geometry generation, meshing, flow computation and analysis.
2. Apply this tool to prioritise propeller pitch, sweep and rotational speed on the impact on propeller efficiency and noise.

Quantifying the dependency between propeller efficiency and noise emissions and prioritising propeller parameters will provide novel understanding in the field of propeller design. The main research question is:

"What is the quantified dependency between propeller efficiency and propeller noise emissions for an isolated, unducted propeller?"

To aid in the completion of the objectives, the following smaller sub-questions are formulated:

1. What is the impact of propeller pitch, sweep and rotational speed on the propeller efficiency and noise?
2. How does the output of the multi-fidelity model compare to the output of a RANS evaluation on the same design vector(s)?

Important to note is that this study only comprises aerodynamic and aeroacoustic aspects of propeller design. Structural constraints and limitations are ignored in this study.

1.3. Thesis Outline

This report is divided into four parts, as is visualised in Figure 1.6. Part I discusses the background starting with an introduction, followed by an overview of the basics of aerodynamics and aeroacoustics in chapter 2. That chapter also includes the decisions for selecting which methods are used in this study for aerodynamic and aeroacoustic analysis, and lists other related past studies. In Part II, the implemented tools used in this study are described, first, followed by a description of the complete workflow. In chapter 3, the implemented low fidelity BEM method is explained. chapter 4 then discusses how the higher fidelity RANS method is implemented. The noise implementation is elaborated on in chapter 5. The implementation of the blade parametrisation is discussed in chapter 6. An elaboration on the use of a kriging model is provided in chapter 7. A description of the complete workflow is given in chapter 8. In this workflow, all tools that have been discussed are combined. In Part III, the numerical results are discussed. The verification and validation of all tools is elaborated on in chapter 9. After the errors of the tools are known, the aerodynamic and aeroacoustic results for various blade designs are investigated in chapter 10. This work is concluded in Part IV, in chapter 11. Next to conclusions of the presented work, recommendations are also provided in this chapter.

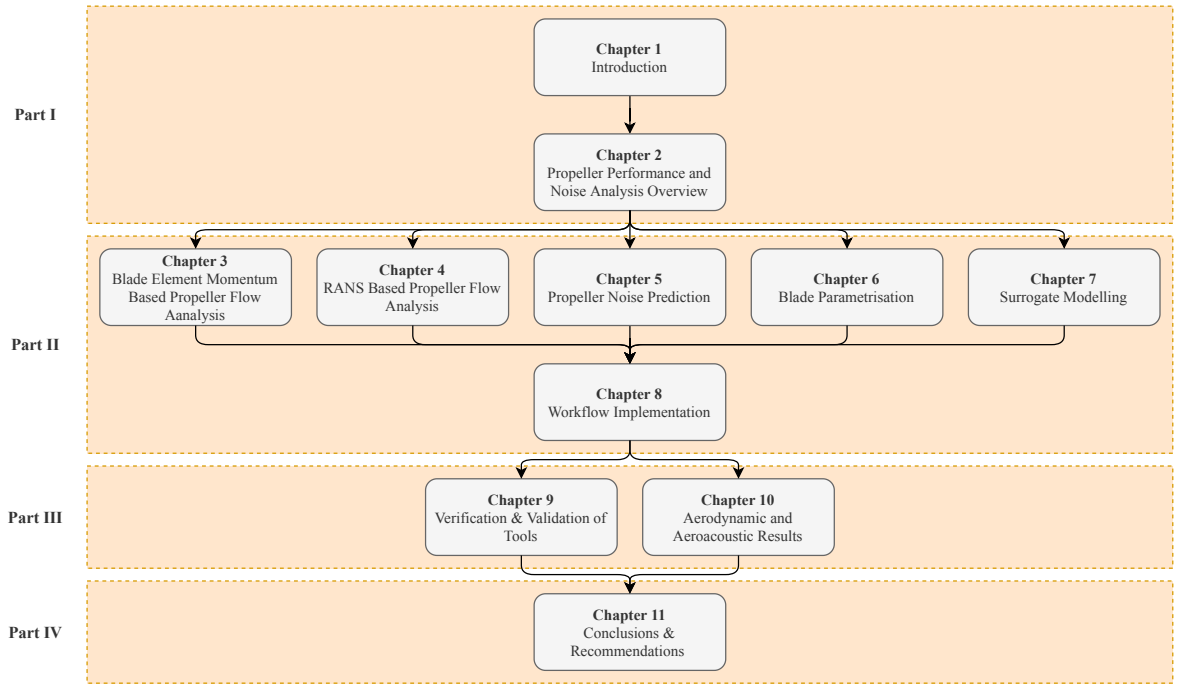

Figure 1.6: Thesis outline

2

Propeller Performance and Noise Analysis Overview and Method Selection

Preceding the in-depth analysis and discussion of the investigation on propeller efficiency and noise, some basics on propeller performance and noise theory are provided and past studies are shortly discussed. The basic aerodynamic flow and forces on propeller blades are discussed in section 2.1, while more on the noise generation and noise sources can be found in section 2.2. Some relevant previous work on propeller optimisation for high efficiency and low noise is provided in section 2.3. Most background information in this chapter is in fact summarised from a previously conducted literature study [7].

2.1. Propeller Performance Background

This section covers basic propeller theory, as well as a discussion on which methods are selected to be used in this research to analyse the performance. Many different methods can be used to predict the propeller performance. The selecting a method mainly depends on whether the assumptions used are acceptable for the intended research and the required computational resources. Basic propeller background information is provided first, followed by a discussion on the selection of a lower and higher fidelity propeller performance analysis method.

2.1.1. Basic Propeller Theory

The main purpose of propellers is to propel aircraft in a forward flight direction. The blades of a propeller can be viewed as a radially distributed set of airfoil sections, similar to the airfoil shape of wings. When rotating the propeller, two force components may be distinguished: axial forces, commonly referred to as thrust, and tangential forces.

When looking at blade sections, the traditional aerodynamic decomposition of forces can also be made, distinguishing the lift and drag components. Essentially, by rotating the blades, the same aerodynamic effects come into play as with wings. Due to the curvature and shape of the blade, a pressure difference is created when accelerating flow around the blades. This pressure difference translates into lift and drag forces. These are affected by the pitch and twist angles of the cross-section, but also by the airfoil shape and thickness. Cross-sectional parameters are usually distributed radially, and vary per location along the radius. This also results in varying forces along the radius of the blade.

Figure 2.1 presents a 2D cross-section of a propeller blade. The lift and drag components are visualised. In this figure, the angle of attack is denoted by α, the inflow angle by ϕ, the airfoil pitch angle by θ and the axial, tangential and radial local induced flow velocities represented by w_z, w_ψ, w_r. The local sweep angle is also depicted by Λ, more on this can be found in chapter 3.

Due to the radial displacement of air by the spinner and the varying pressure along the radius, the flow around propeller blades is actually three dimensional in nature [3]. Also shocks can commonly appear in transonic conditions [3]. The three dimensional structures in the flow such as vortices have a clear impact on propeller performance. Leading edge and tip vortices are shown in Figure 2.2 and Figure 2.3 respectively.

Thrust is a requirement during propeller design, and the thrust and power coefficients can be useful for non-dimensional comparisons and efficiency computation. The thrust and power coefficients are obtained

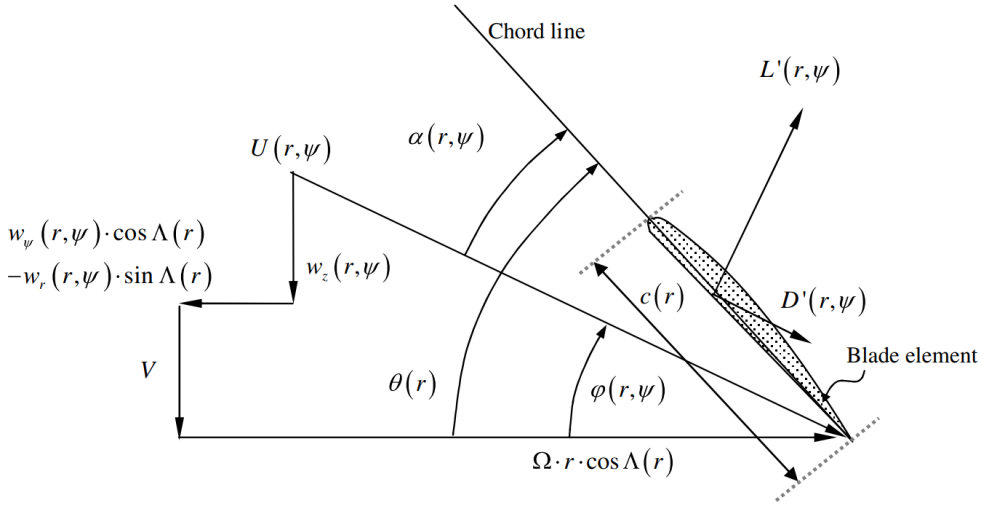

Figure 2.1: Propeller blade airfoil cross-section including angles due to induced velocities [8]

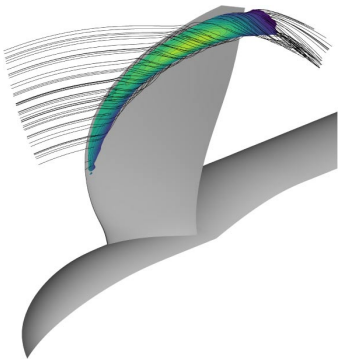

Figure 2.2: Leading edge vortex at swept blade [9]

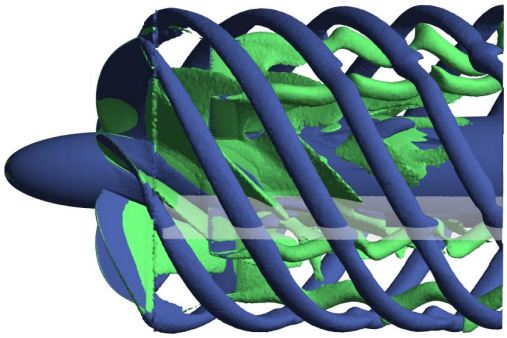

Figure 2.3: Tip vortices [9]

as seen in Equation 2.1 Equation 2.2:

$$C_T = \frac{T}{\rho n^2 D^4} \tag{2.1}$$

$$C_P = \frac{2\pi Q}{\rho n^2 D^5} \tag{2.2}$$

The density is dependent on the operating condition, while n, the rotational speed, may be fixed or variable during the design process. The diameter D naturally is a design variable. Thrust is denoted by T, while the torque is denoted by Q.

Propeller efficiency is the most commonly used performance indicator for propellers in literature. The efficiency can be be determined by comparing the shaft power with the generated thrust. The theoretical propeller efficiency is determined using Equation 2.3. In this formulation, the efficiency is dependent on advance ratio J and the thrust and power coefficients. The used symbols have the same meaning as for Equation 2.1. V represents the free stream velocity.

$$\eta = J\frac{C_T}{C_P} = \frac{V_\infty}{nD}\frac{C_T}{C_P} \tag{2.3}$$

The advance ratio is a non-dimensional relation between the rotational speed of the propellers and the free stream velocity. The advance ratio is more of a operating parameter than design parameter, as it can be tuned to obtain a specified thrust after a blade design has been defined. In this study the a range of advance ratios is computed for each blade design to obtain the blade characteristics.

2.1.2. Propeller Performance Prediction Method Selection

Various methods for performance prediction are available. The main trade-off for method selection usually is about accuracy and computational time. Three dimensional CFD methods are more expensive, but can capture more flow phenomena than two dimensional based methods. The vortices shown in Figure 2.2 and Figure 2.3 are captured using Reynolds-Averaged Navier-Stokes (RANS) simulations, but cannot be predicted by for example a Blade Element Momentum (BEM) theory method. As in this research, the results from both a higher and lower fidelity method will be combined, the limitations imposed by a lower fidelity method may be acceptable whereas these limitations may not be acceptable when solemnly relying on the lower fidelity method.

When computing the flow properties over a propeller blade, a large difference between various methods is how turbulence is computed or approximated. Turbulence can be undesired as it increases the wall friction, and thus drag. However, turbulence has also the characteristic to delay flow separation. Turbulent flows need to be solved in three dimensions as they break away of symmetry. These flows are also unsteady, rotational and viscous. It should be evident to the reader that due to the above-mentioned characteristics of turbulent flows, solving for this phenomenon may be computationally expensive. Low fidelity methods cannot solve this directly, due to the various assumptions such as inviscid flow and irrotational flow. There may be (empirical) approximations available to correct for certain flow characteristics over an airfoil, but if one requires to have detailed insights in the effect of turbulence on the wake characteristics, high(er) fidelity methods are required.

The choice for the low fidelity method is discussed first, followed by a discussion on the choice for the high fidelity method and the volume discretisation method required the CFD analysis.

2D-Based Low Fidelity Propeller Flow Performance

One important criterion for the lower fidelity method in this research is that it should be computationally fast. A lower accuracy due to assumptions being made is acceptable, as long as all design parameters can be taken into account. The actuator disk theory, although this method allows for almost instantaneous computations, is rejected as it is deemed inadequate for the intended research. The method simply does not allow for the various blade geometry parameters to be taken into account.

Other methods that are considered are the Blade Element Momentum theory (BEM), the lifting line method or the Vortex Lattice Method (VLM). According to Branlard [10], the computational time of BEM is in the order of seconds, while the computational time of the lifting line theory typically is in the order of minutes, and VLM is slightly more expensive then the lifting line theory. BEM allows for many geometrical parameters to be taken into account, but does require corrections for tip and hub loss on the blade. In a comparison of a BEM model with several lifting line theory variations, it is said that the BEM model "generally shows very good agreement with the test results" [11]. This gives reason to believe that the extended computational time from the other methods does not necessarily lead to better results. As the BEM method is also used in similar research already [5] [6] and thus proven to work well, BEM is the preferred method of choice to complement the higher fidelity method selected in the next subsection.

An important remark is that classical BEM implementations do not allow for sweep to be taken into account. As this parameter has not been investigated well in other research, indicated in section 2.3, it is the intention to include this parameter in this research. For this reason, a more elaborate BEM approach is implemented which does include a dependency to sweep. The implemented BEM model is based on the research by Rosen and Gur [8]. Although this approach increases the computational time slightly, to the order of 10 seconds, this still is much lower than the required time for lifting line methods. The complete implementation is explained in chapter 3.

3D-Based High Fidelity Propeller Flow Performance

A run time of several hours for the high fidelity method for propeller flow determination is deemed acceptable by the author of this study. Although this is much longer than the allowed run time for the lower fidelity method, this constraint already limits the possibilities of high fidelity methods to either the Euler or Reynolds-Averaged Navier-Stokes (RANS) CFD methods. More accurate solutions would be obtained by Direct Numerical Simulation (DNS) and Large Eddy Simulations, but since these methods are much more computationally expensive than RANS or Euler methods [12] [13], these are not considered to be feasible for this study.

With RANS, all turbulence is modelled instead of simulated, which reduces the computational time. Euler simulations would be even faster, but using Euler equations does not allow for viscous effects to be taken into account. Since trial and error showed that the time required for RANS to be in the acceptable order of several

hours, this method is selected to be used in this research. Regarding the turbulence model, several options are are available for both one equation models and two equation models. One equation models are generally faster than two equation models, but can be less accurate. Comparisons between various models [14][15] show that two-equation models do not necessarily perform better than a one-equation model as Spalart-Allmaras (SA), while they are computationally more expensive. Due to this, the SA turbulence model is the turbulence model of choice in this research.

2.2. Propeller Noise Background

This section describes the background on noise sources and theory first, followed by a short description of how sweep can reduce noise. The section is concluded by a discussion on noise prediction methods.

2.2.1. Propeller Noise Sources

Pressure differences over a propeller blade, caused by rotating the blade, do not only result in thrust and torque, but also in noise emissions. The fluctuation in pressure is what is perceived as noise, and it is propagated through air. Although propeller performance is generally measured through its aerodynamic propulsive efficiency, noise emissions are an unwanted side effect. Propeller noise can be divided into three categories: harmonic noise, broadband noise and narrow-band random noise [16].

As the name suggests, harmonic noise is periodic in nature, repeating at a constant rate in time. The fundamental frequency Bn is found by multiplying the number of blades B with rotational speed n. From this, one can see that the blade-passage period equals $\frac{1}{Bn}$ [16]. The pulses are generated at integer multiples, which is to say 1,2,3,4..., of the fundamental frequency Bn.

Broadband noise is random and does not happen at periodic intervals. Broadband noise is also not bound to a specific frequency, but it emits at the complete range of frequencies. Narrow-band random noise is pseudo periodic. The noise frequencies are not as isolated as is the case with harmonic noise, but more grouped than broadband noise. The harmonic, or tonal, noise and broadband noise spectra are shown in Figure 2.4. In this case, the y-axis shows the Sound Pressure Level (SPL), which represents a log ratio of the generated acoustic pressure and an arbitrary reference pressure. The frequency is presented on the x-axis. The various noise sources are discussed next.

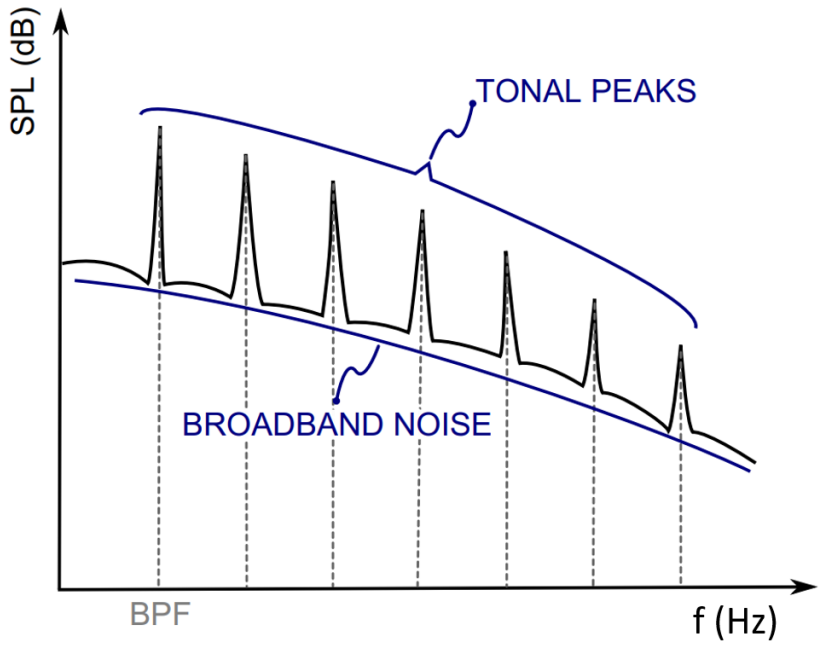

Figure 2.4: Typical Propeller Noise Spectrum [3]

Steady Sources

Steady sources are generated by the rotation of the propeller blades and are periodic in nature. Steady noise sources can be divided into the following categories:

- **Thickness Noise**
  Thickness noise is generated by the displacement of a fluid, in this case air, by the volume of periodically passing propeller blades [16]. This noise type has a monopole source pattern [3], and is more pronounced at increasing Mach numbers. During design, this noise is affected by sweep and blade thickness.

- **Loading Noise**
  Loading noise is a consequence from the lift and drag forces on blade elements caused by the acceleration of the fluid due to the motion of the propeller blades. This noise has a dipole type directivity pattern [16] [3].

- **Quadrupole Noise**
  The quadrupole noise effects are the viscous and propagation effects which are not accounted for by the thickness noise source and loading noise source. This noise source increases for unswept propeller blades with high tip speeds [16]. Marinus [3] notes that neglecting quadrupole sources negatively affects the optimisation routine for a free stream velocity of M = 0.75.

Linear sources from the thickness and loading noise types are dominant at moderate blade velocities. At higher blade section velocities, from transonic onward, the non-linear effects increase and may have to be accounted for [16].

Unsteady Noise

Unsteady sources include, but are not limited to, periodic variation and change of the blade loading. When the angle of attack is non-zero, the propeller blades experience a cyclic or periodic change in the angle of attack over the blade sections. This results in a fluctuating blade loading during each revolution of the propeller blades. This unsteady loading noise is therefore periodic. The occurrence of this noise is generally bound to the harmonics of the Blade Passing Frequency (BPF) [16]. The unsteady loading noise can either increase or reduce noise from the steady-loading noise, depending on the relative location between the loading disturbance and the observer [16].

Aerodynamic interaction which causes unsteady noise is more pronounced at low-speed. The steady sources become dominant at higher speeds. Unsteady noise sources may become more important in the future when electric aircraft are designed with highly integrated propulsive systems.

Unsteady noise sources due to non-zero angles of attack would require flow analysis of the complete propeller in full motion, as it breaks away form axisymmetry. In this study, axisymmetry is used to lower the computational CFD time. Unsteady noise sources are therefore neglected.

Broadband Noise

As written before, broadband noise covers a wide range of frequencies, and is not periodic in nature. The following broadband noise types can be distinguished:

- **Leading Edge Noise**
  The inflow of turbulent flow causes leading edge noise. The interaction between turbulent vortices and the leading edge causes the passing vortices to be modified. The higher the upstream turbulence, the more dominant this noise becomes. Due to the random nature of turbulence, this noise is random as well. The leading edge radius affects this noise type.

- **Trailing Edge Noise**
  Trailing edge noise is related to the boundary layer and wake turbulence and thickness. The modification of vortical structures causes this noise.

- **Blade-Tip Vortex Shedding**
  A similar mechanism as the trailing edge noise causes noise at the blade tips. The interactions of blade-tip vortices with the trailing edge result in additional noise.

According to [17][16], broadband noise does not contribute as much to the total noise as for example harmonic noise during flight for typical aircraft. In this study, therefore only the periodic noise is computed.

2.2.2. Noise Source Reduction due to Sweep

Since sweep is the geometrical blade design parameter that is investigated in this study, this section shortly elaborates on a conceptual mechanism that can lead to noise reduction due to the application of sweep. Sweep can cause the loading distribution over the blade to shift away from the tip, which can reduce the noise. However, there is another mechanism which can lead to noise reduction.

The application of sweep can reduce noise due to the mechanism of phase lag as illustrated in Figure 2.5 [16]. Considering one harmonic at a time, noise on each section of the blade can be described by A_j and phase ϕ_j at each section. By summing all contributions of each section, the total noise is obtained. The mathematical description is provided in Equation 2.4, which uses the notation from Figure 2.5. As is illustrated in the figure, summing the components with a varying phase lag causes phase interference effects which can positively affect the total noise emissions of the blade.

$$A_R \exp\left(i\phi_R\right) = \sum_{j=1}^{N} A_j \exp\left(i\phi_j\right) \tag{2.4}$$

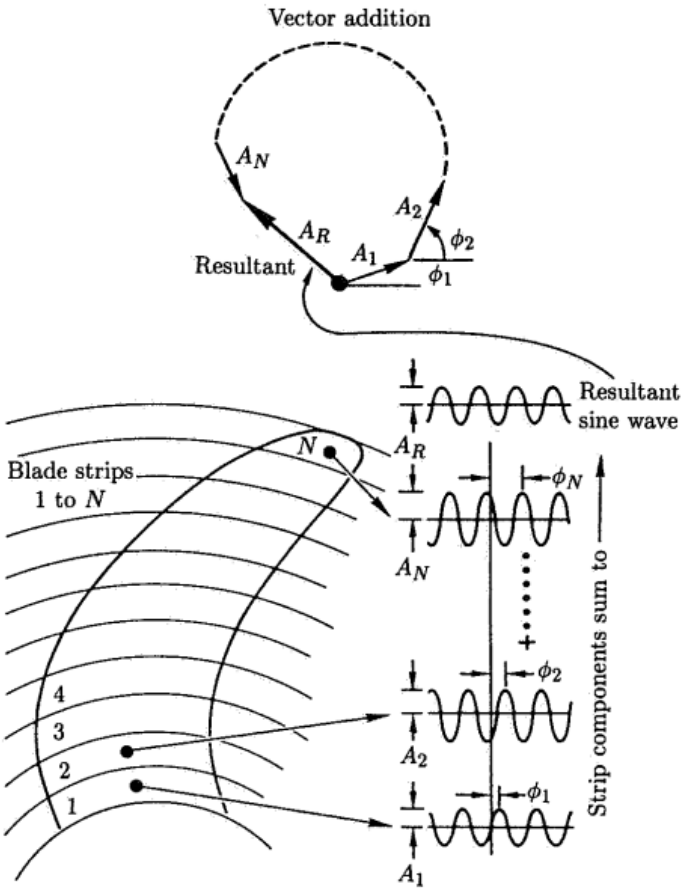

Figure 2.5: Illustration of noise reduction due to blade sweep [16]

2.2.3. Propeller Noise Prediction Method Selection

In this section, the noise prediction method is selected. Two methods are available. First the fundamentals of the methods is shortly discussed, follow by an explanation of the two methods.

The acoustic analogy from Lighthill effectively decouples the noise generation problem from the noise propagation problem. This allows to separate the aerodynamic analysis and the aeroacoustic analysis. Sound is seen as waves which weakly propagate in a compressible fluid. The FW-H equation is obtained by manipulating the the equations for momentum of conservation, continuity and the Navier-Stokes equation, as explained in [3]. The result of this derivation is presented in Equation 2.5 [18].

$$\begin{aligned}\frac{1}{a_0^2}\frac{\partial^2 p'}{\partial t^2} - \nabla^2 p' = &\frac{\partial^2}{\partial x_i \partial x_j}\left\{T_{ij}H(f)\right\} \\ &- \frac{\partial}{\partial x_i}\left\{\left[P_{ij}n_j + \rho u_i(u_n - v_n)\right]\delta(f)\right\} \\ &+ \frac{\partial}{\partial t}\left\{\left[\rho_0 v_n + \rho(u_n - v_n)\right]\delta(f)\right\}\end{aligned} \tag{2.5}$$

In Equation 2.5, u_i represents the velocity of the fluid in the x_i direction and u_n is the velocity of the fluid normal to the surface, where $f = 0$. v_i is the velocity of the surface in the x_i direction, v_n is velocity of the surface normal to the surface. The Dirac delta, $\delta(f)$, and the Heaviside, $H(f)$, are also introduced. The function f is zero on the surface of the body [3]. The acoustic pressure at the far field is represented by p', while a_0 and ρ_0 are the speed of sound and the density in the undisturbed freestream. T_{ij} is Lighthill's stress tensor, and the compressive stress tensor is denoted by P_{ij}. The first term at the right hand side of Equation 2.5 is the quadrupole source term, this quadrupole source accounts for non-linear effects. The loading source term, the dipole, is represented by the second term on the right hand side. The thickness source term, or the monopole, is described by the last term. The time and frequency domain are shortly covered below.

Metzger [2] lists various advancements and derivations on noise prediction, of which most are based on the FW-H equation. Two notable advancements are made by Farassat and Hanson. Farassat describes various formulations, based on work of many others and with help of others, in the time domain [4] [16]. Hanson's formulas cover the frequency domain [16].

Time-Domain Formulation

Since 1975, Farassat has published about multiple formulations for noise prediction [4] [19]. Farassat takes on the time-domain approach for solving Equation 2.5. A general expression is found by applying a convolution of source distributions and free-space Green's functions [3] [20]. Several formulations have been derived, of which some are faster but have more limitations than others. For more information regarding the derivation of the formulations, and for applying Green's functions, see Farassat's elaborate explanation [20].

Frequency-Domain Formulation

One can avoid looking at retarded time blade positions and derivatives by transforming to the frequency domain instead of looking in the time domain [16]. Hanson's extension to include properties such as thickness, sweep and forward flight is explained in [16]. A large advantage is that this method does not require time-accurate solutions, which saves a considerable computational cost. This method only requires the aerodynamic loading to be known, after which the noise radiation can be computed [16]. Both results from low fidelity and high fidelity methods can be used, as long as sections along the blade span can be evaluated separately.

The time-domain formulation poses an additional computational burden, as time-accurate solutions are required. Due to this, the frequency-domain method by Hanson is favoured over the time-domain method. The frequency-domain method does make use of the thin-blade assumption, and is therefore not correct for any arbitrary (thick) shape. For this research, this assumption poses no problems. The frequency domain formulation is covered in detail in chapter 5.

2.3. Previous Work on Propeller Optimisation for High Efficiency and Low Noise

This section shortly lists previous studies conducted in the field of multi-objective propeller optimisation for high efficiency and low noise. This is meant to put the proposed research of this thesis into perspective.

In 1985, Miller [21] developed a preliminary design tool for the combined optimisation of noise and efficiency. A vortex lattice method is used for the aerodynamic analysis, while a noise formulation in the time-domain is used to predict the noise emissions. Using this method, twist, chord and sweep are optimised. The application of sweep is mentioned as an effective noise reduction method.

A study from Gur and Rosen [5] in 2008, mentioned already in the introduction, utilises a BEM method in an aerodynamic and aeroacoustic optimisation routine. The chord length, pitch and blade thickness are varied amongst others. Structural constraints are used as well. Structural constraints are not applied in this thesis.

In another study from 2008, Pagano [6] performed a multidisciplinary optimisation using a BEM method in conjunction with a physics-based surrogate model based on the full potential equation called HELIFPFX. It is mentioned that robustness problems were encountered in the grid generation for this model.

The dissertation from Marinus [3] from 2011 describes a multidisciplinary optimisation of propeller blades in which aerodynamics, aeroacoustics and aeroelastics are combined. As mentioned before, structural aspects are not taken into account in this thesis. As mentioned in the thesis introduction, Marinus used a RANS implementation for the aerodynamic analysis, and used the results to create a surrogate model. The surrogate model was used in the optimisation routine. Unfortunately, the implemented CFD process suffered from a high failure rate of 53%. Both the use of a RANS implementation and the use of a surrogate model are aspects that are also used in this thesis. However, this thesis also includes a sweep sensitive BEM method to create more data points. The results from Marinus were already touched upon in the introduction, and shown in Figure 1.4.

A 2015 study by Wisniewski [22] investigates how to design small propellers for high efficiency and low noise. A blade is designed using low order methods, and then tested in a wind tunnel experiment. Parameters that are discussed include the chord length, pitch angle and blade rotations per minute (RPM).

In a 2019 paper by Ingraham [23], a multi-objective optimisation is performed using NASA's Langley's Advanced Noise Prediction Program and for noise prediction and a BEM implementation for the aerodynamic computations. Various parameters are investigated in an optimisation routine to investigate the trade-off between noise and performance efficiency. The results, however, do seem to be flawed since the presented propeller efficiencies are in the order of high 90% efficiency, approaching almost 100% efficiency. This is shown in Figure 2.6.

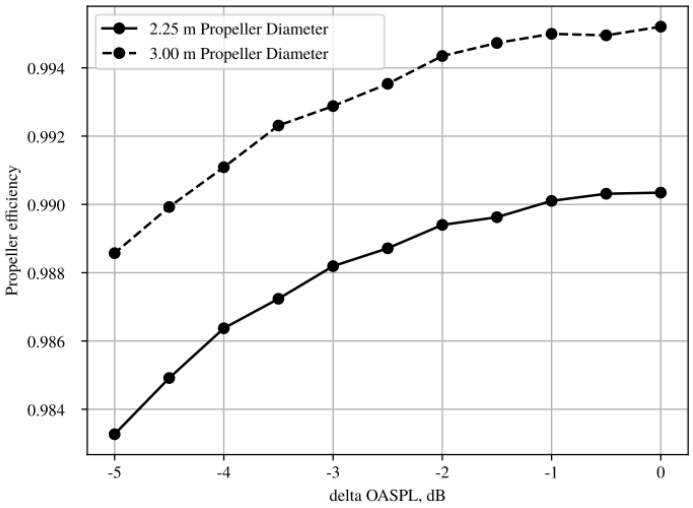

Figure 2.6: Propeller efficiency vs noise plot from Ingraham [23] with questionably high efficiency

An aerodynamic and aeroacoustic optimisation study by Yu et al. published in 2020 uses a RANS implementation for the aerodynamic analysis to create data points to establish a kriging surrogate model. While maintaining the efficiency of a reference blade, a noise reduction of 5 dB was achieved by altering the sweep, chord, twist and thickness of the blade. The initial blade and optimised blade are shown in Figure 2.7. In the figure, chord differences are visible between the original and optimised blade. These changes in the chord do result in trailing edge and leading edge sweep, but the mid chord sweep appears to be mostly unaltered.

In the various studies listed in this section, only a few use a RANS implementation for the aerodynamic analysis. Most studies utilise low order methods, such as BEM methods. Due to the inability of many low order methods to take into account sweep, this parameter is not fully investigated yet for aerodynamic and aeroacoustic blade design. It can be concluded that the proposed research is novel regarding both the investigation of sweep and the multi-fidelity approach. In the coming chapters, the tools used in this study are described.

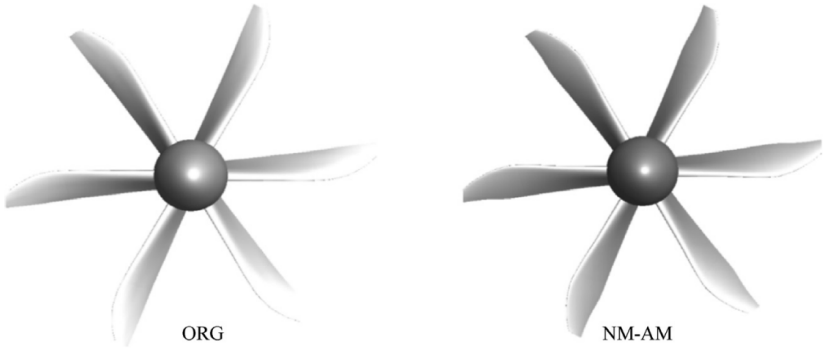

(a) Initial propeller (b) Optimized propeller

Figure 2.7: Comparison of initial propeller and optimised propeller from a study by Yu et al.[24]

II

Research Tools

3

Blade Element Momentum Based Propeller Flow Analysis

The blade element momentum (BEM) theory method is fast but has its limitations. As the solutions of the BEM analysis are combined with higher order CFD simulations, most simplifications are acceptable. However, it is required that the BEM solution shows at least a dependency or sensitivity to sweep. To overcome the limitation of the more standard BEM analysis methods which do not take into account any notion of sweep, a more novel BEM approach was implemented. In this chapter the implementation of the BEM model is discussed, along with the verfication and validation. First, more general information about BEM methods is provided in section 3.1 along with the assumptions made. Thereafter, the specific BEM implementation used in this research is discussed in section 3.2. The verification and validation of this method is elaborated on in chapter 9.

3.1. General Theory

The BEM theory is commonly used in applications for wind turbine and propeller analysis. Before the BEM implementation of this research is discussed, a short general description of the method is provided. The Blade Element Momentum theory combines two theories, namely the momentum theory and the blade element theory.

Actuator Disk Theory

The Actuator Disk Theory is also known as the classical momentum theory. In this theory, a stream tube through an ideal actuator disk, such as a propeller, is considered. This theory was introduced by Rankine in 1865 [25]. A sketch of the stream-tube used in this research is shown in Figure 3.1. A uniform velocity and static pressure are assumed across the actuator disk.

Regarding the stream-tube, the delta in flow momentum of the flow upstream compared to the flow in the slip-stream which has passed through the ideal actuator disk is equal to the thrust of the actuator disk. Assuming an inviscid, incompressible and irrotational flow, Bernoulli's equation can be utilised to compute the pressure and velocities. As the propeller is modelled as an ideal actuator disk with uniform loading, this method does not allow parametrized geometries of various propellers to be used. The 2D representation is very fast to compute, but is inadequate to be used for the analysis of propeller performance computation. To summarise, the four main assumptions are as following [26]:

- The flow is inviscid;
- The flow is incompressible;
- The flow is irrotational;
- There is a uniform velocity profile across the disk and stream-tube;

Blade Element Momentum Theory

As mentioned before, the Blade Element Momentum theory combines the momentum theory and the blade element theory. The uniform loading which was assumed in the Actuator Disk theory is discarded, and instead the blade is divided into separate elements across the radius. This allows to take into account the geometry of the blade and the corresponding flow characteristics.

The thrust and torque of each blade section can be computed when, according to [26], it is assumed that that each blade section does not interact with the other blade sections, and that the two dimensional lift and drag determine the forces of the flow stream on the separate elements of the blade. The momentum balance can be applied to both the axial and angular momentum.

Tip and root losses are not taken into account due to two dimensional nature of the analysis of the blade element momentum theory. A Prandtl loss correction is often applied to correct the effect of induced velocity by the vortices that are being shed. A more elaborate explanation with all equations involved can be found in [26].

Most BEM analysis methods do not account for any sweep. As sweep is one of the investigated parameters in this research, a classic BEM implementation would therefore not suffice. The method proposed by Rosen and Gur [8] adds a radial velocity term which allows for sweep to be taken into account. This radial velocity term is not found in the more classic BEM formulations. The BEM formulation including sweep was implemented using [8] and [11], both being research from Rosen and Gur. As there was no such implementation available to the researcher, the method was coded from scratch in MATLAB. In the next sections the implementation of the formulation is shown. For a more detailed explanation, the reader is referred to the previously mentioned original research by Rosen and Gur.

3.2. BEM Implementation Including Sweep

The BEM implementation including sweep is based on the research of Rosen and Gur[8] [11]. The equations used are obtained from their research. The implementation uses various stations along the free stream. A sketch of the propeller stream tube is provided in Figure 3.1. Next to the ambient, far wake and actuator disk conditions, upstream and downstream conditions infinitesimally close to the actuator disk are defined as well. These are denoted in the Figure 3.1 by p^- and p^+ respectively.

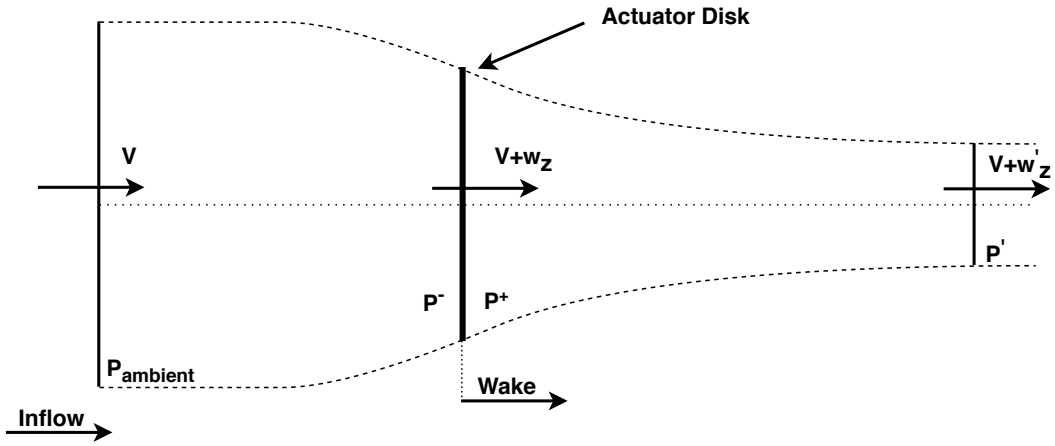

Figure 3.1: Stream-tube showing the inflow area, actuator disk and wake

The solution procedure for solving the propeller flow using the sweep included BEM method can be divided into three stages. In the first stage, the flow passing through the actuator disk is evaluated. This is similar to most classic BEM implementation, with the exception of the additional radial velocity terms and sweep terms included in this implementation. In the second stage the properties of the wake of the flow are computed. This stage is no different to other wake extensions. In the third stage the convergence of the complete solution is checked. Stage 1 and 2 are computed iteratively until convergence of the separate stages is reached, while stage 3 is an iterative loop through all stages. In stage 3, a correction, p_0, is applied to the pressure at the disk plane which ensures the conservation of axial momentum throughout the complete solution. A schematic overview is provided in Figure 3.2. Each stage is discussed separately in the next sections. The corresponding equations are provided there as well.

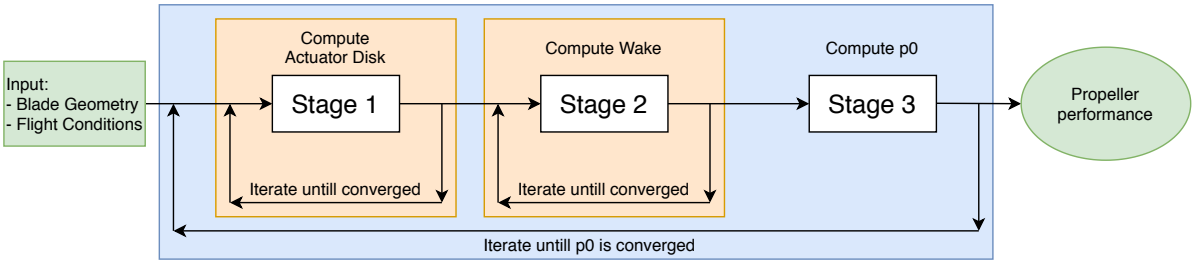

Figure 3.2: Schematic overview of BEM implementation

As with other BEM implementations, the properties of each airfoil have to be computed beforehand. In this case, RFOIL is used to compute the pressure distributions of each airfoil. A grid sweep was done for the angle of attack and Reynolds number. The angle of attack was analysed ranging from -20 to 20 degrees in steps of 0.1 degree. The Reynolds number was varied between $0.5 \cdot 10^5$ to $15 \cdot 10^5$ in steps of $0.5 \cdot 10^5$. As there are 25 radial stations on the blade, this resulted in approximately $300 \cdot 10^5$ distributions to be generated. An interpolant for the C_l and C_d could be created from these distributions. In a next stage, the pressure distributions are used to compute the noise as well.

Additionally, this BEM method requires the use of the pressure ratio factor k. As can be seen from Equation 3.1, the pressure ratio factor is essentially a relation between the pressure on the upper surface and lower surface of the airfoil, and the zero lift condition. The pressure coefficients of the upper and lower surface are computed according to Equation 3.2 and Equation 3.3.

$$k = \frac{-\int_0^1 \left[\tilde{C}_{Pu}(x/c) - \tilde{C}_{Pu0}(x/c)\right] \cdot \mathrm{d}(x/c)}{\int_0^1 \left[\tilde{C}_{Pl}(x/c) - \tilde{C}_{Pu}(x/c)\right] \cdot \mathrm{d}(x/c)} \tag{3.1}$$

$$\tilde{C}_{Pu}\left(\frac{x}{c}\right) = \frac{\Delta p_u(x/c)}{\frac{1}{2} \cdot \rho \cdot V^2} \tag{3.2}$$

$$\tilde{C}_{Pl}\left(\frac{x}{c}\right) = \frac{\Delta p_l(x/c)}{\frac{1}{2} \cdot \rho \cdot V^2} \tag{3.3}$$

The local blade sweep is denoted by Λ. According to Rosen and Gur [8] the sweep is defined by the quarter chord line of the blade in the plane of rotation. This is depicted in Figure 3.3. The sweep is computed by drawing a line from each quarter chord point on the airfoil stations towards the next. Then, a reference line parallel to the centre line of the unswept blade is drawn which intersects the quarter chord line. In the case of Figure 3.3, the reference line is horizontal. In this study, the blade is build along the vertical axis. The angle between the parallel reference line and the quarter chord line is the local angle of attack. Any out of plane translation for sweep or lean is not accounted for using this method.

The way sweep is defined in [8] does leave room for questions. The first is whether it is correct to chose a quarter chord sweep instead of using a mid chord sweep. Since out of plane movement needs to be taken into account to some extent, it can be reasoned that it would be better to take the sweep at the mid chord line, since the out of plane movement of the leading edge and trailing edge are then averaged. Another ambiguity is how the quarter chord line or mid chord line is projected onto the actuator disk. One can project the sweep line after all rotation for pitch and twist has been done, but this implies that the sweep used in the BEM computations changes when adjusting the pitch angle. This means that the sweep has become dependent on the pitch. Another way to define the sweep line is to project it onto the actuator disk before the pitch and twist rotation are applied. This means that the sweep does not change when the pitch angle is adjusted. These issues are addressed in the BEM verification in chapter 9.

The required propeller input for the BEM analysis in this study is provided at 25 radial stations along the blade. Since segments with an area are required for the BEM analysis, some adjustments are required for the tip and root airfoil section. With exception of the root and tip segment, all segments are defined such that a radial station is positioned in the middle of a segment. For the tip and root, interpolation is used to create artificial tip and root segments.

3.2.1. BEM Stage 1: Computing Actuator Disk Properties

The 12 unknown variables in this stage are shown below. At the start of the first iteration, all variables are assumed to be zero.

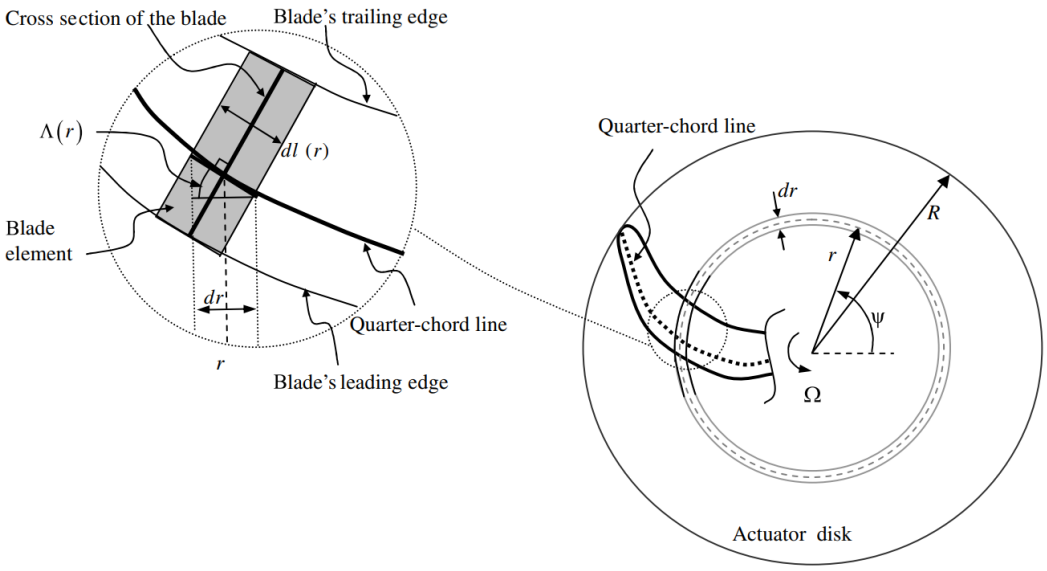

Figure 3.3: Blade in plane of rotation showing the definition of sweep according to Rosen and Gur [8]

$$\begin{array}{ccc} w_r(r), & w_\psi(r), & w_z(r) \\ v_r\left(r, z=0^-\right), & v_r\left(r, z=0^+\right), & v_\psi\left(r, z=0^+\right) \\ p\left(r, z=0^-\right), & L'(r), & \varphi(r), \\ \alpha(r), & U(r), & D'(r) \end{array}$$

First, the angle $\varphi(r)$ (see Figure 2.1) is computed according to Equation 3.4. Then, using $\varphi(r)$, the angle of attack $\alpha(r)$ can be determined using the simple relation shown in Equation 3.5.

$$\varphi(r) = \tan^{-1}\left[\frac{V + w_z(r)}{\Omega \cdot r \cdot \cos\Lambda(r) - w_\psi(r) \cdot \cos\Lambda(r) + w_r(r) \cdot \sin\Lambda(r)}\right] \tag{3.4}$$

$$\alpha = \beta - \varphi \tag{3.5}$$

The absolute velocity is then computed using Equation 3.6, from which the Mach number and Reynolds number can be computed as shown in Equation 3.7 and Equation 3.8.

$$U(r) = \sqrt{[V + w_z(r)]^2 + \left[\Omega \cdot r \cdot \cos\Lambda(r) - w_\psi(r) \cdot \cos\Lambda(r) + w_r(r) \cdot \sin\Lambda(r)\right]^2} \tag{3.6}$$

$$M = \frac{U}{\sqrt{\gamma R T_s}} \tag{3.7}$$

$$Re = \frac{\rho U l_{chord}}{\mu} \tag{3.8}$$

Using the previously computed quantities, the C_l, C_d and k of each radial station can be obtained by interpolation of the RFOIL results. The Karman-Tsien compressibility correction is applied on the C_l and C_d afterwards. See Equation 3.9 for this relation.

$$C_p = \frac{C_{p,0}}{\sqrt{1 - M_\infty^2} + \left[M_\infty^2 / (1 + \sqrt{1 - M_\infty^2})\right] C_{p,0}/2} \tag{3.9}$$

The Prandtl tip loss and root loss corrections are applied to the lift and drag coefficients after the compressibility correction is applied. The expressions for the Prandtl tip loss correction can be found in Equation 3.10, Equation 3.11 and Equation 3.12.

$$\phi_{tip} = \arctan\left(\frac{r}{R} \cdot \tan\phi\right) \tag{3.10}$$

$$s = \frac{\pi \cdot D \cdot \sin\phi_{tip}}{N_b} \tag{3.11}$$

$$F = \frac{2}{\pi} \cdot \arccos\left(\exp\left[-\pi \cdot \frac{R-r}{s}\right]\right) \tag{3.12}$$

The lift and drag per unit length are computed using Equation 3.13 and Equation 3.14.

$$L' = \frac{1}{2}\rho U^2 l_{chord} C_l \tag{3.13}$$

$$D' = \frac{1}{2}\rho U^2 l_{chord} C_d \tag{3.14}$$

Next, the upstream pressure infinitesimally close to the actuator disk is computed as seen in Equation 3.15.

$$p(r, z=0^-) = p_\infty + p_0(r) - k(r) \cdot \frac{N_b \cdot \left(L'(r) \cdot \cos\varphi(r) - D'(r) \cdot \sin\varphi(r)\right)}{2 \cdot \pi \cdot r \cdot \cos\Lambda(r)} \tag{3.15}$$

Applying Bernoulli far upstream and at upstream at the actuator disk allows to compute the axial induced velocity w_z from Equation 3.16. Use is made of the conservation of angular momentum, resulting in that a fluid particle is assumed to not cross the actuator disk more than once. This assumptions leads to Equation 3.17.

$$\frac{1}{2}\rho\left((V + w_z)^2 + v_r^2(r, z=0^-)\right) + p(r, z=0^-) = \frac{1}{2}\rho V^2 + p_\infty \tag{3.16}$$

$$v_\psi(r, z) = 0 \quad \text{for} \quad z < 0 \tag{3.17}$$

With the induced axial velocity at the disk known, the radial upstream velocity can be determined. As can be seen from Equation 3.18, this step requires to integrate along the radius of the blade. This does make the procedure more computational expensive.

The influence of each radial station is determined by integrating from root to tip. In this formulation, r_1 is the location each radial station. A small tolerance ϵ is applied to make sure that while integrating, a step never lands exactly on the position of a station. Functions A and B are computed using Equation 3.19 and Equation 3.20.

$$\begin{aligned} v_r(r, z=0^-) = \lim_{\varepsilon\to 0}\Big\{ & -\tfrac{1}{\pi} \cdot \textstyle\int_{r_1=0}^{r_1=r-\varepsilon} w_z(r_1) \cdot r_1 \cdot [r \cdot A(r, z, r_1) - r_1 \\ & \cdot B(r, z, r_1)] \cdot \mathrm{d}r_1 - \tfrac{1}{\pi} \cdot \textstyle\int_{r_1=r+\varepsilon}^{r_1\to\infty} w_z(r_1) \cdot r_1 \cdot [r \cdot A(r, z, r_1) - r_1 \\ & \cdot B(r, z, r_1)] \cdot \mathrm{d}r_1 + \tfrac{w_z(r)}{\pi \cdot r} \cdot \varepsilon \cdot \ln\varepsilon \Big\} \end{aligned} \tag{3.18}$$

In Equation 3.19 and Equation 3.20, complete elliptic integrals of the first kind and second kind, have to be solved. These are denoted by $K(\kappa)$ and $E(\kappa)$ respectively. These are solved using built-in functions of MATLAB. Variable κ is determined using the relation of Equation 3.21.

$$A(r, z, r_1) = \frac{2}{\left[(r - r_1)^2 + z^2\right] \cdot \sqrt{(r + r_1)^2 + z^2}} \cdot E(\kappa) \tag{3.19}$$

$$B(r, z, r_1) = \frac{r^2 + r_1^2 + z^2}{r \cdot r_1\left[(r-r_1)^2 + z^2\right] \cdot \sqrt{(r+r_1)^2 + z^2}} \cdot E(\kappa) - \frac{1}{r \cdot r_1 \cdot \sqrt{(r+r_1)^2 + z^2}} \cdot K(\kappa) \tag{3.20}$$

$$\kappa = 2 \cdot \sqrt{\frac{r \cdot r_1}{(r + r_1)^2 + z^2}} \tag{3.21}$$

When the upstream radial velocity from Equation 3.18 is evaluated at a radius larger than the propeller radius R, the approximation from Equation 3.22 is used. Note that at the actuator disk $z = 0$, omitting the second term of Equation 3.22.

$$v_z(r, z) \cong \frac{w_z(R) \cdot R^4}{r^4} - \frac{Q}{4 \cdot \pi} \cdot \frac{z}{\left(r^2 + z^2\right)^{3/2}} \quad \text{for } r \geq R \tag{3.22}$$

With $v_r(r, z=0^-)$ known, $v_r\left(r, z=0^+\right)$ can be determined as well using Equation 3.23. The downstream angular velocity is obtained by combining Equation 3.17 and Equation 3.24.

$$[V + w_z(r)] \cdot \left[v_r\left(r, z=0^+\right) - v_r\left(r, z=0^-\right)\right] = \frac{1}{\rho} \cdot \frac{N_b \cdot \tan\Lambda(r) \cdot \left(L'(r) \cdot \sin\varphi(r) + D'(r) \cdot \cos\varphi(r)\right)}{2 \cdot F \cdot \pi \cdot r} \tag{3.23}$$

$$[V + w_z(r)] \cdot \left[v_\psi\left(r, z=0^+\right) - v_\psi\left(r, z=0^-\right)\right] = \frac{1}{\rho} \cdot \frac{N_b \cdot \left(L'(r) \cdot \sin\varphi(r) + D'(r) \cdot \cos\varphi(r)\right)}{2 \cdot F \cdot \pi \cdot r} \tag{3.24}$$

Lastly, the induced angular and radial velocities at the disk are computed using Equation 3.25 and Equation 3.26.

$$w_\psi = \frac{1}{2} v_\psi\left(r, z=0^+\right) \tag{3.25}$$

$$w_r = \frac{1}{2}\left(v_r\left(r, z=0^-\right) + v_r\left(r, z=0^+\right)\right) \tag{3.26}$$

After these quantities are computed, the new values are compared with the values obtained in a previous iteration. If the differences are larger than the set convergence criterion, a new iteration is done until convergence is reached. Relaxation factors are applied as well to aid stability and convergence.

3.2.2. BEM Stage 2: Computing Wake Characteristics

In the second stage, the wake characteristics are determined. These characteristics depend on the actuator disk properties computed in stage 1. The wake characteristics are denoted by subscript $'$. The first time this stage is reached, the following assumptions are made:

$$\begin{gathered} w'_z = 2 w_z \\ w'_\psi = w_\psi \\ p' = p_\infty \\ r' = r \end{gathered}$$

The stage iteration then commences by computing the downstream disk pressure is first using Equation 3.27.

$$p\left(r, z=0^+\right) = \frac{N_b \cdot \left(L'(r) \cdot \cos\varphi(r) - D'(r) \cdot \sin\varphi(r)\right)}{2 \cdot \pi \cdot r \cdot \cos\Lambda(r)} + p\left(r, z=0^-\right) \tag{3.27}$$

Next, the radius of each radial station in the wake is determined using Equation 3.28.

$$w'_\psi \cdot r' = v_\psi\left(r, z=0^+\right) \cdot r \tag{3.28}$$

Applying Bernoulli far upstream and far downstream allows to compute p', as shown in Equation 3.29. Note the pressure difference along the disk which is included, denoted by Δp.

$$p' = \Delta p + p_\infty - \frac{\rho}{2}\left(\left(V + w'_z\right)^2 - V^2 + w'^2_\psi\right) \tag{3.29}$$

The angular velocity in the far wake is computed using Equation 3.30 and the assumption of Equation 3.31.

$$\frac{\mathrm{d}p'\left(r'\right)}{\mathrm{d}r'} = \rho \cdot \frac{w^2_\psi\left(r'\right)}{r'} \tag{3.30}$$

$$p'\left(r'\right) = p_\infty \quad \text{for} \quad r' \geq r'(R) \tag{3.31}$$

The induced velocity in the far wake, w'_z, is obtained by solving Equation 3.32.

$$\begin{aligned} &\tfrac{\rho}{2} \cdot \left\{[V + w_z(r)]^2 + v^2_\psi\left(r, z=0^+\right) + v^2_r\left(r, z=0^+\right)\right\} \\ &\quad + p\left(r, z=0^+\right) = \tfrac{\rho}{2} \cdot \left\{\left[V + w'_z\left(r'\right)\right]^2 + w'^2_\psi\left(r'\right)\right\} + p'\left(r'\right) + \left(p' - p_\infty\right) \end{aligned} \tag{3.32}$$

This stage is iterated until convergence is reached, similar to stage 1. Relaxation is applied in this stage as well.

3.2.3. BEM Stage 3: Complete Solution Convergence

This stage ensures convergence of the complete solution. For the next steps, some equations have to be combined. Thrust can be obtained from Equation 3.33 by making use of the already computed pressure difference over the disk. However, applying conservation of axial momentum, thrust can also be obtained using Equation 3.34.

$$\mathrm{d}T(r) = 2 \cdot \pi \cdot r \cdot \Delta p(r) \cdot \mathrm{d}r \tag{3.33}$$

$$\mathrm{d}T(r) = 2 \cdot \pi \cdot \rho \cdot r'(r) \cdot \left\{V + w_z'\left[r'(r)\right]\right\} \cdot w_z'\left[r'(r)\right] \cdot \mathrm{d}r' - 2 \cdot \pi \cdot r'(r) \cdot \left\{p_\infty - p'\left[r'(r)\right]\right\} \cdot \mathrm{d}r \tag{3.34}$$

Conservation of mass is formulated as seen in Equation 3.35.

$$\left[V + w_z(r)\right] \cdot r \cdot \mathrm{d}r = \left[V + w_z'\left(r'\right)\right] \cdot r' \cdot \mathrm{d}r' \tag{3.35}$$

By combining Equation 3.33, Equation 3.34 and Equation 3.35, one can obtain Equation 3.36. According to [8], $\Delta p_e(r)$ can be seen as an equivalent pressure difference across the actuator disk.

$$\Delta p_e(r) = \Delta p(r) - \left(p_\infty - p'\left[r'(r)\right]\right) \cdot \frac{V + w_z(r)}{V + w_z'\left[r'(r)\right]} \tag{3.36}$$

As proposed in [8], the pressure correction p_0, ensuring axial momentum conservation, is computed according to Equation 3.37. Parameter C should be 0, but can be tuned when convergence criteria are not met.

$$p_0(r) = (1 + C) \cdot k(r) \cdot \left(p_\infty - p'\left[r'(r)\right]\right) \cdot \frac{V + w_z(r)}{V + w_z'\left[r'(r)\right]} - C \cdot k(r) \cdot \Delta p(r) \tag{3.37}$$

When p_0 is computed, it can be compared with the p_0 obtained in the previous iteration. When the convergence criterion is not met, the new p_0 is used as input for stage 1, and the complete iterative loops from stage 1 and 2 are repeated.

3.2.4. Computing Performance Characteristics

When all stages have converged successfully, the performance characteristics of the blade can be computed. This computation is straightforward and similar to other BEM methods, with the exception of the area computation. Due to the addition of sweep, the area of each blade section is adjusted. This is done by correcting $\mathrm{d}r$, as can be seen in Equation 3.38.

$$\mathrm{d}l = \frac{\mathrm{d}r}{\cos\Lambda} \tag{3.38}$$

With $\mathrm{d}l$ known, the thrust and torque at each radial segment are computed using Equation 3.39 and Equation 3.40. The total thrust and torque are obtained by a simple summation of the values at each station.

$$\mathrm{d}T = \frac{1}{2} \cdot \rho \cdot U^2 \cdot N_b \cdot l_{chord} \cdot (C_l \cdot \cos\phi - C_d \cdot \cos\phi) \cdot \mathrm{d}l \tag{3.39}$$

$$\mathrm{d}Q = \frac{1}{2} \cdot \rho \cdot U^2 \cdot N_b \cdot l_{chord} \cdot r \cdot (C_l \cdot \cos\phi - C_d \cdot \cos\phi) \cdot \mathrm{d}l \tag{3.40}$$

The non-dimensional characteristics are obtained in the conventional procedure. The computation of the thrust coefficient and power coefficient is shown in Equation 3.41 and Equation 3.42.

$$C_T = \frac{T}{\rho \cdot n^2 \cdot D^4} \tag{3.41}$$

$$C_P = \frac{2 \cdot \pi \cdot Q}{\rho \cdot n^2 \cdot D^5} \tag{3.42}$$

The efficiency is obtained from Equation 3.43. With all quantities at each station and the total quantities known, the BEM analysis is finished. The radial data from the BEM analysis is used during the Noise computation. The chordwise data from RFOIL, used in the computation of pressure ratio factor k, is also used in the Noise computation. A discussion on the noise is found in chapter 5.

$$\eta = J \cdot \frac{C_T}{C_P} \tag{3.43}$$

4

RANS Based Propeller Flow Analysis

The theoretical and practical aspects of the RANS model are discussed in this chapter. As stated in chapter 2, RANS is the choice of high-fidelity method in this study to correct the BEM results. The commercial software package *ANSYS Fluent 19.2* is used for both domain meshing and solving. The the mathematical background of RANS is covered first in section 4.1, followed by a discussion on the computational domain, boundary conditions, grid generation and grid error estimation in section 4.2. Validation and verification of the RANS solver are performed in chapter 9.

4.1. Governing RANS Equations

This section covers some fundamental details on the RANS solver. In this study, steady-state RANS simulations are performed with viscous and compressibility effects taken into account. An existing implementation of RANS and the SA turbulence model is used by means of the commercial software *ANSYS Fluent 19.2*. A short overview of the governing equations is provided below. For more information on the implementation, the reader is referred to the *ANSYS Fluent* manual [18].

Three fundamental equations for Navier-Stokes methods are: the conservation of mass, conservation of momentum and conservation of energy. These are provided in Equation 4.1, Equation 4.2 and Equation 4.3 respectively. In these equations, density is denoted by ρ, flow velocity by u with i or j component, and the deviatoric stress tensor by τ_{ij}. E is the total energy, and f is the ith or jth body force component. The pressure is denoted by p, while q_i represents the heat conduction.

$$\frac{\partial \rho}{\partial t} + \frac{\partial (\rho u_j)}{\partial x_i} = 0 \tag{4.1}$$

$$\frac{\partial (\rho u_j)}{\partial t} + \frac{\partial (\rho u_i u_j)}{\partial x_i} = -\frac{\partial p}{\partial x_j} + \frac{\partial \tau_{ij}}{\partial x_i} + \rho f_j \tag{4.2}$$

$$\frac{\partial (\rho E)}{\partial t} + \frac{\partial (\rho u_i E)}{\partial x_i} = -\frac{\partial u_i p}{\partial x_i} + \frac{\partial u_i \tau_{ij}}{\partial x_i} - \frac{\partial q_i}{\partial x_i} + u_i \rho f_i \tag{4.3}$$

To reduce the computational load, the governing equations are first statistically averaged instead of solving them directly. This is the basis of Reynolds-Averaged Navier-Stokes Simulation. The averaging does reduce the accuracy of the flow solution, but due to the lower computational requirements the method is more accessible for research than for example LES or DNS.

For Reynolds averaging, the key step is to decompose the scalar quantities into the sum of their mean value and the fluctuation. This is shown in Equation 4.4 for the velocity component u_i.

$$u_i = \langle u_i \rangle + u_i' \tag{4.4}$$

An ensemble averaged solution is given in Equation 4.5, while the average for statistically stationary process is provided in Equation 4.6.

$$\langle u_i \rangle = \frac{1}{N} \sum_{\mu=1}^{N} u_i|_\mu \tag{4.5}$$

$$\langle u_i \rangle = \lim_{t\to\infty} \frac{1}{t} \int_0^t u_i(t')\,dt' \tag{4.6}$$

New expressions can be obtained by substituting variables in the decomposed form of the sum of the mean and the fluctuation, as seen in Equation 4.4, into the continuity equation and momentum equation. By applying the average operator and simplifying as much as possible, ie. the mean of the fluctuating part equals zero, the ensemble-averaged equations are obtained. See Equation 4.7 and Equation 4.8 for the application to the continuity equation and conservation of momentum equation.

$$\frac{\partial(\rho)}{\partial t} + \frac{\partial(\rho\langle u_i \rangle)}{\partial x_i} = 0 \tag{4.7}$$

$$\frac{\partial\left(\rho\langle u_i \rangle\right)}{\partial t} + \frac{\partial\left(\rho\langle u_i \rangle\langle u_j \rangle\right)}{\partial x_j} = -\frac{\partial p}{\partial x_i} + \frac{\partial}{\partial x_j}\left[\mu\left(\frac{\partial\langle u_i \rangle}{\partial x_j} + \frac{\partial\langle u_j \rangle}{\partial x_i} - \frac{2}{3}\delta_{ij}\frac{\partial\langle u_l \rangle}{\partial x_l}\right)\right] + \frac{\partial(-\rho\langle u_i' u_j' \rangle)}{\partial x_j} \tag{4.8}$$

The Reynolds stresses are given by the term $-\rho\langle u_i' u_j' \rangle$ and need to be modelled as there are more unknowns than equations. The turbulence models can approximate the Reynolds stress term, or also known as the stress tensor.

4.2. RANS Simulation Set-Up

In this section, the set-up of the CFD simulations is discussed. First, the computational domain and boundary conditions are elaborated on. Then, the grid choice is discussed along with a discussion on the determination of the height of the first mesh layer and estimation of the grid discretisation error. The actual findings for the grid discretisation error are discussed in chapter 9.

4.2.1. Computational Domain

The definition of the computational domain can largely impact both the end solution as the convergence of the simulation. A domain which is too large or too small may cause non-physical effects to appear in the solution. As this study only comprises flows with a zero angle of attack, axi-symmetry can be used to drastically reduce the computational domain. Due to axi-symmetry, only one propeller blade has to be analysed. This translates to a wedge shaped computational domain, with periodic boundaries on the side. The angle of the wedge is determined by dividing 360 degrees with the number of propeller blades. A domain size optimisation is out of scope of this research, and therefore conventional rules based on the blade radius are used for the domain sizing. This results in a domain height of 10R, with R being the blade radius. The distance between the inlet and blade, and outlet and blade are equal to 10R as well. An illustration of such domain is provided in Figure 4.1.

In the case of Figure 4.1, the complete domain is given the rotational velocity of the propeller, while the blade itself is stationary. This formulation allows for a steady-state solution instead of a transient solution, which reduces the computational effort. The domain consists of several boundaries: an inlet, outlet, far-field, 2 periodic boundaries and 3 stationary wall boundaries. The wall boundaries represent the propeller blade, spinner and nacelle.

4.2.2. Boundary conditions

After having defined the computational domain, correct boundary conditions need to be imposed for the initialisation and run of the simulation. The enclosure, or complete domain, is given the rotational velocity corresponding the advance ratio of the propeller. The propeller blade itself has zero rotational velocity. For the pressure inlet, pressure far-field and pressure outlet, additional flow properties need to be computed.

Either International Standard Atmsophere (ISA) values are assumed, or specific conditions have to be provided. With the static temperature, T_s, known, and using assumptions for the specific heat ratio γ and gas constant R of air, the boundaries can be computed. The isentropic flow relations are used to compute the required total temperature and pressure quantities. For the pressure far-field boundary, the Mach number and static temperature are required. The Mach number is determined by first computing the speed of sound in Equation 4.9, followed by Equation 4.10.

$$a_0 = \sqrt{\gamma \cdot R \cdot T_s} \tag{4.9}$$

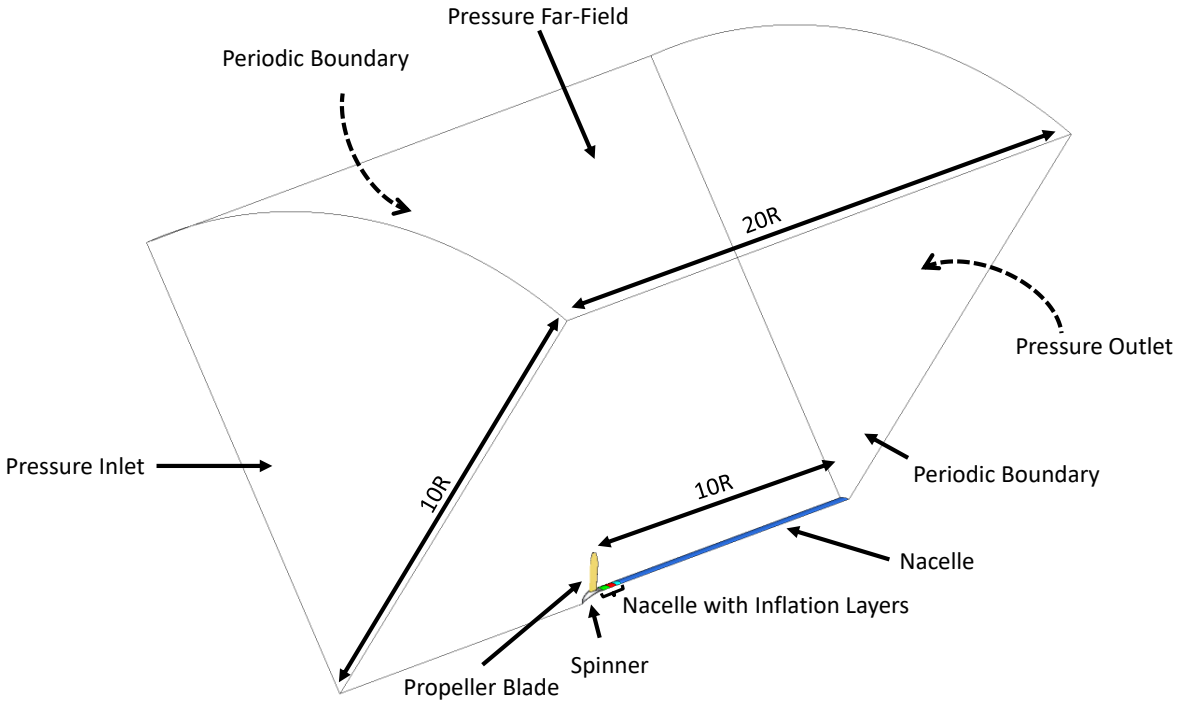

Figure 4.1: Computational domain enclosure in the shape of a wedge

$$M = \frac{V_\infty}{a} \tag{4.10}$$

The pressure inlet and pressure outlet require the total temperature as input. This property is determined using the previously found Mach number and static temperature, as can be seen in Equation 4.11.

$$T_0 = T_s \cdot \left(1 + \frac{\gamma - 1}{2} \cdot M^2\right) \tag{4.11}$$

The pressure inlet also requires a pressure gauge value as input. This value is the delta between the static pressure and total pressure. The gauge pressure is thus determined by computing the total pressure quantity using the isentropic relations, and subtracting the static pressure. This is shown in Equation 4.12.

$$\Delta P_{0,gauge} = P_s \cdot \left(1 + \frac{\gamma - 1}{2} M^2\right)^{\frac{\gamma}{\gamma - 1}} - P_s \tag{4.12}$$

4.2.3. Meshing

Volume and surface discretisation are an essential part of 3D computational fluid dynamics. Multiple methods exist to create a discretized grid, each with their own advantages and disadvantage. First, a short summary with criteria and options for volume discretisation methods is provided, as well as an explanation for the choice of grid. The implementation of the mesh is then shown, followed by a discussion on the methods for determining the first inflation layer height and estimating the grid disretisation error.

Volume and Surface Discretisation

Finite volume methods divide the computational domain into discrete, non overlapping volumes. For each volume, the discrete flux balance is evaluated. Three main types of grids are available in *ANSYS Fluent*: structured grids, unstructured grids and hybrid grids. Despite the differences between the methods, the main requirements for the grids remain the same[27]:

- Intersection and overlap of grid lines is not allowed.

- Refining or coarsening of the grid should be possible in selected regions.
- Orthogonality and smoothness of the grid must be maximised.
- The grid has to be able to represent the geometry by allowing a high enough grid resolution.

In structured grids, the cells have the same number of connections, and are similar at a topological level. In structured grids, grid domains, consisting of either rectangles or hexahedrons, can be presented and projected onto Cartesian domains [27]. These grids are straight forward and efficient for solver algorithms [27]. Grid generation may, however, be difficult for complex geometries. With automated CFD workflows, the robustness of the mesher is a decisive factor. For grid refinement, multi-block grids are likely required. An example of an airfoil section with a structured grid is provided in Figure 4.2.

Domains of unstructured grids can generally not be projected onto Cartesian domains and are mainly build out of triangles for two dimensional grids, and tetrahedrons for three dimensional grids [27]. Other shapes such as prisms are also possible. Unstructured grids are generally easier to apply to complex geometries compared to structured grids. Refinement of an unstructured grid can be done by dividing the grid element. A large downside to unstructured grids is that it is computationally more expensive for flow solvers than structured grids [27]. An example of an airfoil section with an unstructured grid is provided in Figure 4.3.

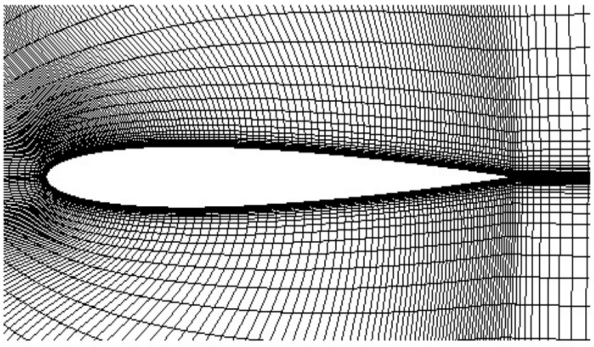

Figure 4.2: Structured Grid Example [27]

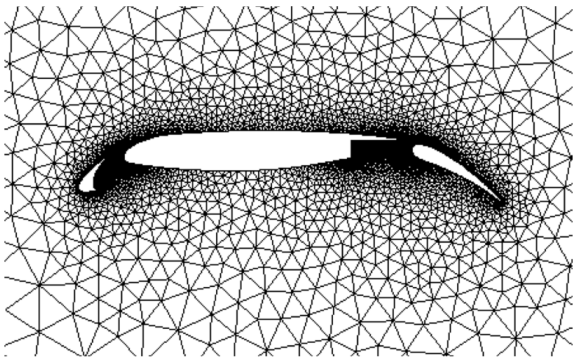

Figure 4.3: Unstructured Grid Example [27]

Hybrid grids combine both structured and unstructured mesh sections, or can consist of poly-hexcore 'hybrid' elements as introduced by Ansys [28]. This can be useful, as inflation layers for capturing boundary layer interactions benefit largely from a structured mesh, while outside of the inflation layer, a different type of mesh can be used to smoothly attach to any complex geometry. According to Ansys [28], poly-hexcore meshes are faster to solve, and require less resources for similar or better simulation results. The combination of a fast solve time, while keeping the flexibility to mesh complex geometries is ideal for this study. Therefore the hybrid approach is used in this work. Figure 4.4 shows an implemented hybrid mesh for this study.

Grid Implementation

Examples of the implemented hybrid grids are given in Figure 4.4 and Figure 4.5. Figure 4.4 clearly shows both structured and unstructured grids applied to connect the inflation layer on the spinner and blade with the rest of the discretised domain.

With the hybrid mesh approach taken, the surface mesh is generated using poly-prism shapes. Traditionally, blade surfaces are meshed by creating a division line on the leading edge between the upper and lower airfoil. Multiple chord-wise and radial grid spacings are then defined and imposed on the geometry to create a mesh. This method gives good results if the grid spacing parameters are well chosen by a researcher based specifically on a geometry. In this study however, the aim is to evaluate many different complex geometries. Therefore, a different approach is used. Instead of imposing a fixed grid spacing, a more robust method is used which takes into account the curvature of the geometry.

Curvature based surface meshing requires the minimum face size and maximum face size as input, next to the feature angle. The feature angle parameter compares the normal angles of adjacent cell faces. If the angle between the normal angles exceeds the feature angle parameter, an edge is created. This method offers flexibility in terms of geometry generation. Any geometry can be meshed, as based on the curvature of the mesh, refinement is automatically performed. This can be seen in Figure 4.5, where the trailing edge

and leading edge have automatically been refined. This method remains stable when introducing sweep or additional twist.

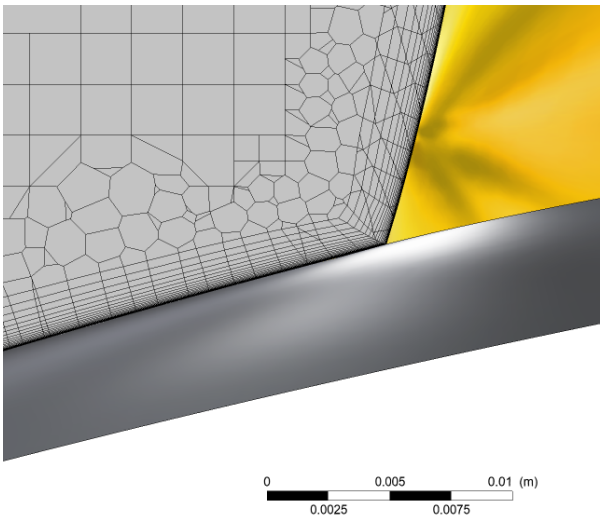

Figure 4.4: Hybrid volume mesh example used in this study

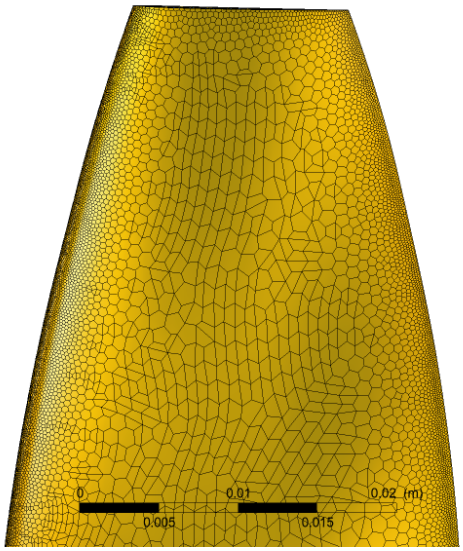

Figure 4.5: Surface mesh example used in this study

Figure 4.6 shows a cross-section of a meshed domain. Note the largely structured mesh, with irregular poly-prism shapes at the edges near the boundaries. Refinement boxes can also be identified from Figure 4.6. Two additional local volume mesh refinements are applied. One refinement box is placed in the upstream and downstream of the propeller, at 1.1R. The second refinement is located surrounding the propeller. The refinement is required to capture smaller flow phenomena on and surrounding the blade. Applying refinement only locally reduces the number of cells in the domain, and thus save computational effort.

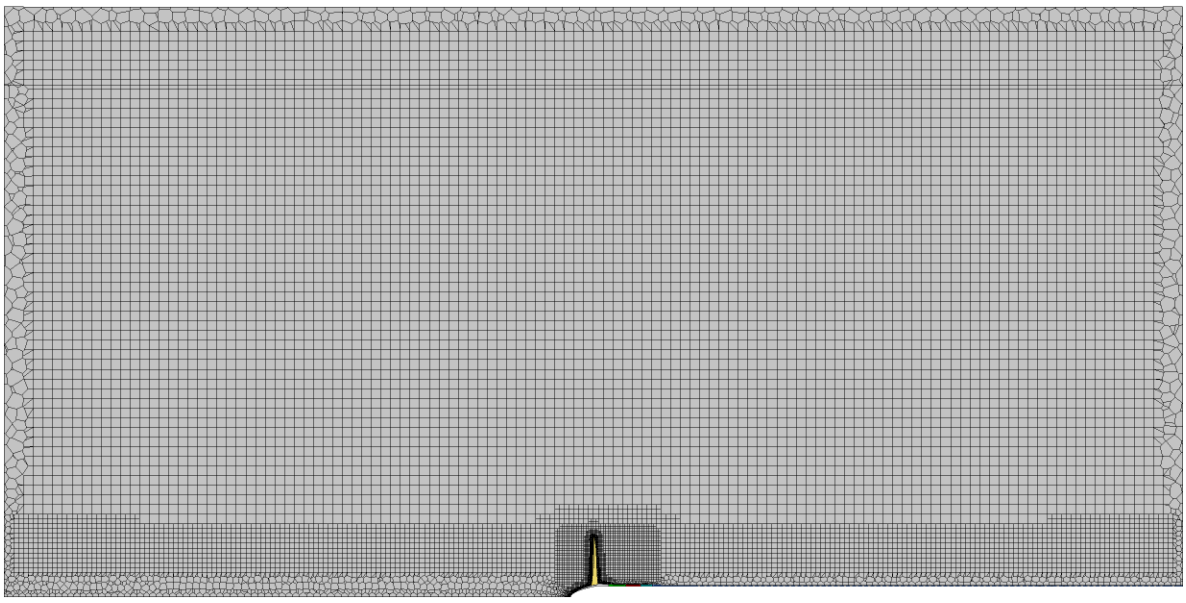

Figure 4.6: Plane of typical meshed domain used in this study

Determining Inflation Layer Height

The determination of the final number of inflation layers is discussed in section 9.1. The method of computing the first layer height is discussed in this section.

As large velocity gradients are present near walls, the grid is locally required to have a high resolution to resolve the boundary layer correctly. The dimensionless y^+ value is used to determine the required resolution. The thickness of the first inflation layer is tuned such that $y^+ \approx 1$ at 0.7 radius of the blade at the lowest advance ratio which is simulated. The lowest advance ratio results in the highest velocities and requires the smallest inflation layer height. This criterion ensures $y^+ \leq 1$ at all simulated conditions, and thus enables to capture the viscous sub-layer. Wall functions are also available for use at higher y^+ values, but those only approximate the development of the boundary layer which leads to less accurate results. The first inflation layer height that complies with $y+ \approx 1$ is found using the following procedure.

First, the velocity of the blade is determined at $0.7R$ using Equation 4.13. Note that induced velocities are ignored in this computation, and that the velocity is based purely on the geometrical conditions.

$$U = \sqrt{(r\omega)^2 + V_{inlet}^2} \tag{4.13}$$

The Reynolds number can then be estimated as follows as function of the density ρ, absolute velocity U, chord length l_{chord}, and dynamic viscosity μ.

$$Re = \frac{\rho U l_{chord}}{\mu} \tag{4.14}$$

The skin friction coefficient and wall shear are computed using Equation 4.15, obtained from Schlichting [29], and Equation 4.16 respectively.

$$C_f = \left(2\log_{10}(Re) - 0.65\right)^{-2.3} \tag{4.15}$$

$$\tau_w = 0.5 C_f \rho U^2 \tag{4.16}$$

The friction velocity u_*, and consequently the first layer height y can then be determined using Equation 4.17 and Equation 4.18 respectively.

$$u_* = \sqrt{\frac{\tau_w}{\rho}} \tag{4.17}$$

$$y_{inflation\ layer} = \frac{y^+ \mu}{\rho u_*} \tag{4.18}$$

This procedure is done for both the blade and the spinner. The spinner is done separately as a higher first inflation layer height is allowed due to the lower absolute velocities on the spinner compared to the blade. A higher first inflation layer height generally results in fewer mesh cells and thus saves computational time.

Estimating the Grid Discretisation Error

The grid discretisation errors are computed using the method as described by Eça and Hoekstra [30]. For more information on this method, please refer back to the listed paper. The results from this method can be found in chapter 9. The method is shortly summarised next.

Richardson extrapolation is utilised to determine the grid errors. The basic formulation is presented in Equation 4.19. Here, δ_{RE} is the estimated error, and ϕ_i and ϕ_0 are the numerical and estimated exact solution respectively. The constant scaling factor is denoted by α, while h_i is the relative grid cell size. Parameter p is the order of accuracy.

$$\delta_{RE} = \phi_i - \phi_0 = \alpha h_i^p \tag{4.19}$$

The relative cell grid size is determined using a fraction between the grid with the maximum number of cells and grid i. This is shown in Equation 4.20.

$$h_i = \left(\frac{N_{cells,max}}{N_{cells,i}}\right)^{\frac{1}{3}} \tag{4.20}$$

As more than three grids were to be evaluated, a least squares approach was used to estimate ϕ_0, α and p. The function to be minimised is shown by Equation 4.21. Parameter n_g represents the number of the grid. This function is solved using the `lsqnonlin` function from MATLAB.

$$S(\phi_0, \alpha, p) = \sqrt{\sum_{i=1}^{n_g} \left(\phi_i - \left(\phi_o + \alpha h_i^p\right)\right)^2} \tag{4.21}$$

The standard deviation is computed as seen in Equation 4.22.

$$U_s = \sqrt{\frac{\sum_{i=1}^{n_g} \left(\phi_i - \left(\phi_o + \alpha h_i^p\right)\right)^2}{n_g - 3}} \tag{4.22}$$

When the parameters are fitted, the error is estimated using Equation 4.23. Here, Δm presents the maximum difference between the computed solutions, shown in Equation 4.24. The variables with superscript * indicate that the theoretical order of convergence of $p = 2$ is used.

$$U_\phi = \begin{cases} \min(1.25\delta_{RE} + U_s,\ 1.25\Delta m), & 0 < p < 0.95 \\ 1.25\delta_{RE} + U_s, & 0.95 < p < 2.05 \\ \max(1.25\delta^*_{RE} + U^*_s,\ 1.25\Delta m), & p \geq 2.05 \\ 3\Delta m, & p < 0 \end{cases} \tag{4.23}$$

$$\Delta m = \max(|\phi_i - \phi_j|) \tag{4.24}$$

5

Propeller Noise Prediction

After the propeller flow characteristics are computed, a separate method has to be implemented which can obtain the noise characteristics from both RANS and BEM results. As explained in chapter 2, the frequency-domain formulation from Hanson is applied in this work. The mathematical description which is implemented from scratch in MATLAB is discussed in section 5.1. Also the definition used for noise in this study is explained. Verification of the computed noise characteristics is performed in chapter 9.

5.1. Far-Field Tonal Noise Prediction Implementation

The frequency method is selected for this study. In this section the corresponding equations are provided showing how to get from a general expression far field noise to the implemented expression. Multiple researchers have gone through the process of deriving the frequency domain equations from scratch. The complete derivation is not part of this research, and the reader is referred to publications from for example Hanson [31][32], Magliozzi [16] and Parry [33] if interested. Important to note is that in this work, only the far-field noise is considered.

According to Hanson [31], the general far field pressure harmonic is given by Equation 5.1. In this equation, ρ_0 is the ambient density, c_0 is the speed of sound, and B is the number of blades. The radiation angle from the propeller axis to the observer point is denoted by θ, n is the harmonic of the shaft frequency, y is the observer distance from the propeller axis, D is the propeller diameter and M_x is the flight Mach number. M_r is the section relative Mach number, while M_t is the tip rotational Mach number. Two noise computations are performed in this study. In one computation, the θ is varied between 0 and 180 degrees and the observer distance from the propeller is kept constant such that the directivity can be visualised. In the second computation, the θ is varied between 15 and 165 degrees and the noise is projected on a line parallel to the propeller. This means that the distance from the observer to the propeller varies in the second computation. For the directivity computation the distance is set at 20 times the propeller diameter, while for the line computation the minimum observer distance is set at 20 times the propeller diameter.

$$\begin{aligned} P_{n,k} = &- \frac{\rho_0 c_0^2 B \sin\theta \exp\left(i\left[(n+q)\frac{\Omega r}{c_0} - sign(n+q)\frac{|n|\pi}{2}\right]\right)}{8\pi\left(y/D\right)(1-M_x\cos\theta)} \\ &\times \int_0^1 M_r^2 \exp\left(i\phi_{os}\right)\Psi_n(k_x) J_{|n|}\left(\frac{|n+q|zM_t\sin\theta}{1-M_x\cos\theta}\right)dz \end{aligned} \tag{5.1}$$

Equation 5.1 can be viewed as consisting of two parts: a constant part and an integrating part. The constant part is section independent, while the integral integrates along the normalised blade radius z. The terms inside the integral can thus be section independent and need to be determined for each separate section. The source term for noise generation is $\Psi_n(k_x)$. This source term is dependent on the thickness distribution and forces that act on the blade sections. The general description of this source term is shown in Equation 5.2 [31].

$$\Psi_{n,k}(k_x) = k_x^2 t_b \Psi_v(k_x) + i\Psi_{Fk}(k_x) + B_D \Psi_{rk}(k_x)\frac{\partial}{\partial z}(\cdot) \tag{5.2}$$

The first term in Equation 5.2 accounts for thickness, the second term accounts for axial and tangential forces, while the third term accounts for radial loading. In this study only the first two terms are used since this is in accordance with the derivation seen in [16]. The thickness term is a monopole, while the force terms, if expressed in lift and drag, are dipoles. The thickness shape function can be computed according to Equation 5.3 [31].

$$\Psi_v(k_x) = \int_{-\frac{1}{2}}^{\frac{1}{2}} H(X) \exp(ik_x X) dX \tag{5.3}$$

In this monopole term, the shape function $H(X)$ gives the normalised sectional thickness distribution such that the maximum thickness equals 1. The normalised chord is represented by X, which ranges from -0.5 to 0.5. It should be noted that this makes use of the thin blade assumption.

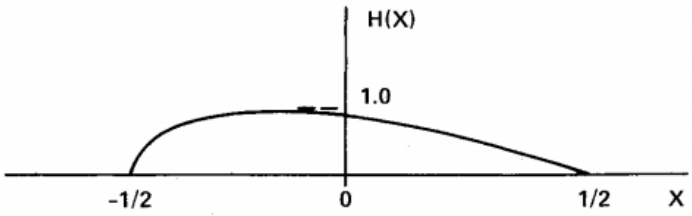

Figure 5.1: Thickness shape function example [32]

The second term in Equation 5.2 accounts for non-radial loading on the blade. In literature, this non-radial loading is often described in terms of lift and drag loading. This leads to the relation found in Equation 5.4 [32][31].

$$\Psi_{Fk} = k_y \left(\frac{C_{Lk}}{2}\right) \Psi_{Lk}(k_x) + k_x \left(\frac{C_{Dk}}{2}\right) \Psi_{Dk}(k_x) \tag{5.4}$$

However, the noise computation in this study relies on thrust and torque distributions. The derivation by Hanson in [31] shows that Ψ_{Fk} can also be described by a general expression based on axial and tangential forces, or thrust and tangential forces. This expression is shown in Equation 5.5 [31].

$$\Psi_{Fk} = -a(\omega - n - q) B_D \left(\frac{C_{f_x}}{2}\right) \Psi_{xk}(k_x) - \frac{n}{z} B_D \left(\frac{C_{f_\phi}}{2}\right) \Psi_{\phi k}(k_x) \tag{5.5}$$

The axial and tangential force sources from Equation 5.5 are described by Equation 5.6 and Equation 5.7 respectively.

$$\Psi_x(k_x) = \int_{-\frac{1}{2}}^{\frac{1}{2}} f_x(X) \exp(ik_x X) dX \tag{5.6}$$

$$\Psi_\phi(k_x) = \int_{-\frac{1}{2}}^{\frac{1}{2}} f_\phi(X) \exp(ik_x X) dX \tag{5.7}$$

The terms $f_x(X)$ and $f_\phi(X)$ are the sectional axial and tangential force distributions, normalised such that the areas integrate to unity. For the CFD solutions this is computed for each section at each advance ratio using the known pressure on the blade. For noise computations based on a BEM analysis, these shape functions are obtained from RFOIL. The lift and drag distribution is generated by RFOIL at each radial station for angles of attack ranging from -20 to 20, and for Reynolds numbers ranging from $0.5 \cdot 10^5$ to $15 \cdot 10^5$. Using the known angles from the BEM analysis, the lift and drag distributions can be transformed into axial and tangential distributions. For BEM solutions, using different shape distributions for each advance ratio resulted in unexpected oscillatory behaviour at high advance ratios in the final noise solution. Therefore the shape functions from one advance ratio is used for all advance ratios. This assumption is only applied to the BEM solutions, not the CFD solutions.

The sectional axial and tangential force coefficients, C_{f_x} and C_{f_ϕ}, are normalised similar to the general way lift is normalised. This is shown in Equation 5.8.

$$C_f = \frac{F}{\frac{1}{2}\rho V^2 S} \tag{5.8}$$

The dimensionless chord-wise wave numbers k_x and k_y are described by Equation 5.9 and Equation 5.10 respectively, in which a and σ_0 are given by Equation 5.11 and Equation 5.12.

$$k_x = \frac{2a}{\sigma}\left(\omega - q\right) B_D \tag{5.9}$$

$$k_y = -\frac{2}{\sigma}\left[\left(\omega - n - q\right) a^2 z - \frac{n}{z}\right] B_D \tag{5.10}$$

$$\sigma = \frac{U}{V} \tag{5.11}$$

$$a = \frac{\Omega r_t}{V} \tag{5.12}$$

The effects of lean and sweep of the blade are taken into account in Equation 5.1 by the inclusion of the phase delay factor ϕ_{os}. This factor is the summation of the separate influence of lean and sweep, as seen in Equation 5.13.

$$\phi_{os} = \phi_o + \phi_s \tag{5.13}$$

The phase delay contributions for lean and sweep are given by Equation 5.14 and Equation 5.15 respectively [31]. The MCA and FA are defined as shown in Figure 5.2 [32].

$$\phi_o = \frac{2}{z\sigma}\left(\frac{a^2 z^2 (n+q) M_x \cos\theta}{1 - M_x \cos\theta} - n\right)\frac{FA}{D} \tag{5.14}$$

$$\phi_s = \frac{2a}{\sigma}\left(\frac{n+q}{1 - M_x cos\theta}\right)\frac{MCA}{D} \tag{5.15}$$

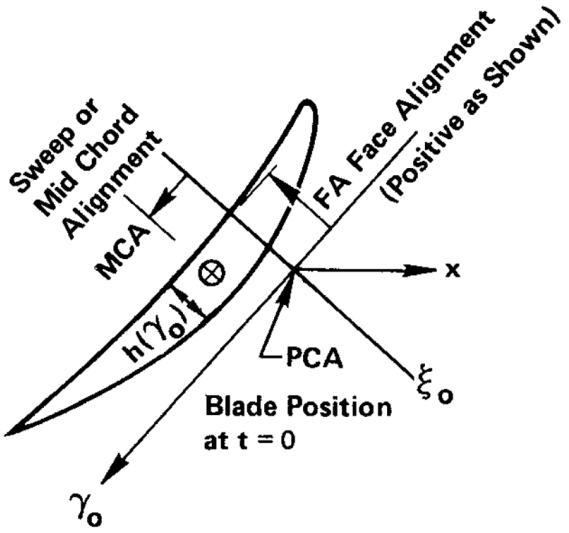

Figure 5.2: Lean and sweep definitions for the noise formulation[32]

Using that the stationary phase is given according to Equation 5.16 [31], the well known far field noise frequency domain equation from Hanson can be obtained.

$$\omega_0 = \frac{n+q}{1 - M_x \cos\theta} \tag{5.16}$$

A steady non-radial loading is to be assumed next. This assumption omits the radial term in Equation 5.2, and q becomes zero. Furthermore, in this case $n = mB$.

By substituting the previous mentioned equations in each other and writing out all expressions, finally Equation 5.17 is obtained. This is similar to the expression presented by Hanson in [32].

$$\begin{aligned} P_{mB} = &- \frac{\rho_0 c_0^2 B \sin\theta \exp\left[imB\left(\frac{\Omega r}{c_0} - \frac{\pi}{2}\right)\right]}{8\pi\left(y/D\right)\left(1 - M_x \cos\theta\right)} \\ &\times \int_0^1 M_r^2 \exp\left(i\left(\phi_o + \phi_s\right)\right) \Psi_{mB}(k_x) J_{mB}\left(\frac{mBzM_t \sin\theta}{1 - M_x \cos\theta}\right) dz \end{aligned} \tag{5.17}$$

However, there is a difference with the final expressions by Hanson from [31] and [32]. The difference is found in the expression for the source terms. Instead of lift and drag, axial and tangential forces are used to describe the dipole sources. This can be seen in Equation 5.18.

$$\Psi_n = \Psi_{mB} = k_x^2 t_b \Psi_v(k_x) + i\left(-\frac{\Omega r_t}{V}\left(\frac{mB}{1 - M_x cos\theta} - mB\right) B_D\left(\frac{C_{f_x}}{2}\right)\Psi_x(k_x) - \frac{mB}{z} B_D\left(\frac{C_{f_\phi}}{2}\right)\Psi_\phi\right) \tag{5.18}$$

As the noise source terms are easily separable, they can be computed independently to study the effect associated to each source. The total noise pressure is found by simply taking the sum of each component, as can be seen in Equation 5.19.

$$P_{mB} = P_{Vm} + P_{F_x m} + P_{F_\phi m} \tag{5.19}$$

The time dependent waveform for the mth harmonic can be determined by applying the Fourier Series as seen in Equation 5.20. This waveform can be used to determine the root mean squared wave from Equation 5.21.

$$p(t) = 2Re\left[\sum_{m=1}^{\infty} P_{mB} exp(imB\Omega t)\right] \tag{5.20}$$

In Equation 5.21, the terms T_1 and T_2 are the boundaries for time t. As the rotation is cyclic, the boundaries can be chosen such that they cover exactly one rotation of the blade.

$$p_{rms} = \sqrt{\frac{1}{T_2 - T_1}\int_{T_1}^{T_2} p(t)^2 dt} \tag{5.21}$$

The final sound pressure level can then be determined. A common way is to compare the sound pressure to an arbitrary reference sound pressure which the human ear can capture. Such relation is shown in Equation 5.22.

$$SPL = 20\log_{10}\left(\frac{p_{rms}}{p_{ref}}\right) \tag{5.22}$$

However, this does not provide much information in relation to the propeller that is evaluated. In this study, noise emissions of propellers are compared. Therefore, a different comparison is proposed, which relates the acoustic pressure from the propeller to its diameter and thrust. Equation 5.23 shows such relation.

$$\text{TSSP} = 20\log_{10}\left(p_{rms} \cdot \frac{D^2}{T}\right) \tag{5.23}$$

6

Blade Parametrisation

Parametrisation of propeller blades is necessary to perform the intended research. If no form of parametrisation is used, countless of coordinates have to be adjusted directly in order to change the blade geometry. This is not feasible. Parametrisation allows to change the blade geometry by adjusting only a few variables. The definitions of the blade parameters along with an explanation whether they are parametrised or kept constant are discussed first in section 6.1. Most parameters are not a single value, but comprise a distribution along the radius of the blade. In this study, Bezier curves are used to generate such a distribution. A short discussion on possible distribution parametrisation methods and why the Bezier curve method is selected is given in section 6.2. A description of the Bezier implementation used in this study is included in this section as well. The parametrisation errors are estimated in chapter 9.

In this study, experimental data from the XPROP propeller is available for validation. As is explained in the next section, not all possible blade design parameters are adjusted in this study. Values from the XPROP propeller are used when design parameters are kept constant. This propeller is visualised in Figure 6.1.

Figure 6.1: XRPOP propeller which is used as reference in this study

6.1. Propeller Design Parameters

The shape of a propeller blade can be described in many ways. For optimisation and surrogate modelling it is best if there are as few variables as possible. The blade is build up of several sections of airfoils along the blade radius, which have a variable shape and chord length, and can be positioned and oriented anywhere on a 3D grid. This means that instead of using a single value for twist, sweep and chord length distributions are used. Gur and Rosen divide all design variables in three categories [5]: general design variables, blade design

variables and cross-sectional design variables. The parameters required in this research to generate a blade are listed in this section.

- **Airfoil Shape**
  The airfoil shape is recognised as a cross-sectional parameter. The airfoil shape of each section can be defined by NACA profiles or curves coming from a distribution. Altering the airfoil shape increases the design space and computational effort. To reduce the computational cost, the airfoil shape is not varied in this study. The airfoil cross-sections from the XPROP have been normalized with respect to the chord length at their station, and are used throughout this study.

- **Twist Distribution**
  The twist distribution is defined as the twist angle which each cross-sectional airfoil makes around their local airfoil pitch change axis. The twist is not altered in this study, and therefore the XPROP twist is used. As part of a complete blade parametrisation, a Bezier curve is fitted to match the XPROP twist distribution.

- **Sweep Distribution**
  The sweep distribution is computed along the mid chord alignment. During the 3D blade generation, the collective pitch and twist are applied after the translation of airfoil cross-sections for sweep is performed.

- **Collective Pitch**
  The collective pitch is defined as the rotation around the pitch change axis of the root airfoil section. This is applied after twist and sweep. No distribution is required as this consists of a single value. The reference angle is set at 70% radius of the blade, which has an angle of zero degrees if the collective pitch is set to zero. The collective pitch is altered in this study.

- **Propeller Radius**
  Due to computational time limitations, this parameter is not altered in this study. The propeller radius is set equal to the XPROP propeller which is used for validation. The radius of the propeller is therefore fixed at 0.2032 meter. The created computational framework does allow for a variable radius, and it is recommended to include this in a future study.

- **Number of Blades**
  The number of blades impact the aerodynamic efficiency as well as the noise [5]. In this study, the number of blades is fixed to 6, which is equal to the number of blades of the XPROP propeller. Similar to the propeller radius, the number of blades can be easily varied in the created framework. The number of blades is already parametrized for the BEM, CFD and noise analysis. It is recommended to include a varying number of blades in a future study.

- **Rotational Speed**
  According to Gur [5], a reduction of the rotational speed reduces the propeller noise. The rotational speed is not optimised directly, but rather the advance ratio is used. The advance ratio is a relation between flight speed and rotational propeller speed. During the blade comparison, the advance ratio is adjusted to obtain a constant thrust for all blades in this study.

Other parameters influencing the propeller performance are the spinner and nacelle. In this study, the propeller blade is the main subject of interest. The spinner and nacelle geometries are therefore not varied. The spinner and nacelle used in the CFD analysis are equal to those of the XPROP. The spinner and nacelle dimensions are normalised with respect to the blade radius. Although not required for this study, the spinner and nacelle will thus scale when the blade radius is increased.

It should be noted that the order of operations is important in the blade generation. Figure 6.2 shows this order. First, the cross-sectional airfoils are placed along the radius, and centred along their pitch change axis. This axis is copied from the XPROP propeller, but this input to the framework can also be changed. As the airfoils are normalized with respect to their chord length, the centre point of each airfoil is also scaled to the chord. Next, the sweep is applied by translating each airfoil section along the direction of their chord. Then the twist is added, in which the airfoil sections are rotated along their local pitch change axis. Lastly, the collective pitch is added, at which all airfoils are rotated along the root or global pitch change axis.

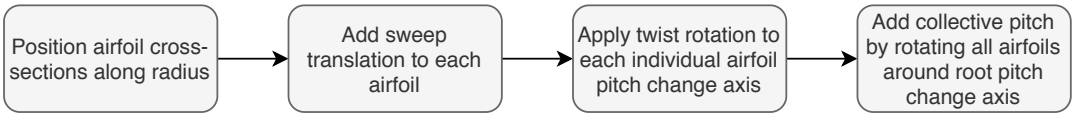

Figure 6.2: Order of operations for blade generation

6.2. Parametrisation of Radial Distributions of Design Parameters

There are various ways to describe a distribution, each has its advantages and disadvantages. Since the airfoil sections are kept constant in this study, only a parametrisation for the radial distributed parameters has to be implemented. A short description of options for distribution parametrisation are given first, followed by a description of the implementation. Options for methods to describe an arbitrary curve are listed below:

- **Bezier curves**
  Bezier curves are based on Bernstein polynomials. Control points are defined which bend the curve towards them. By moving the control points, the curve changes shape. Bezier curves are widely used in airfoil optimization, and require relatively few parameters.

- **NURBS**
  The Non-Uniform Rational B-Spline is a versatile method used to describe arbitrary curves and geometries in modern CAD software amongst others, and is a more generalised version of the Bezier curve. Control points are determined which determine the direction of the curve. By moving the control points in any direction, the curve is 'pulled' towards it depending on the weight. It is clear that this method offers a lot of freedom, but the number of parameters might increase fast.

- **Polynomials**
  Some other mentioned methods rely on multiple summed polynomials for a curve description, but polynomials can also directly be used to describe a curve. A wide range of shapes can be described using this method, but it suffers from the possible large number of parameters required to accurately describe shapes. Polynomial functions can also have unpredictable behaviour, resulting in non-smooth shapes.

The author has a preference to the Bezier curve since it is successfully applied in other similar research [6] [3]. The Bezier curve results in smooth continuous shapes and requires relatively few parameters. The implementation of the Bezier distribution is discussed next.

6.2.1. Bezier Curve Implementation

The Bezier curve is used to parametrise distributions in this research. A Bezier curve is a set of Bernstein polynomials which uses control points to create a curve. The general formulation is given in Equation 6.1. In this formulation, P_i denotes the i-th control point. The control point is a coordinate in a 2D grid in the form of (X,Y). The degree of the curve is denoted by n. The first and last control point directly fixate the start and end point of the curve. As the curve should always cover the complete radius of the blade, the start and end y-coordinate is fixed to the normalised 0 and 1 blade radius.

$$B(t) = \sum_{i=0}^{n} \binom{n}{i} (1-t)^{n-i} t^i P_i \tag{6.1}$$

The implementation in this research is done in MATLAB, and has been coded in a vectorized and dynamic matter. This makes the code to run fast and allows a Bezier curve of any number degrees, with a minimum of 2 control points. Two control points result in two variables due to the constraint of starting and ending at the root and tip of the blade. Each additional control point adds two more variables. Three control points therefore result in a total of four variables, and four control points result in six variables. An example of such a curve with four control points is given in Figure 6.3. The control points shown are randomly generated, see Table 6.1 for the specific coordinates of each control point. Note the fixed start and end coordinate of the y-axis, and that both the x and y-axis are normalised, such that the curves can be applied to any parameter or unit without much effort. Also visible is that the four control points result in six variables when the 0 and 1 y-coordinates are excluded.

Table 6.1: Control point coordinates of Bezier curve example

X-Coordinate	Y-Coordinate
0.3065	0
0.0951	0.6745
0.4348	0.7483
0.0613	1

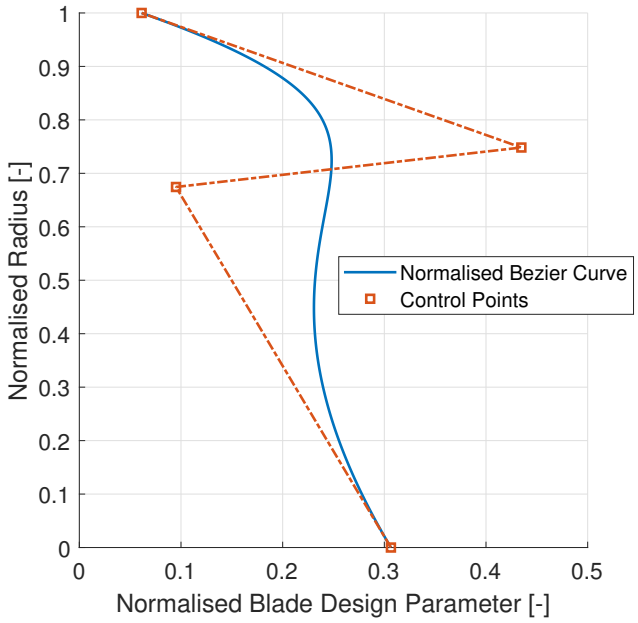

Figure 6.3: Bezier curve example

7

Surrogate Modelling

This chapter elaborates on the surrogate modelling that is performed in this in this study. In this study, data is generated from sources with a varying fidelity. This data is then combined into a multi-fidelity surrogate model. The idea is to create as many data points as possible using both high and low fidelity methods. Since a lot of different blade designs and operating settings are possible, it is not feasible to try every possible blade design. Therefore, a design of experiments is performed to generate a set of design vectors which cover the design space as well as possible. The design of experiments is discussed first in section 7.1, followed by the selection of surrogate modelling method in section 7.2. Contrary to the other described tools, the surrogate model accuracy is discussed along with the results in chapter 10.

7.1. Design Of Experiments Method Selection

The number of sampling points to a degree determine the accuracy of statistical and surrogate model results. According to Keane [34], the objective of design of experiments can be "to generate data that can be used to fit a regression model ... that reliably predicts the trends of the input-output relationship". This definition does agree with the objective in this study. To maximise the accuracy of the predictions of the meta-model, the sample points need to cover the complete range in the design space as well as possible. The design space can be represented by an N-dimensional hypercube, where N equals the amount of parameters. Some common and well known methods for sub-sampling are summarised below.

- **Monte Carlo Experiment** [34] [3]
  The Monte Carlo method relies on repeated random sampling to obtain unbiased results. Using an assigned probability density function, the method can fill the sub-sample space with random design points. A disadvantage of this method is that, due to the randomly assigned points, the algorithm may fail to cover the complete design space and it could explore only a certain area within the design space. To counteract this effect, many samples are required, which increases computational effort.

- **Latin Hypercube Sampling** [34] [3]
  The Latin Hypercube Sampling (LHS) method uses probabilities as well. The latin hypercube sampling technique can suffer from the same flaw as the Monte Carlo techniques, which is that the design space isn't necessarily filled well with sampling points if too few points are generated. This sampling technique was for example used by Zhang [35], in which a multi-objective aerodynamic optimisation with CFD and kriging was performed. In the creation of a multi-variate model, Urban [36] prefers latin hypercube sampling over other techniques such as various Quasi-Monte Carlo techniques. Urban, however, also notes that the Sobol sequence (see next item) has not been tested specifically.

- **Quasi-Monte Carlo Methods** [34]
  Quasi-Monte Carlo methods depend on low-discrepancy sequences. This sequences are in fact deterministic, instead of pseudo-random sequences used for Monte Carlo simulations. Well known methods include the Halton sequence, Faure sequence and Sobol sequence. Although these sequences appear random, they ensure a better spread of samples in the sample space compared to pseudo-random generated samples. The Halton sequence suffers from too much degradation beyond 14 dimensions, as

it shows correlation between various dimensions. Generally, Halton sequences are not used beyond 6 to 8 dimensions for this reason. The Faure sequence shows good performance up to 50 dimensions. The Sobol sequence performs the best regarding the number of dimensions, and would thus be the preferred method. Looking at research fields outside aerospace, Singhee [37] favours Sobol sequences in statistical circuit analysis over latin hypercube sampling in a direct comparison. An advantage that is mentioned is that since a Sobol sequence is sequential, new points can be generated afterwards. This is in contrast to latin hypercube sampling, for which a completely new grid is required when more points need to be added. In marine propeller design, the Sobol sequence has also been applied for an efficient optimisation routine [38].

- **Full Factorial Design** [34] [3]
  This sampling method covers the complete design space, by dividing the complete range of each variable into k levels. The corners of the hypercube, and sometimes interior points are selected. Although this method covers the design space very well, it is also computationally expensive since many points are required.

- **Fractional Factorial Design** [34] [3]
  With fractional factorial design sampling, only a fraction of the samples taken by full fractional design sampling are used. Although less points are required than for full factorial design, it is expected that other methods result in a better sampling of the design space with fewer points.

Full factorial design and fractional factorial design do not seem to be able to capture the design space as efficiently as the other methods and are therefore dropped. Examples of a random Monte Carlo sampling, Latin Hypercube sampling and a Sobol sequence can be seen in Figure 7.1, Figure 7.2 and Figure 7.3 respectively. Ten points are generated using each method. It is visible that the LHS and Sobol sequence provide a better spread in data points than the random Monte Carlo method. Although LHS and Sobol seem to perform the similar in this example, the author prefers the use of a Sobol sequence in this study. The reason is that a Sobol sequence allows to generate additional points afterwards, whereas LHS requires the complete data set to be changed when more points are required. Due to this flexibility, a Sobol sequence is used in this study for the design of experiments.

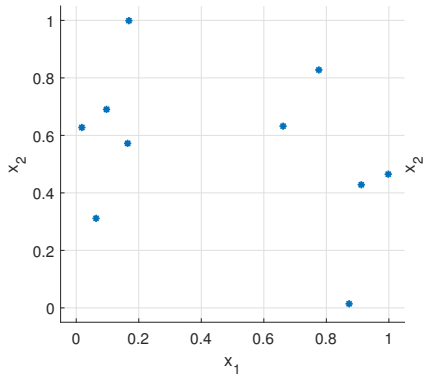

Figure 7.1: Monte Carlo sampling example

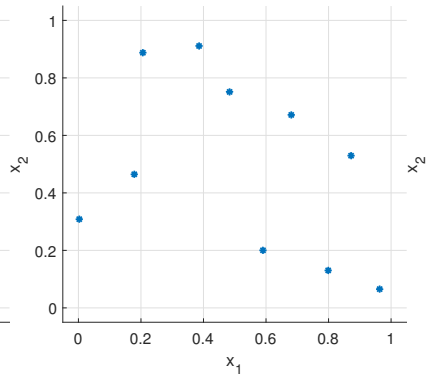

Figure 7.2: LHS example

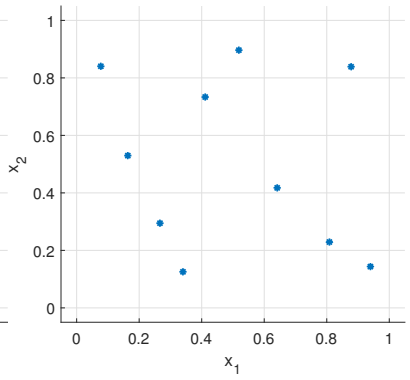

Figure 7.3: Sobol sequence example

7.2. Surrogate Model Selection

In this study, the results from two different methods with also a different level of accuracy are combined into a surrogate model. Some surrogate model types allow for multi-fidelity inputs by nature. Others are only single-fidelity by nature, but can be extended such that it is still possible to use multi-fidelity data. A division is made between multi-fidelity hierarchical models and multi-fidelity surrogate models. For the surrogate models, the main idea is to use high-fidelity results to correct low-fidelity observations. Fernandez-Godina identifies four correction methods [39]: multiplicative correction, additive correction, comprehensive correction and space mapping. Multiplicative and additive corrections are corrections on the low-fidelity model by either multiplying or adding a, often constant, ratio or value to the low-fidelity results. Comprehensive corrections use both multiplying and addition terms. Space mapping is a method of correcting the input variables by transforming the input vector for different models to obtain similar results.

In this subsection, some candidate surrogate models are listed and shortly summarised. Kriging is selected as surrogate model, the reasoning and conclusion for this are provided at the end of this subsection.

- **Response Surface Methods** Response Surface Methods (RSM) apply a set of polynomials of different orders to approximate the data points. The method was created with physical experiments in mind. Experiments usually include measurement errors. With RSM, the analysis of variance can be applied to measure the uncertainty of the polynomial coefficients [34]. With a t-statistic, low t-score coefficients can be dropped to improve the RSM accuracy [34].

  The response surface function is usually easy to create, but the drawbacks according to Marinus [3] are that the method is of limited use when complex input and output relations have to be modelled, which is the case with noisy, high-dimensional and multi-modal data. Amrit [40], however, has performed a multi-objective optimisation using response surface methods to explore the design space faster. This was done with RANS analysis with an SA turbulence model. Pagano [6] also uses RSM as a surrogate model in the multi-objective optimisation of propellers.

- **Neural Networks** Machine learning covers a broad area of prediction techniques used for classification and regression. A common technique is the use of neural networks. Here, a short description of neural networks is provided. Extensive information about machine learning methods can be found in [41]. In [42], the surrogate models use machine learning techniques for aerodynamic shape design of 2D airfoils and 3D turbomachinery blades.

  Neural networks consist of perceptrons, or neurons, which can realise an OR gate. The perceptrons are placed in hidden layers, in which they receive inputs directly from the input vector, or it uses the outputs of the perceptrons in hidden layers in front of it. After the hidden layer, the output layer either returns a value for regression, or a 1 or 0 for classification. A risk with neural networks is over-fitting. When this happens, the neural network reproduces the samples of the training set very well, but has not generalised the model, and the network will perform poorly on new data points. A drawback is the amount of hyperparameters that need to be tuned. The number of layers, number of neurons in each layer, activation functions, learning rate during training and more need to be defined. This means many data points are required to get a good model.

- **Kriging Methods** Kriging is a statistical approach invented by D.G. Krige [3]. Kriging assumes that the observed data points are not prone to errors, and is also referred to as a Gaussian process regression. Unlike many other methods, the created model will exactly reproduce the sample data points [34]. A visual comparison of the resulting interpolation is shown in Figure 7.4. Depending on the characteristics of the data set, different kriging methods are available. These include ordinary kriging and universal kriging amongst others. Ordinary kriging only uses one constant value to estimate the trend, whereas universal kriging uses additional parameters. The assumption of a Gaussian process is important to kriging, and observations from simulations or computer models do not necessarily comply to this assumption [43]. A stochastic process is Gaussian when all random variables have a multivariate normal distribution. Amrit [40] uses kriging successfully in transonic airfoil design.

According to Fernandez-Godino [39], response surface models are "being replaced by Kriging-like surrogates". Bayesian discrepancy and co-kriging are also being mentioned as candidate methods for multi-fidelity models[39]. Combining these statements with the finding of Marinus that the kriging model performed better than neural networks in terms of accuracy when compared to validation data [3] leads to the decision to use kriging as a surrogate model in this study.

The multi-fidelity kriging implementation is not created from scratch, instead an existing python package is used; the Surrogate Modelling Toolbox [44]. The underlying principles are shortly described.

Kriging uses stochastic process modelling as shown in Equation 7.1. Here, the interpolation result is denoted by $\hat{y}$, the linear regression coefficients by β_i, and the stochastic process by $Z(\mathbf{x})$. The known function is presented by $f_i(\mathbf{x})$.

$$\hat{y} = \sum_{i=1}^{k} \beta_i f_i(\mathbf{x}) + Z(\mathbf{x}) \tag{7.1}$$

The stochastic process $Z(\mathbf{x})$ is determined using Equation 7.2. It is assumed that the mean of $Z(\mathbf{x})$ is zero. The variance is given by σ^2, and R is the correlation function.

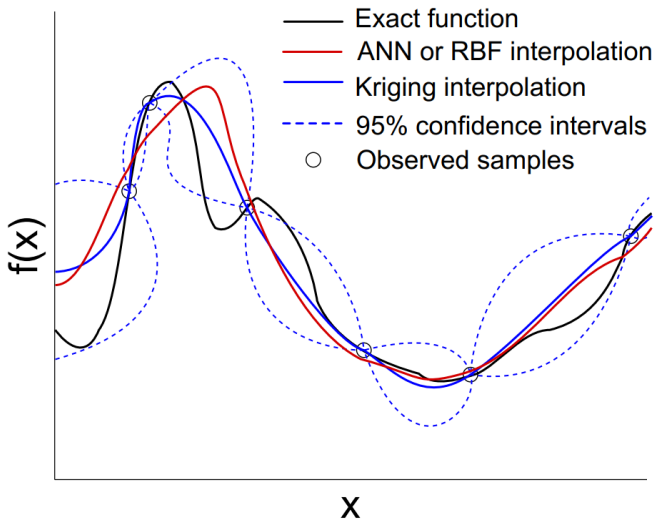

Figure 7.4: Interpolation Comparison Between Kriging and NN [3]

$$\text{cov}\left[Z\left(\mathbf{x}^{(i)}\right), Z\left(\mathbf{x}^{(j)}\right)\right] = \sigma^2 R\left(\mathbf{x}^{(i)}, \mathbf{x}^{(j)}\right) \tag{7.2}$$

Several correlation functions exist [3], but the most common function is the Gaussian function as shown in Equation 7.3. In this equation, θ_l denotes the hyperparameters that need to be tuned. In this case, the number of variables equals the number of hyperparameters. The hyperparameter are estimated by maximizing the likelihood, or minimizing the mean square error.

$$R\left(\mathbf{x}^{(i)}, \mathbf{x}^{(j)}\right) = \prod_{l=1}^{n_x} \exp\left(-\theta_l \left(x_l^{(i)} - x_l^{(j)}\right)^2\right) \tag{7.3}$$

The required computational effort rises drastically when more variables or dimensions are added to the problem. In this research, 5 variables are used, which is at the limit of the common maximum amount of variables used for kriging [1].

To allow for multi-fidelity kriging, an additional function is used which relates the high fidelity data to the low fidelity data. This is shown in Equation 7.4 [44]. In this function, $\rho(x)$ denotes the correlation factor, and $\delta(x)$ the discrepancy function. In the Surrogate Modelling Toolbox, the correlation factor can be either constant, linear or quadratic.

$$y_{\text{high}}(x) = \rho(x)\, y_{\text{low}}(x) + \delta(x) \tag{7.4}$$

The accuracy of the surrogate model is discussed in section 10.2.

[1] Source: https://smt.readthedocs.io/en/latest/_src_docs/surrogate_models/kpls.html, accessed at 13-08-2020

8

Workflow Implementation

This chapter elaborates on the implementation of the automated workflow.The workflow implementation is specifically discussed in detail in this chapter since the current implementation is considered essential for the realisation of the surrogate model in this research. Evaluating hundreds of propellers with two different flow performance methods, using another method for the computation of the TSSP and finally combining the results in one model requires consistent and reliable data streams. These issues are addressed in this chapter.

8.1. Workflow Implementation

As stated at the start of this chapter, the worfklow that is created for this research is considered essential by the author for the success rate of the complete approach in this study. Since many different steps are required to obtain the results from the initial set of design parameters, it must be made sure that each step has access to a consistent data set containing all required information, from the advance ratio range, to the flight conditions, to the mesh settings, etc. In addition, the process is required to run automatically for most steps since time-wise it is not possible to manually run each step for each propeller blade design. To the knowledge of the author, the created workflow is state of the art in the sense that a CFD mesh and simulation routine from commercial CFD software can be run autonomously on a variety of blades without manual interference after initial parameters have been set, and that the CFD results are processed without manual interference such that noise can be computed using the frequency formulation. The RANS method that is currently used can easily be replaced by other CFD methods which are available in ANSYS Fluent.

The workflow, from the start to the multi-fidelity model as end product, can be divided into three parts: design of experiments, performance and noise data generation from RANS and BEM, and the training of a kriging model. A visualisation of this can be found in Figure 8.1.

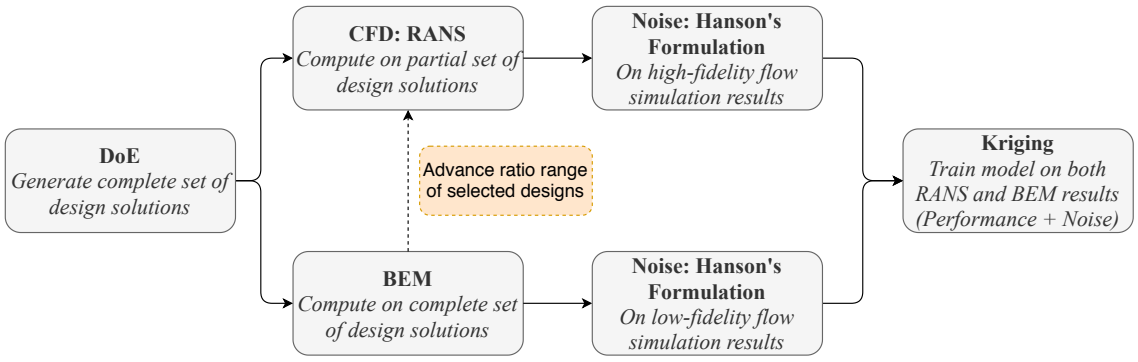

Figure 8.1: General data flow chart for the several tools used in this thesis

As can be seen in the chart, first a design of experiments is performed to generate a set of design solutions within a given design space. After this set has been created, all design solutions are evaluated using BEM. A fraction of the designs is evaluated using RANS as well. As little is known about the feasible operational regime for the generated propellers, a valid advance ratio range for each RANS simulation is obtained from

the BEM analysis of the propellers. After the flow properties are computed, the TSSP can be computed using the results from each method. After both the performance and noise characteristics are determined, they can be used to train a kriging model. A kriging model is trained separately for each quantitity. This means that a separate model is created for the thrust coefficient, efficiency and TSSP.

Design of Experiments

As explained in chapter 7, a Sobol sequence is used to generate pseudo-random designs. In this low cost step, each design variable is assigned to a separate dimension. This means that for sweep alone, already a 3-dimensional sequence is created. When including pitch, twist and chord length, this comes down to a 14-dimensional Sobol sequence. The implementation allows for all blade parameters to be varied, even though in this study only the blade sweep and pitch angles are varied.

Since the Sobol sequence is low cost to generate, a set of 15000 designs is generated at the initialisation of the workflow. A random number generator seed ensures that the same sequence is generated at each initialisation. Next to the Sobol sequence, all other method parameters and settings are set during initialisation. These settings can be accessed by each method at each step, ensuring a consistency of settings throughout the complete workflow.

Data Generation

In this stage, the data required for the Kriging model is generated. After selecting the blade design parameters to be varied, and the number of different designs to be evaluated, the process is started. For the BEM analysis, the workflow is straightforward. Immediately after the design blade design vectors have been generated from the Sobol sequences, the designs are evaluated. Both the total results as well as the separate conditions at each radial segment of the blades are stored.

For the CFD analysis only a fraction of the generated designs is evaluated. Suitable blades and advance ratios are determined when the blade is created and analysed using the BEM analysis. Initially, the Mach number and angle attack at each cross-section of the blade are computed without induced velocities for a range of advance ratios between 0.1 and 10. Next, the ranges are limited such that the Mach number should be below 0.75, and the absolute angles of attack cannot be higher than 18 degrees. Each advance ratio within this range is then used in the BEM analysis, after which only a small set of realistic advance ratios is obtained. This feasible set can then also be used for the CFD computations. The automated CFD workflow is more elaborate than the BEM workflow. Implementing such workflow posed several problems which had to be overcome. For example, a routine had to be created which automatically uploaded, submitted and downloaded back CFD files to and from the computer cluster to which the author had access to. This routine could also detect failures, such as license or RAM failures, which randomly occurred. The jobs were automatically resubmitted when such a failure was detected. In the final workflow, a combination of MATLAB, Python, Iron Python and Scheme programming languages have been used along with ANSYS Workbench, ANSYS SpaceClaim, and ANSYS Fluent software packages. A step-wise explanation of the essential workflow steps is provided next.

1. **Propeller Geometry File Generation**
   The geometry file generation step is visualised in Figure 8.2. First the propeller blade geometry is created from the parametrized design vector. The blade is radially divided into several airfoil cross-sections, after which all coordinates are written to a text file. Next to the coordinate file, another file is created containing the computational domain sizes, mesh refinement box positions and nacelle and spinner dimensions. Additionally, an ANSYS Journal file is created containing mesh and solve settings which are required for automating ANSYS Fluent. To summarise, the output files created in this stage are:

   - Propeller blade coordinate file
   - Dimension file for computational domain
   - ANSYS Fluent mesh Journal file
   - ANSYS Fluent solve Journal file

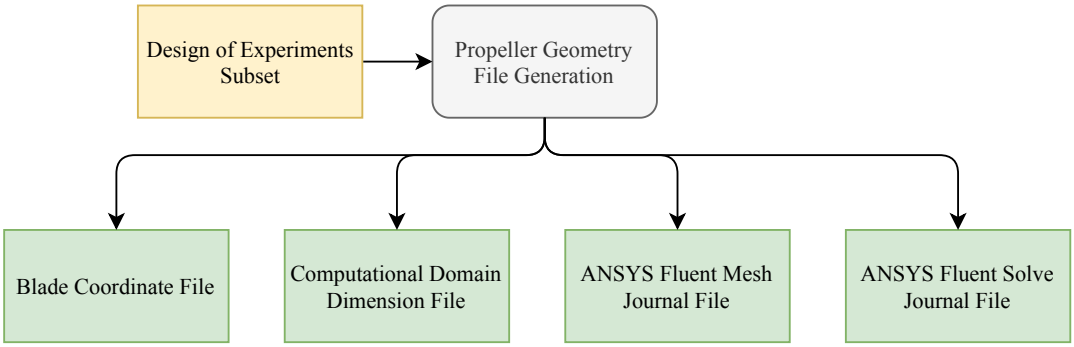

Figure 8.2: Automated CFD implementation step 1

2. **Propeller Geometry Creation**
   In this second stage, visualised in Figure 8.3, the propeller blade coordinate file and dimension file are used to generate a CAD geometry and computational domain of the propeller. This is done in ANSYS SpaceClaim. SpaceClaim allows for scripted geometry generation, although this is experimental and relatively undocumented. It also supports named selection within the ANSYS environment which is useful in the next steps. SpaceClaim can be run from the command line, and can thus be automated, by calling ANSYS workbench in batch mode. An existing workbench file has to be pre-configured to be able to do this. The SpaceClaim instance which is run by workbench contains a script written in IronPython V2.7 which reads the coordinate files, generates the geometry and domains, includes named selection (inlet, outlet, etc.), and saves this to a CAD file. The output file in this stage is:

   - Propeller CAD geometry & computational domain

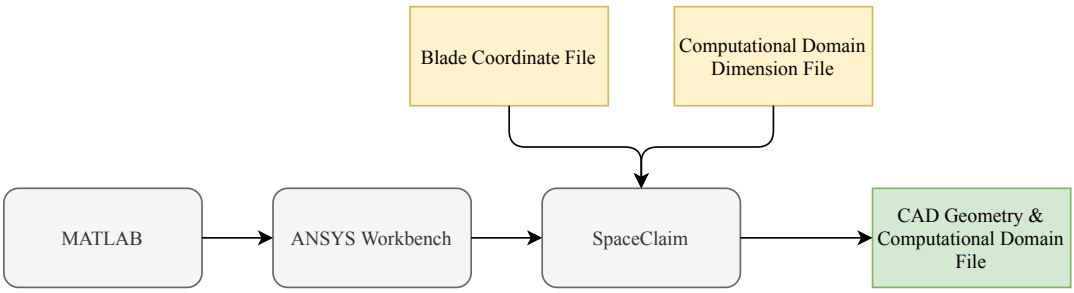

Figure 8.3: Automated CFD implementation step 2

3. **Propeller Meshing**
   The third step is meshing the geometry in ANSYS Fluent. A flow chart of this is shown in Figure 8.4. A MATLAB script calls Fluent from the command line, and combines the correct Journal file from step 1 with the correct geometry from step 2. The Journal file contains all necessary mesh settings for Fluent to mesh the geometry. The information includes minimum and maximum mesh cell sizes, curvature refinements, refinements based on named selections, mesh type, number of inflation layers, etc. The final mesh is then saved again to the disk. The output files of this stage are:

   - Geometry mesh file
   - Mesh log file

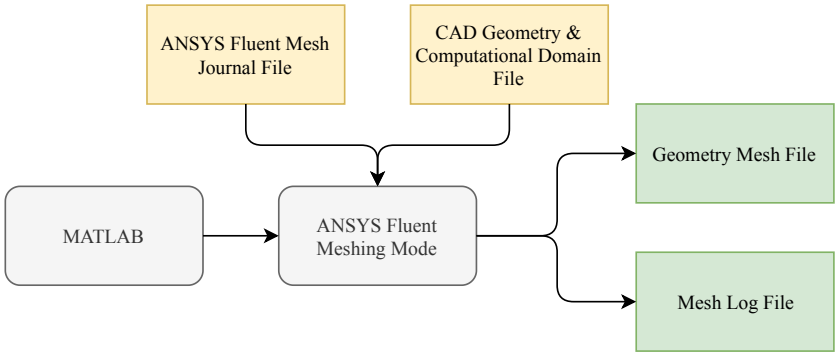

Figure 8.4: Automated CFD implementation step 3

4. **Propeller Flow Simulation**
   In this stage, shown in Figure 8.5, the flow around the propeller is simulated using the mesh and Fluent solve Journal from the previous steps. Using MATLAB, the required files are uploaded to the cluster computer and the job is submitted. The MATLAB script also keeps on checking the log file for errors. If errors are encountered in the log file, due to RAM or license errors, the job is resubmitted. When the simulations succeeds, several files are saved including the complete simulation results, total forces and moments on the blade, and all mesh cell values. The output files of this stage are:

   - Solve log file
   - Flow result data file
   - Total force and moment files
   - Run-time log file
   - Raw blade surface data files

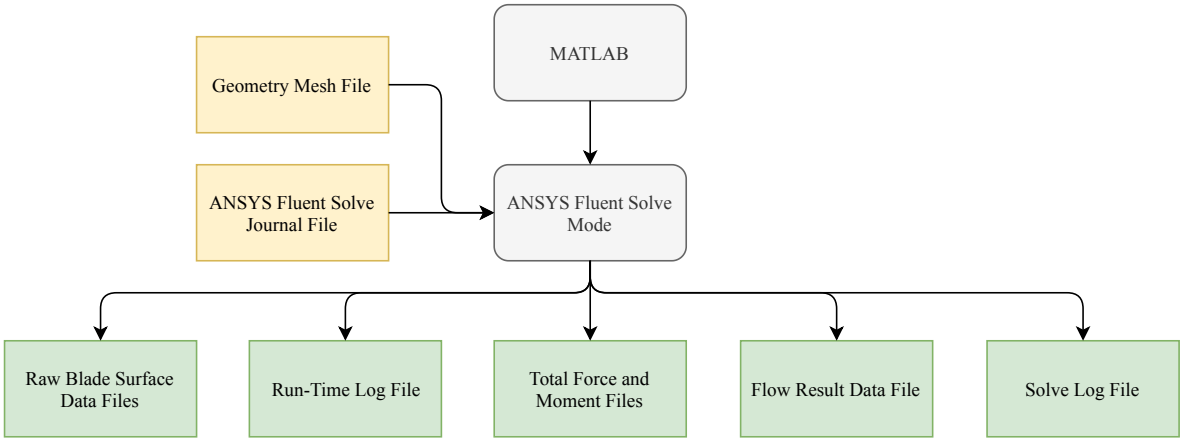

Figure 8.5: Automated CFD implementation step 4

5. **CFD Data Extraction**
   In this stage, the output data from the flow simulation stage is processed such that it can be used for noise computation and additional analysis. This procedure includes interpolation and the determination of normal vectors, and is visualised in Figure 8.6.

   - **Divide upper/lower blade**
     First, the upper and lower airfoil parts of the blade are divided. This is done by creating interpolated upper and lower blade models based off the original geometry based on the design vector. For this to work, any sweep and rotation are reversed for both the original blade and CFD blade, such that the upper and lower airfoils can be divided along an axis. The interpolants take the

chord-wise and radial locations as input, and have the airfoil thickness coordinate as output. All mesh cell coordinates from the CFD blade are inserted in both the upper and lower airfoil interpolants. The resulting interpolated thickness coordinates are then compared with the actual mesh cell coordinates. The upper/lower airfoil label is then assigned to whichever interpolant gives the closest approximation compared to the mesh coordinate.

- **Interpolate CFD mesh cell results**
  Knowing the indices of the upper and lower cell points, interpolants can be made from the pressure data and node location data using the de-rotated data. A grid is made from chord length x and blade radius, after which the corresponding pressure and thickness values are found. Next, the grid coordinates are transformed back to the swept and rotated state.

$$R = \begin{bmatrix} \cos\theta & -\sin\theta \\ \sin\theta & \cos\theta \end{bmatrix} \tag{8.1}$$

- **Surface normal and area computation**
  The grid points are then divided into triangles, and the normal and area are computed. By taking the cross product of two vertices of a triangle, the normal vector is computed. To make sure that the normal is pointing outward, Equation 8.2 is used to determine the angle of the normal vector each face to the angle to the mean chord line. In this case, v and u represent the two vectors, and θ is the angle between them.

$$\cos\theta = \frac{u \cdot v}{\|u\| \cdot \|v\|} \tag{8.2}$$

- **Final value computation**
  The last step is to use Equation 8.2 again to determine the relative angles between the normal and the x, y and z-axis. Having determined this, pressure forces can be easily decomposed along each axis. The shear is included as well.

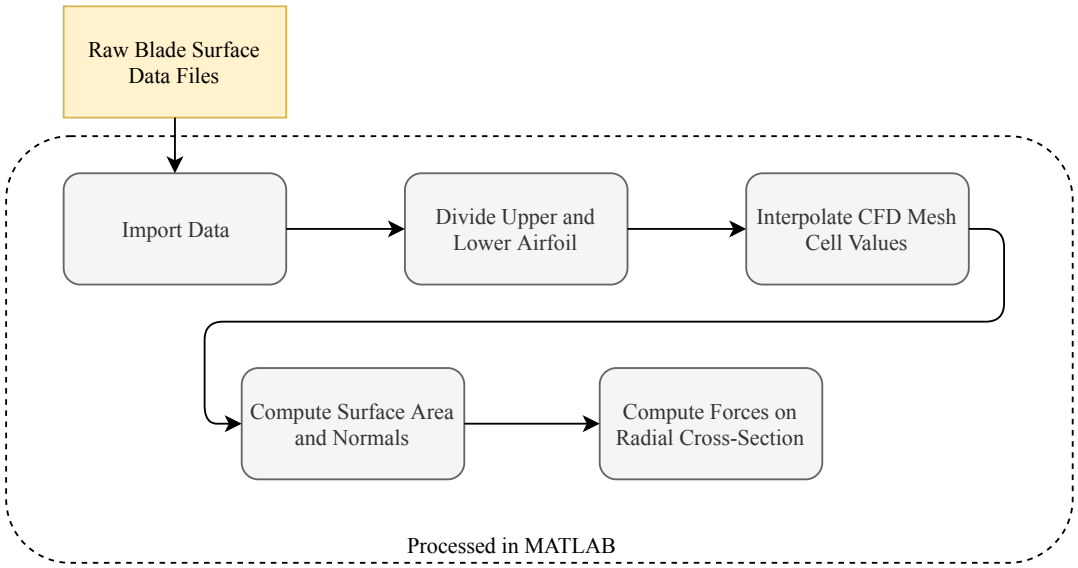

Figure 8.6: Automated CFD implementation step 5

The noise determination is fairly straightforward for both the RANS and BEM data. See chapter 5 for more on the the noise computations. The sectional loading distributions from BEM are obtained directly from the analysis, while the distribution from the CFD analysis are obtained in the CFD data extraction step.

Creating a Kriging Model

As explained before, the Surrogate Modelling Toolbox [44] is used to create kriging models. When the noise is computed, the low and high fidelity results and design variables are written to CSV files. These files are then imported by the kriging script in Python.

Before the kriging models are created, all data is scaled using the standard scaler from the SKLearn package[1]. For the advance ratio, an additional normalisation is applied first using the relation from Equation 8.3. This normalisation centres the advance ratios around 1, more or less independent of the collective pitch angle. Reducing advance ratio dependence to the pitch angle results in better output from the kriging model.

$$J_{norm} = \frac{J}{2 \cdot \tan\beta_{0.7}} \tag{8.3}$$

After these steps, the kriging models can be trained, after which design points can be inserted into the models which then provide the C_T, η and TSSP as output.

[1] Source: https://scikit-learn.org/stable/index.html, accessed at 13-08-2020

III

Tool Error Analysis and Results

9

Verification & Validation of Tools

Before any results are generated, the aerodynamic, aeraocoustic and parametrisation tools are verified and validated first. The surrogate model accuracy is discussed along with the results in chapter 10. In the following sections, first the RANS and BEM verification are performed in section 9.1 and section 9.2. RANS verification is discussed first since RANS results are used in the BEM verification. The RANS verification includes the determination of the number of inflation layers and a grid dependency study to estimate the discretisation error of the chosen grid. The BEM verification is meant to show BEM dependency to sweep. It also includes a dependency check to the number of radial stations used in the BEM analysis. section 9.3 elaborates on the validation of the BEM and RANS methods using experimental data from the XPROP propeller, shown in Figure 9.49. The noise tool is verified in section 9.4. Lastly, the parametrisation errors are investigated in section 9.5.

9.1. RANS Verfication

In this section, the required number of inflation layers is determined and a grid dependency study is conducted to quantify the grid discretisation error.

9.1.1. Determination of the Number of Inflation Layers

Before the refinement on all sizing parameters is done, an initial estimate on the required number of inflation layers is made first. This estimate is made by evaluating a variety of sizing settings at different numbers of inflation layers from 5 to 25 in steps of 5. By then averaging the results per number of inflation layers, an initial estimate could be established. The advance ratio was varied between 0.7 and 1.2 with steps of 0.1. It is desirable to limit the inflation layer size as it heavily impacts the grid size and therefore the required computational time of the solver. However, the inflation layer should be large enough to capture important characteristics of the boundary layer. The effects of the number inflation layers on the C_P are presented in Figure 9.1. It is visible that from about 20 inflation layers onward, the C_P does not change much. The C_P difference between 20 and 25 inflation layers is less than 0.005 on average, which can be seen more clearly in Figure 9.2. This difference is deemed small enough to continue using 20 inflation layers for the remainder of this study.

9.1.2. Grid discretisation Error

By using a poly-hexcore grid, much of the grid is structured with only few irregular poly-shaped cells at curved regions. The inflation layer consists of prism layers and is located at the spinner and blade. Fewer and coarser inflation layers are placed behind the blade and spinner on the nacelle, this can be seen in Figure 4.1. This is done to have the inflation layer disappear more smoothly, and it improves the simulation stability at various mesh refinements. The grid density is controlled by multiplying all sizing parameters with a certain factor. If interested, all grid sizing parameters are listed in Table A.1 in Appendix A.

Grid size 3 from Table 9.2 is taken as reference and is intended to be used for the remainder the study. The results of this routine are shown in Figure 9.3 and Figure 9.4. The presented results are for $J = 0.7$, using the flow conditions from Table 9.1. Both C_T and C_P show a reasonable convergence with low standard deviations as can be seen from Table 9.3. The best order fit for the thrust coefficient is almost linear at $p = 1.02$, while

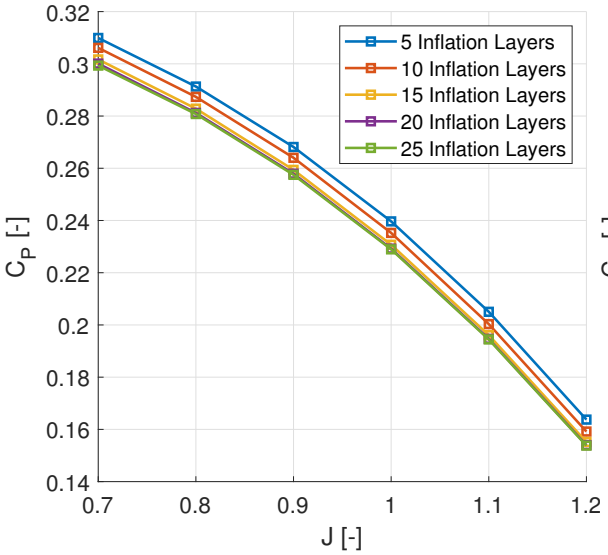

Figure 9.1: C_P comparison for varying numbers of inflation layers on the XPROP

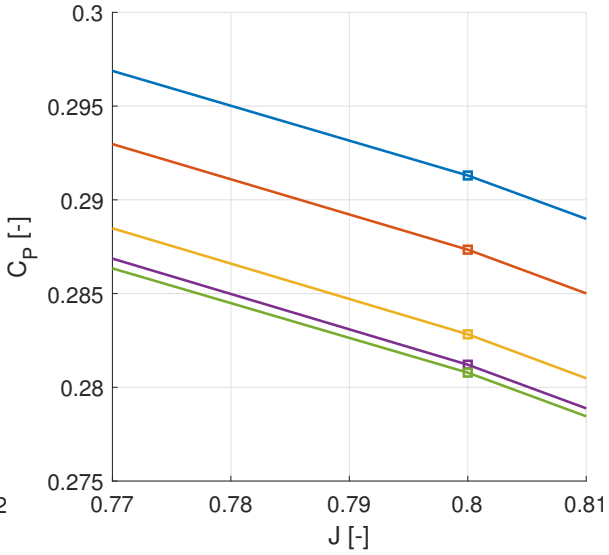

Figure 9.2: Zoomed-In C_P comparison for varying numbers of inflation layers

the fit for C_P shows non-linear behaviour at $p = 2.42$. The estimated discretisation error U_ϕ for the thrust coefficient is 0.93%, while the estimated error for the power coefficient is 1.00%. The results are considered sufficient for the continuation of this study.

Table 9.1: Flow conditions grid dependency study

Flow Condition	Value	Unit
V_∞	30	[m/s]
p_∞	101325	[Pa]
T_s	298.15	[K]

Table 9.2: Grid sizes used in dependency study

Grid	Number of Cells	h_i/h_1
5	977575	1.58
4	1125343	1.51
3	1937330	1.26
2	2342716	1.18
1	3854970	1.00

Table 9.3: Results from grid dependency study for grid 3

	C_T	C_P
p	1.02	2.42
U_s	0.05	0.06
U_s*	0.06	0.06
U_ϕ, %	0.93	1.00

9.2. BEM Verification

With the BEM method being implemented from scratch, verification is required. To evaluate whether the BEM implementation has a reasonable dependency to sweep, verification is performed by generating three blades with a random sweep distribution and comparing the BEM results with CFD results. With exception of the sweep, these blades share the same geometry as the XPROP propeller with a 0.2032 m radius shown in Figure 6.1. The verification also includes a short investigation to the ambiguities on the sweep definitions raised earlier. Secondly, the dependency of the BEM solution to the number of radial stations is checked.

9.2.1. Verification with Random Sweep Distribution

No experimental data from a propeller with a swept blade is available to the researcher. To still be able to investigate the dependency of the new BEM implementation to sweep angles, three blade designs are generated with random sweep. These three blades are then evaluated using both BEM and CFD. The latter analysis method is discussed in chapter 4. A detailed explanation of propeller blade generation and parametrisation is provided in chapter 6. In this verification procedure, the XPROP blade is taken as reference. The airfoil cross-sections, chord, collective pitch and twist are the same. The only change is the addition of sweep to the airfoil sections.

The three random swept blade designs are presented in Figure 9.5, Figure 9.6 and Figure 9.7. Design 1 is swept backward from the root to about half the radius, at which a forward sweep is applied. Design 2 exhibits forward sweep from the root to a third of the blade radius, after which a strong backward sweep is present. Design 3 is a mainly slight backward swept blade, with low local sweep near the tip.

The local mid chord sweep angles in the plane of rotation of each design are shown in Figure 9.8. These

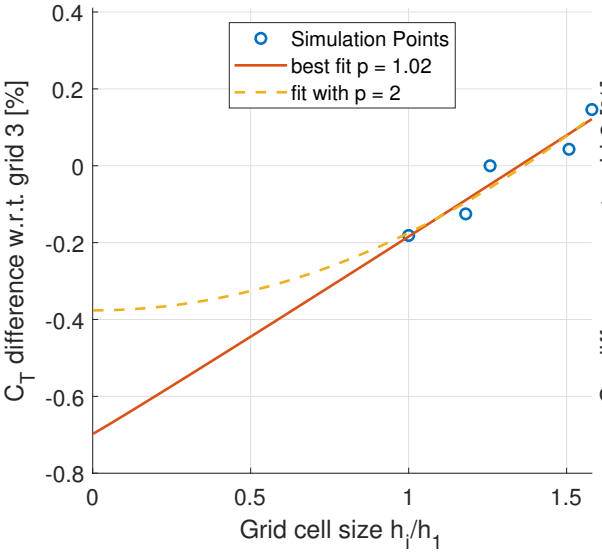

Figure 9.3: CFD thrust coefficient difference w.r.t. grid 3 at J = 0.7

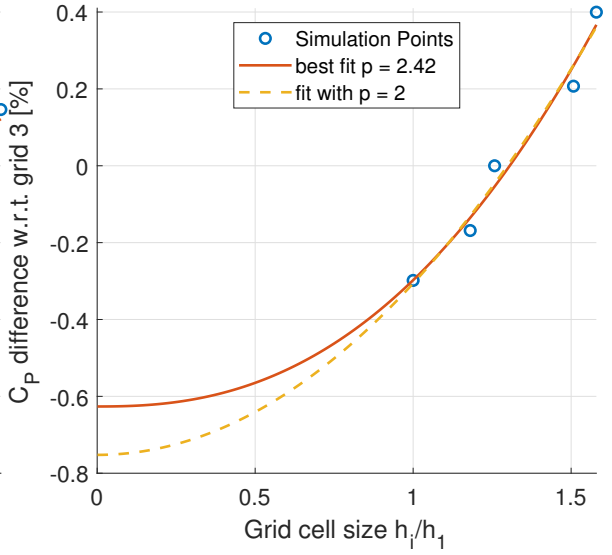

Figure 9.4: CFD power coefficient difference w.r.t. grid 3 at J = 0.7

angles are shown for blades without pitch and twist. The figure shows a sufficient spread in sweep angles for the verification purposes. A discontinuity is visible where the sweep is fixed to zero at the root of the blade. This is not an error, but the result of the constraint that the root has zero sweep. This is done to ensure that the blade is build up centred from inside the spinner. The translation of sweep is parametrised, and visualising this in Figure 9.9 shows that the parametrisation is smooth. The local sweep angle discontinuity does not affect the CFD simulations since these depend on the 3D geometry, but it may affect the BEM results. The possible effect of the sweep angle discontinuity on the BEM results investigated at the end of this subsection in Figure 9.2.1. The out of plane translation that is visible is only taken into account by the CFD analysis. The root airfoil section of the blade starts at 0.16 radius. The flow conditions, including the velocity, are presented in Table 9.4.

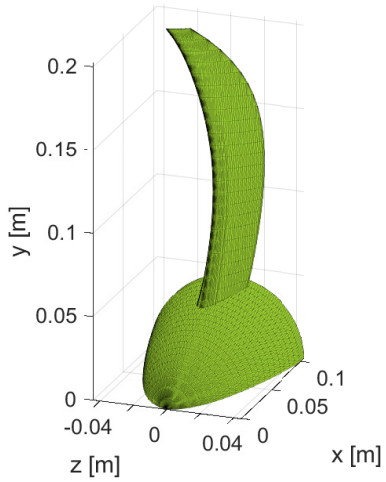

Figure 9.5: Random swept blade design 1

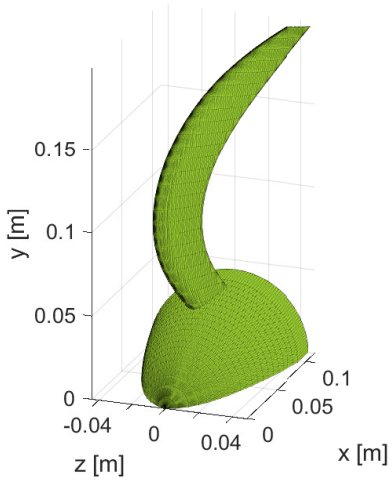

Figure 9.6: Random swept blade design 2

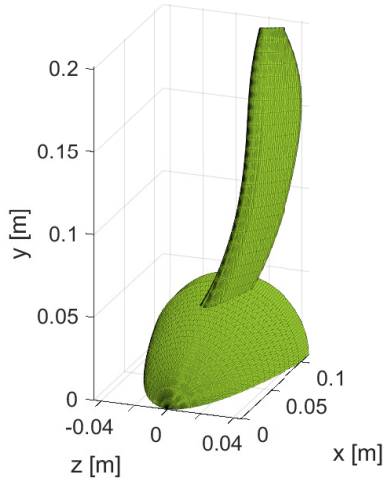

Figure 9.7: Random swept blade design 3

The ambiguities surrounding sweep are investigated first. This is done by plotting the thrust coefficient curves for the definition options. In Figure 9.10, the differences between 0.25C sweep and 0.5C sweep are shown for the thrust coefficient. The CFD results are plotted next to the BEM results as well. The differences between the two sweep definitions are small. For design 2 and 3 a half chord sweep slightly improves the similarity to the CFD results, while for design 1 the discrepancy is slightly increased. Since it can be reasoned that the out of plane movement of the leading edge and trailing edge should be averaged, it has been decided to use the half chord sweep in this study.

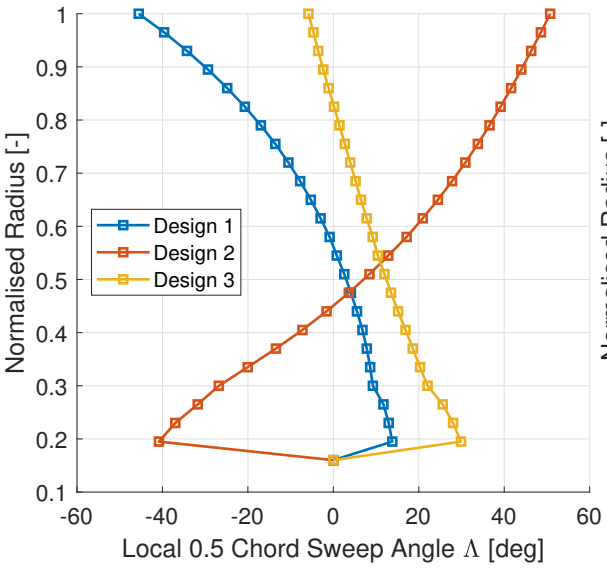

Figure 9.8: Local zero twist sweep angle vs normalised radius

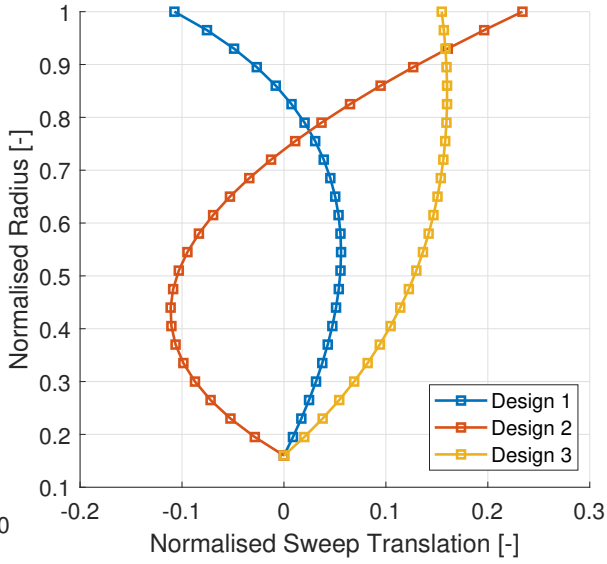

Figure 9.9: Normalised smooth sweep translation as generated making use of a Bezier curve

Table 9.4: Flow conditions for BEM verification

Flow Condition	Value	Unit
V_∞	60	[m/s]
ρ	1.225	[kg/m^3]
p_∞	101325	[Pa]
T_s	288.15	[K]

Regarding the fixed or variable sweep in relation to the pitch angle, Figure 9.11 should be inspected. Although design 3 does not show large differences, the results from design 1 and 2 indicate larger discrepancies when defining the sweep before twist and pitch rotation is added to the blade sections. Due to this, the local sweep in this research will be projected onto the actuator disk after the twist and pitch have been applied. This means that the sweep used in the BEM computations changes when the pitch angle is adjusted.

BEM sensitivity to the application of sweep is clearly visible when looking at the analysis results. Plots of the BEM and CFD results for C_T, C_P and efficiency can be found in Figure 9.12, Figure 9.13 and Figure 9.18. The BEM and CFD analysis of design 1 show a small but constant offset for both the C_T and C_P. The BEM analysis under predicts the C_T by approximately 0.0073, and the C_P by 0.0091 on average. The discrepancy in power coefficient does reduce at lower advance ratios. Whereas the BEM analysis underpredicted the coefficients for design 1, the opposite is the case for design 3. Both the thrust and power coefficients are overpredicted compared to the CFD results, but the discrepancy decreases as the advance ratio increases. Looking back at Figure 9.8, it is suggested that the underprediction and overprediction may occur due to the tip sweep, which is almost zero for design 3 but over 40 degrees forward for design 1.

Design 2 shows large discrepancies for both the C_T and C_P. It is suggested that this may partially be explained by the large out of plane deflection occurring with this blade. This out of plane translation is not accounted for in the BEM analysis.

To investigate the differences further, the blade thrust distributions for design 1, 2 and 3 are visualised in Figure 9.14, Figure 9.15 and Figure 9.16 respectively. These distributions are taken at $J = 1.15$, which is approximately at the advance ratio of maximum efficiency for the propeller designs (Figure 9.18). For the CFD distributions, the blade is radially discretized in 50 segments. The BEM distributions are discretized in 25 segments. Each bar represents the average loading that is computed on the radial segments. Investigating the blade loading for the three blades shows that, regarding the RANS analysis, all blades have a higher loading near the tip than the root. This is in line with what is expected for efficient blades. A notable difference between all BEM and CFD loadings is present at the root of each blade. The BEM analysis consistently shows a negative loading at the root of the blade, but in the RANS analysis the magnitude of the loading at the root is much smaller. It is likely that these are spinner/root interaction effects which are captured by RANS, but

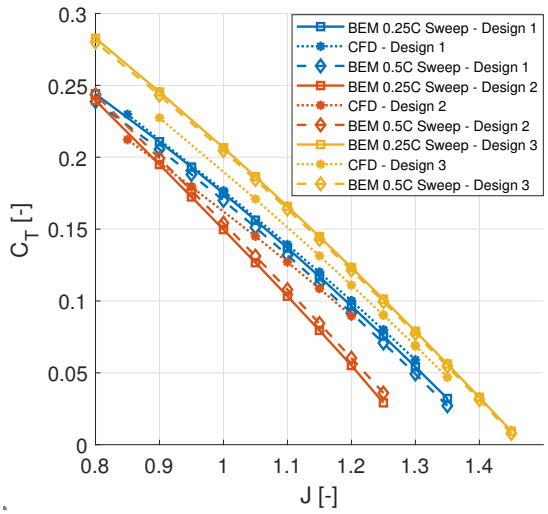

Figure 9.10: Thrust coefficient comparison for 0.25C sweep and 0.5C sweep

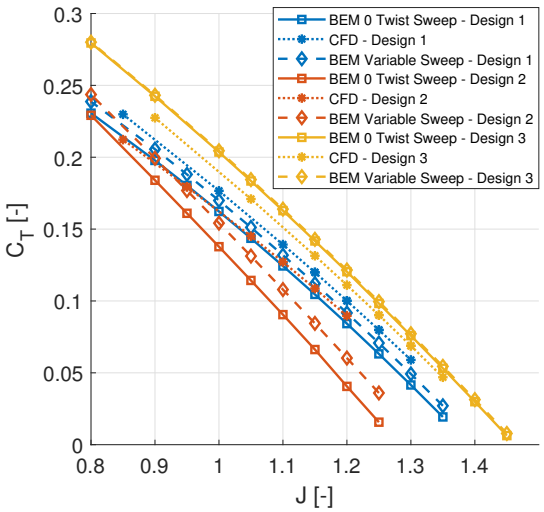

Figure 9.11: Thrust coefficient comparison for a fixed and variable local sweep definition

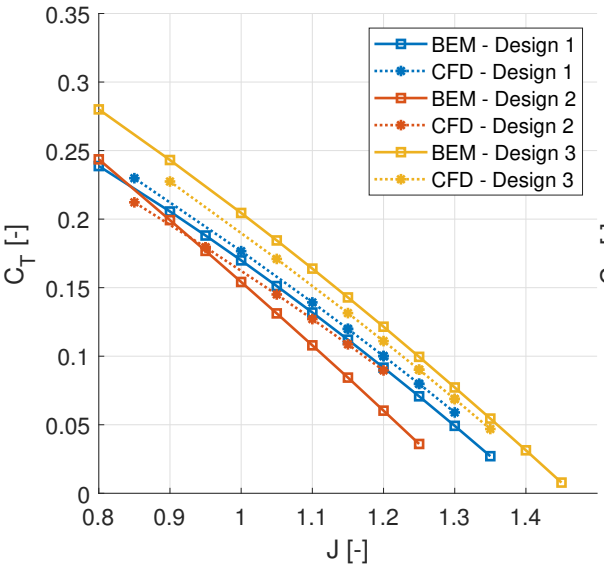

Figure 9.12: Thrust coefficient comparison between BEM and CFD for randomly swept blades

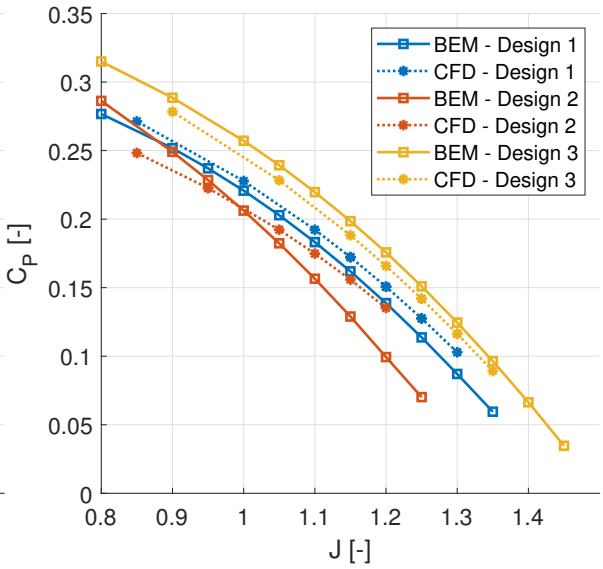

Figure 9.13: Power coefficient comparison between BEM and CFD for randomly swept blades

not taken into account by the BEM analysis.

The computed loading distributions for design 2 differ clearly. The BEM analysis shows large root losses, it estimates the highest loading to be close the middle of the blade and the loading becomes negative towards the tip. The RANS analysis still shows a high tip loading. It is possible that vortices are formed on the blade which result in the difference between the BEM and RANS analysis. The tangential force distributions for design 2 are shown in Figure 9.17. In this figure, the loading the CFD evaluation shows that the peak of the tangential forces is slightly closer to the tip than the BEM distribution. Close to the tip, the BEM distribution shows small forces, while the CFD distribution indicates a large spike.

Comparing the distributions suggests that the BEM analysis locates the position of highest loading more towards the root with a increase in tip sweep. A higher out of plane movement may also be the cause of the wrong location of highest loading, as design 2 has a similar but mirrored tip sweep compared to design 1, but the point of highest loading is moved more towards the middle of the blade radius.

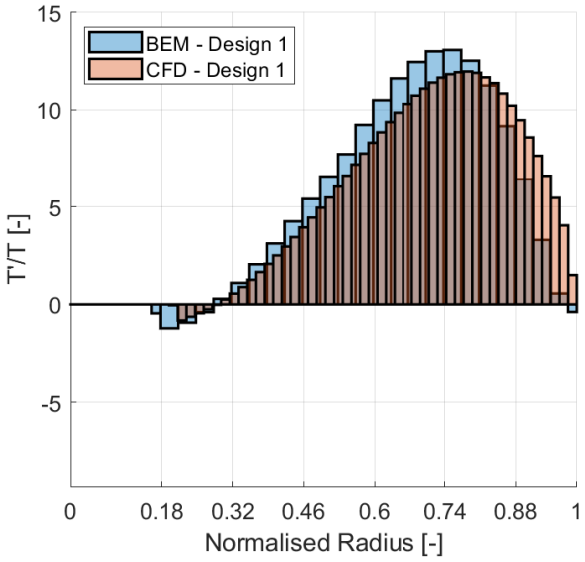

Figure 9.14: Radial axial force distributions for design 1 at $J = 1.15$

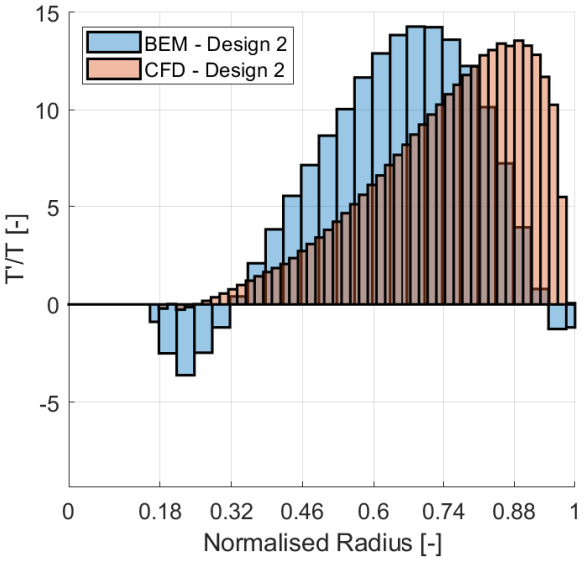

Figure 9.15: Radial axial force distributions for design 2 at $J = 1.15$

Looking at the efficiencies in Figure 9.18, the CFD and BEM analysis are much in agreement for design 1. Although there is a difference in the computed thrust and power coefficients, this offset is constant, which shows in the efficiency. The BEM analysis over estimates the efficiency of design 3 compared to the CFD analysis. This is due to the offset of the C_T being larger than the offset of the C_P, which results in a higher efficiency. Due to the differences seen in thrust and power coefficient for design 2, a large discrepancy in efficiency is seen as well.

Although perfect agreement is not shown between the RANS and BEM analysis, it can be concluded that the BEM implementation does show a reasonable sensitivity to sweep. In all three cases, BEM and RANS show similar behaviour when sweep is applied. Since the BEM and RANS results will be combined in a multi-fidelity model, the current results are deemed acceptable by the author of this work.

Investigation of the Local Sweep Angle Discontinuity at the Root

To investigate the effect of the sweep angle discontinuity at root of the blade, the sweep angle of the cross-section of the root airfoil is adjusted such that it has the same value as the second defined section at a radius of approximately 0.2R. This is shown in Figure 9.19.

The results for both the original mid chord angle distribution and the adjusted distribution are presented in Figure 9.20 and Figure 9.21 for the C_T and C_P respectively. It is clear that the BEM results have barely changed by the root angle adjustment. This is quantified in Table 9.5, in which the average values of the absolute differences for each design are presented. The largest difference is obtained for design 2.

The fact that such small differences appear can explained due to the way the root and tip sections are handled by the BEM method. Segments with an area are required for the BEM analysis. With exception of the root and tip segment, all other segments are defined such that a station is positioned in the middle of segment. The root and tip station are used in an interpolation to obtain root and tip segments. Due to this,

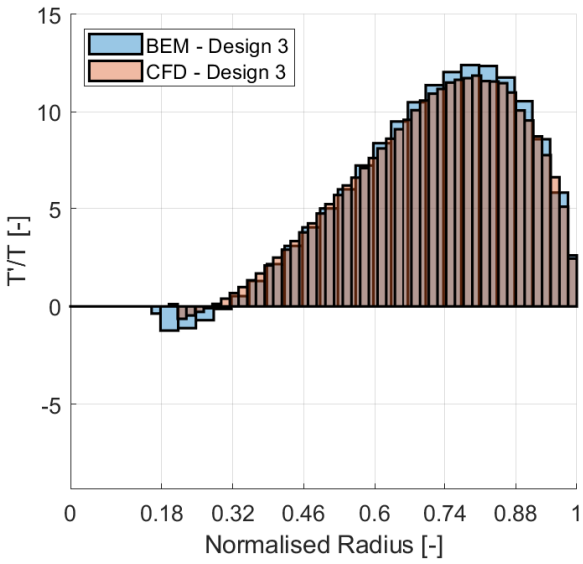

Figure 9.16: Radial axial force distributions for design 3 at $J = 1.15$

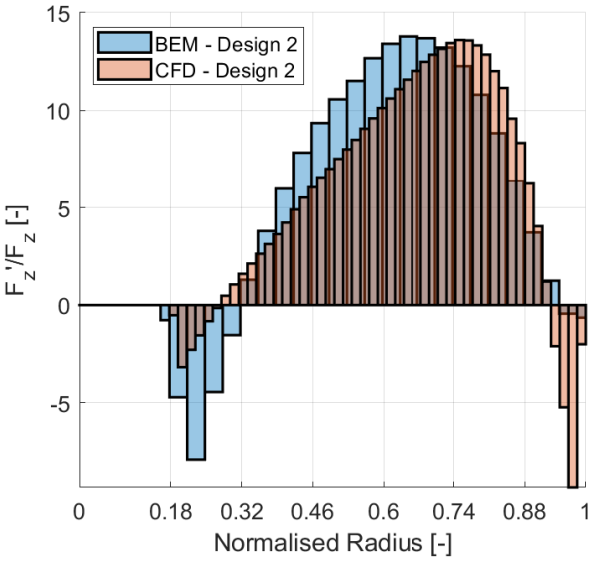

Figure 9.17: Radial tangential force distributions for design 2 at $J = 1.15$

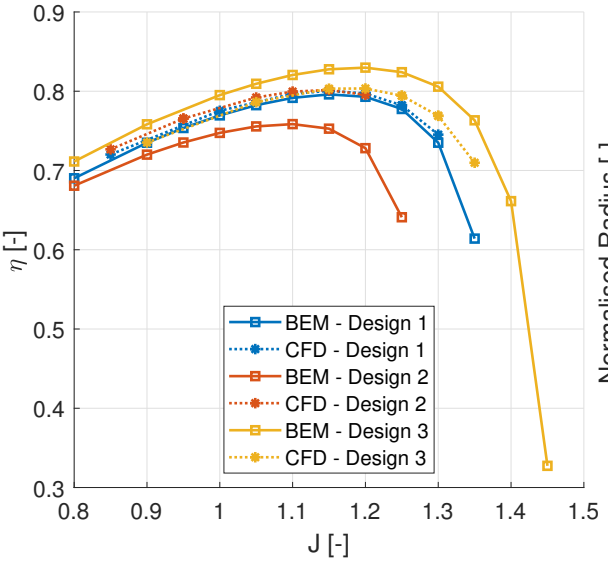

Figure 9.18: Efficiency verification of randomly swept blades by comparing BEM and CFD evaluations

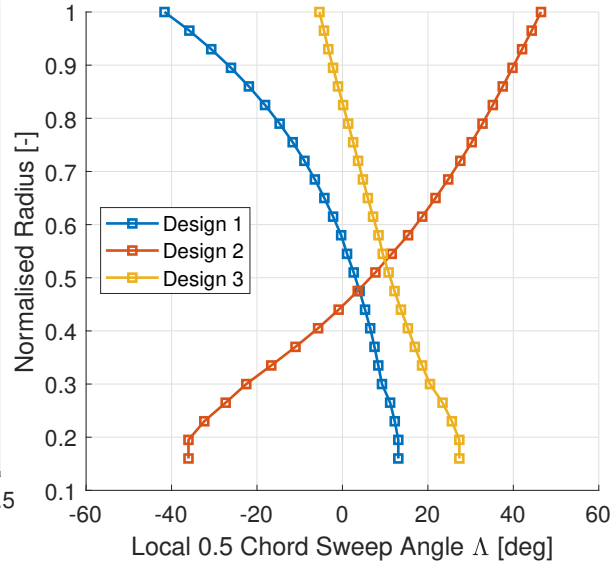

Figure 9.19: Local zero twist sweep angle with adjusted root section

Table 9.5: Mean absolute differences between the cases for a swept root section or zero sweep at the root section

Design	**Mean ΔC_T [-]**	**Mean ΔC_P [-]**
1	1.18E-05	1.22E-05
2	1.74E-04	1.71E-04
3	6.31E-05	5.86E-05

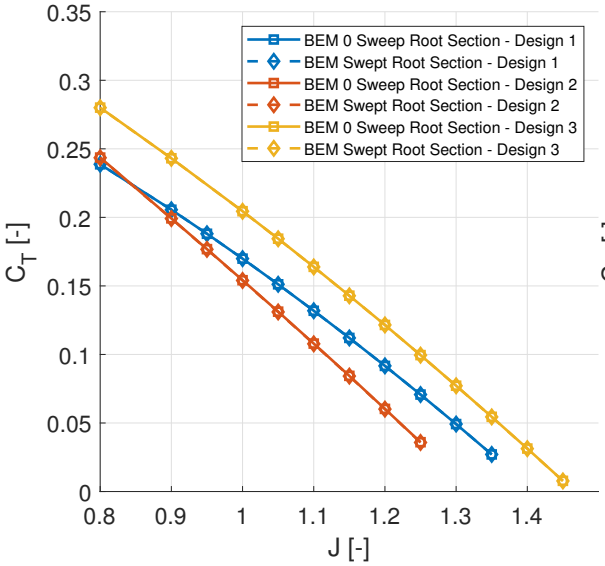

Figure 9.20: Thrust coefficient comparison of BEM analysis results for blades with zero root section sweep and blades with root sweep

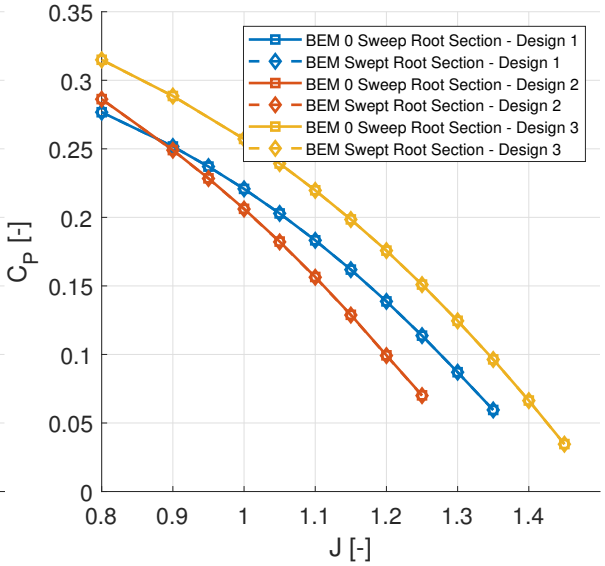

Figure 9.21: Power coefficient comparison of BEM analysis results for blades with zero root section sweep and blades with root sweep

the root segment actually does have a sweep in the BEM analysis, although the defined root airfoil section does not.

9.2.2. Dependency to Number of Radial Stations

To determine whether the current 25 radial stations used in the BEM analysis are sufficient for reliable results, a short dependency study is carried out. In this dependency study, the radial stations at the root and tip are untouched, but some stations in between are removed. Table 9.6 shows the number of stations used. The maximum number of stations, 25, is used as benchmark. In this study, the XPROP is used. The results shown in Figure 9.22 and Figure 9.23, for the C_T and C_P respectively, show that using less stations results in a low discrepancy between the curves.

Table 9.6: Radial stations used in BEM dependency study

Radial Station Setting	Number of Radial Stations	h_1/h_i
1	25	1.00
2	15	1.67
3	11	2.27
4	10	2.5

The errors for the thrust and power coefficients are estimated as well. Figure 9.24 and Figure 9.25 show the estimated errors for C_T and C_P at $J = 0.7$. A second order curve is fitted to estimate the errors compared to infinite stations. For the thrust coefficient, the error of the used 25 stations is estimated to be approximately -0.073%. For the power coefficient this error is estimated to be -0.044%. These errors are small, and it is therefore concluded that using 25 stations yields satisfactory results.

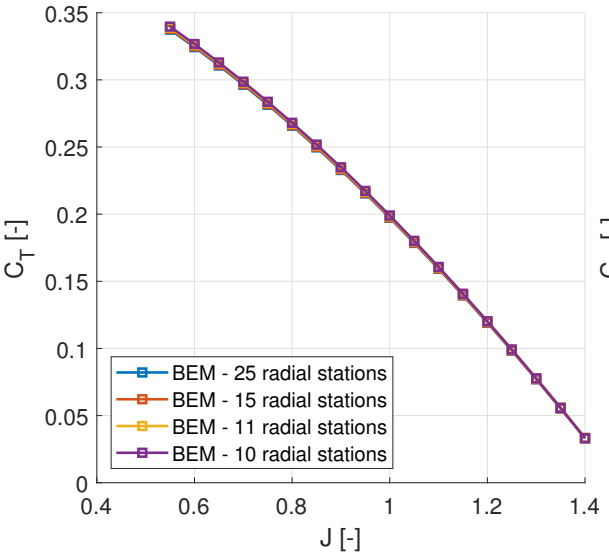

Figure 9.22: Thrust coefficient for a varying number of radial stations

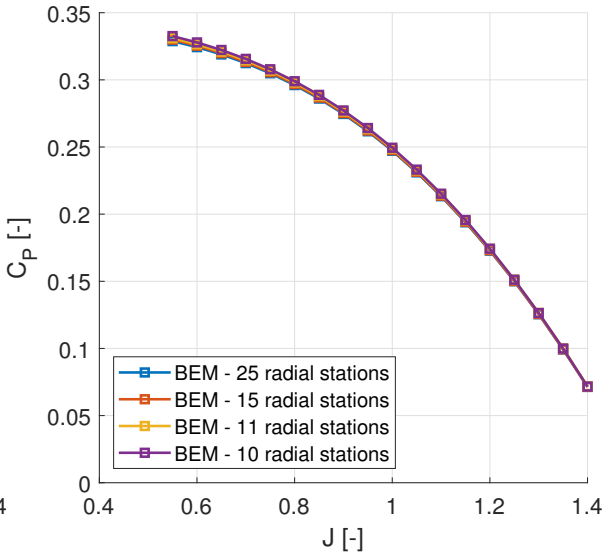

Figure 9.23: Power coefficient for a varying number of radial stations

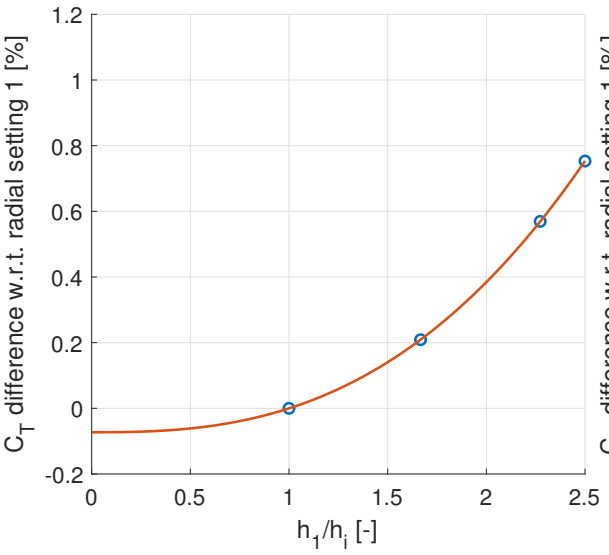

Figure 9.24: BEM radial station thrust coefficient difference w.r.t. radial setting 1 at $J = 0.7$

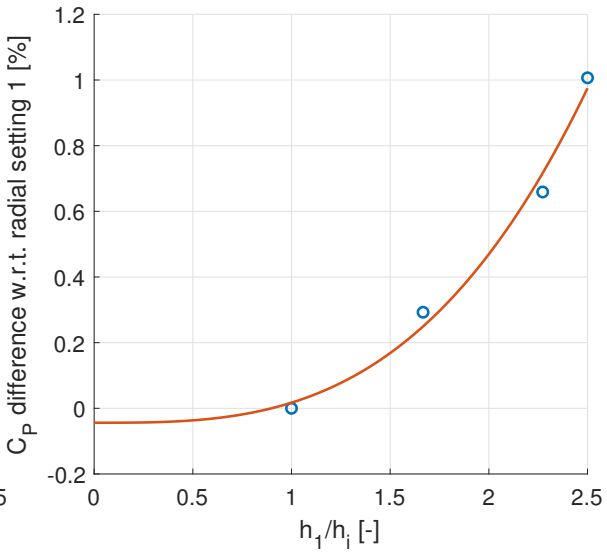

Figure 9.25: BEM radial station power coefficient difference w.r.t. radial setting 1 at $J = 0.7$

9.3. BEM & RANS Validation

This section covers validation by means of a comparison of BEM and CFD results with experimental data. The available experimental data is from the XPROP propelller at a wind tunnel inlet velocity of 30 m/s. The XPROP propeller has 6 blades and has a diameter of 0.4064 m. The XPROP blade is visually presented in Figure 9.26.

Figure 9.26: Visualisation of the XRPOP propeller used in the validation of the BEM and RANS tools

The available experimental data consisted of three runs at which the advance ratio was altered in small steps. The flow conditions of all runs have been averaged for the BEM and CFD analysis, and can be found in Table 9.7.

Table 9.7: Mean Flow Conditions Validation Data

Flow Condition	**Value**	**Unit**
V_∞	30	[m/s]
ρ	1.1747	[kg/m^3]
p_∞	101459	[Pa]
T_s	300.8813	[K]

Although the flow conditions have been averaged, the three experimental runs are shown separately on the validation figures. A low order fit has been made through the experimental data points for visualisation purposes only. The differences between the experimental data and BEM analysis on the thrust coefficient, power coefficient and efficiency are shown in Figure 9.27, Figure 9.28 and Figure 9.29 respectively.

Looking at Figure 9.27 and Figure 9.28, the BEM analysis consistently over predicts the C_t and C_P compared to the experimental data. The error in thrust coefficient is smallest at low advance ratio, and increases with an increase in advance ratio. For the C_P, the smallest error to the test data is obtained around an advance ratio of 1.1. The further the advance ratio deviates from 1.1, the larger the discrepancy between the experimental data and BEM analysis becomes.

Contrary to the results from the BEM analysis, the RANS analysis underestimates the thrust coefficient for most advance ratio settings. The thrust coefficient is reasonably well captured, but the RANS curve shape shows a more linear relation with the advance ratio, while the experimental data shows a more curved drop as the advance ratio increases. This behaviour is similar to the BEM curve. The thrust coefficient is slightly overestimated from an advance ratio of 1.1 upward, and underestimated below 1.1. Regarding the C_P, the RANS data shows again a more linear relation to the advance ratio than the experimental data. Similar to the BEM analysis, RANS underestimates the power coefficient for the largest part. Only from an advance ratio upwards of 1.25, the simulated curve intersects the experimental curve and overestimates it slightly. The BEM and RANS curve for the power coefficient start to deviate more as the advance ratio increases. The deviation in thrust coefficient between BEM and RANS seems constant and more or less independent of the advance ratio. The zero thrust condition is reached much later for both the BEM and RANS calculations.

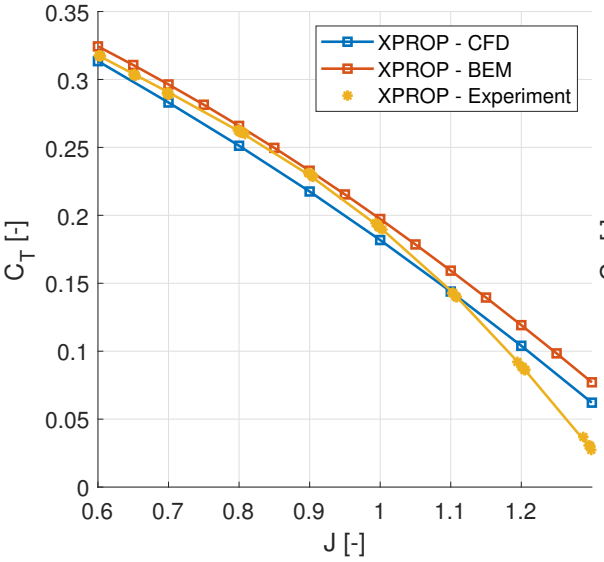

Figure 9.27: Ct Comparison BEM and Experimental Data

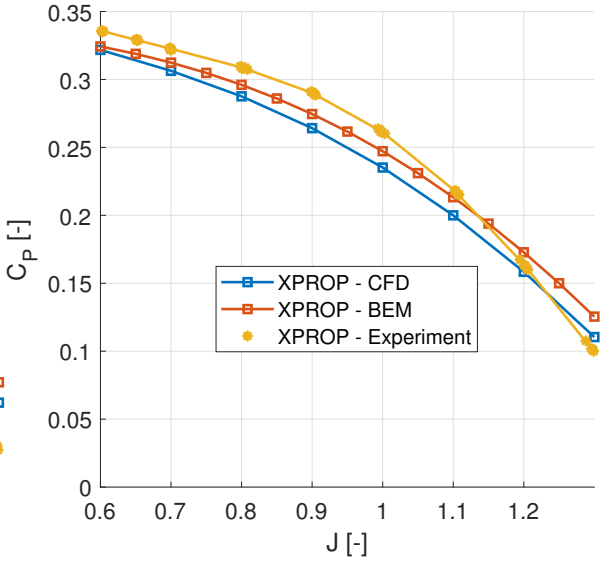

Figure 9.28: CP Comparison BEM and Experimental Data

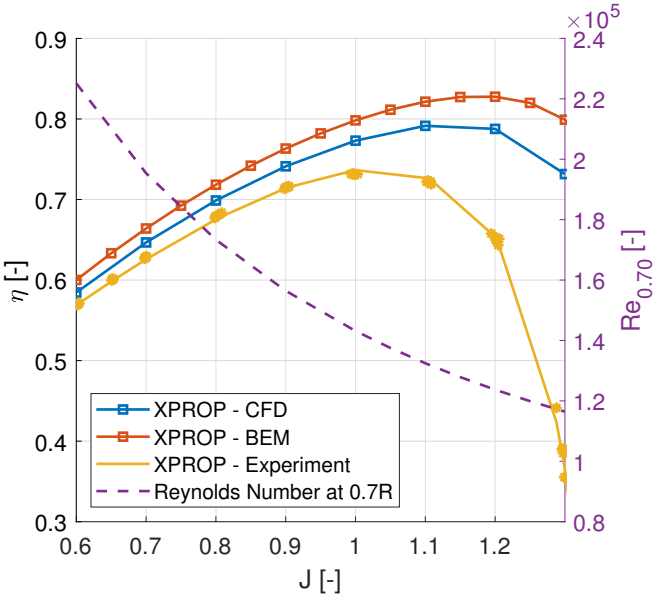

Figure 9.29: Efficiency Comparison Between BEM and Experimental Data

The observations from Figure 9.27 and Figure 9.28 result in expected discrepancies in efficiency, shown in Figure 9.29. At advance ratios lower than 0.9, the experimental data and BEM analysis show reasonable agreement in the slope of the curve. At higher advance ratios, however, the discrepancy becomes larger. The BEM analysis over predicts both the efficiency and the advance ratio at which the maximum efficiency is obtained. The BEM analysis suggests a maximum efficiency of approximately 0.83 at an advance ratio of 1.2, whereas the the experimental data shows a maximum efficiency of approximately 0.74 at an advance ratio of 1.

The RANS analysis overestimates the efficiency at the complete advance ratio range as well. The discrepancy between the simulated data and experimental data does decrease with a decreasing advance ratio. It should be noted though, that with the computed maximum at $J = 1.1$, the efficiency curve of RANS shows better agreement with the experimental data than the BEM analysis. The magnitude of the RANS curve shows also a closer resemblance with the experimental data than the BEM analysis.

The curves presented in this section indicate that the effective blade pitch angle differs between the computed blades and the experimental data. This may be due to a shift in the zero lift angle of attack of the blade profiles caused by low Reynolds numbers at high advance ratios. From the right hand y-axis in Figure 9.29 it can be seen that the Reynolds number drops below $1.5 \cdot 10^5$ at advance ratios greater than 0.95. Reynolds number sensitivity below $1.5 \cdot 10^5$ results in deviations which are difficult to predict. For Reynolds numbers higher than $1.5 \cdot 10^5$, the performance sensitivity to the Reynolds number becomes smaller [45]. In an attempt to reduce the discrepancies caused by low Reynolds numbers, the ambient velocity is increased to 60 m/s compared to the 30 m/s of the experimental data for computations in the remainder of this study.

Although the RANS and BEM results do not show perfect agreement with each other and the experimental data, the results are deemed satisfactory for this research. By increasing the flight velocity, the Reynolds number is increased which is expected to slightly decrease the error compared to wind tunnel data. In this research, the goal is to find trends between sweep, efficiency and noise. As all propellers are compared relatively to each other, the study can be carried out with the proposed analysis methods. For future research, when propellers are designed with real-life applications in mind, possibly more computational expensive methods should be used.

9.4. Noise Verification

In this section, the noise results are verified. First, the shapes of the noise sources are qualitatively compared to reference shapes from literature. This allows to visually check if the computed sources are of the correct type. Secondly, the noise results from both BEM and CFD computations are compared. As no experimental or reference data is available, validation is not performed. However, when the results from the comparisons show satisfactory agreement, this is deemed sufficient for the relative comparisons done in this study. As the equations used are valid for far-field noise only, all noise computations are done at a distance of at least 20 times the propeller diameter. The noise source shapes are computed at a constant radius from the propeller, while the total noise is computed along a line located at a distance of 20 times the propeller diameter parallel to the propeller direction. In the third subsection, the sensitivity of the total noise solution to the number of harmonics is investigated. The last subsection elaborates on the dependency of the noise results to the number of radial stations.

9.4.1. Qualitative Noise Source Verification

The first step in verifying the noise computations is checking the shape of each separate noise source. By visually inspecting the shapes of the noise sources, it can be ensured that the resulting sources are the correct source type. The general noise source shapes are obtained from literature [46], and are shown in Figure 9.30, Figure 9.31 and Figure 9.32. From these figures, it can be seen that the thickness and tangential force sources should be shaped as a dipoles, while the thrust source should be a quadrupole.

For this verification, an evaluation from the XPROP propeller, visualised in Figure 9.49, is used at a velocity of 60/ms and an advance ratio of 0.85. The resulting source shapes are shown in Figure 9.33, Figure 9.34 and Figure 9.35. Comparing the computed shapes with the reference figures, it is clear that the computed sources are of the correct type. The thrust source shape is pointing in a less distinct diagonal direction compared to the shape from literature. This distinct shape could depend on the magnitude of the thrust. Near 90 and 270 degrees the curve is less smooth, this is due to the discretisation of the angles, as the source is computed in steps of 1 degree.

All computed noise sources and the total noise are plotted together in Figure 9.36 and Figure 9.37 for an

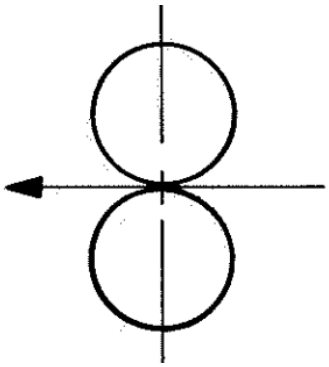

Figure 9.30: General thickness dipole shape [46]

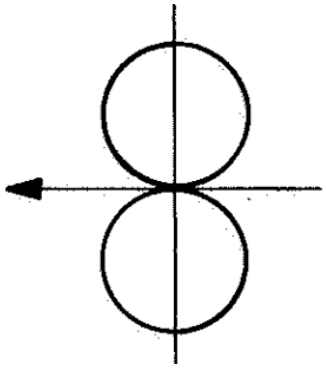

Figure 9.31: General tangential dipole shape [46]

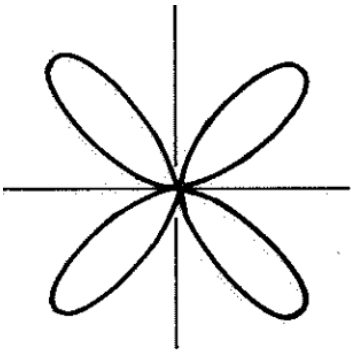

Figure 9.32: General thrust quadrupole shape [46]

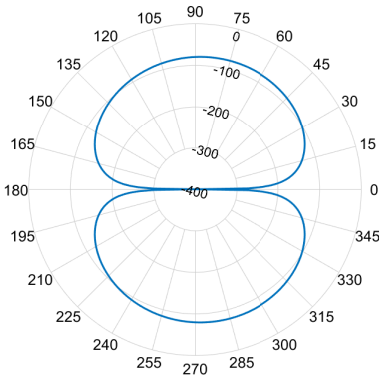

Figure 9.33: Computed thickness source shape for the XPROP at J = 0.85

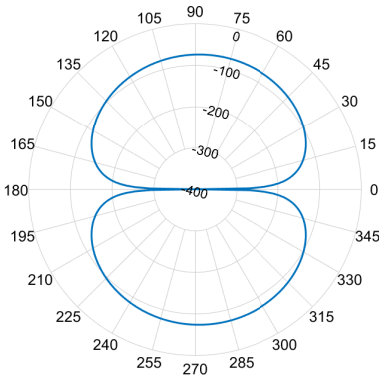

Figure 9.34: Computed tangential source shape for the XPROP at J = 0.85

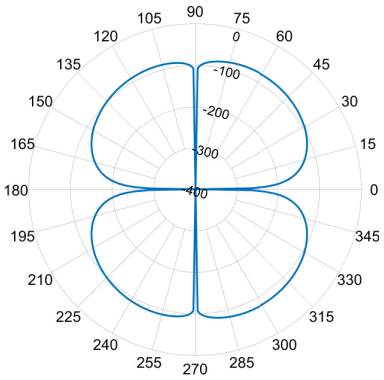

Figure 9.35: Computed thrust source shape for the XPROP at J = 0.85

advance ratio of 0.85 and 1.30 respectively. Interference between the noise sources is visible in Figure 9.36, where the individual tangential source component on the left side is larger than the total noise pattern. The thickness and tangential source components appear dominant, where the thickness source gets notably more dominant at Figure 9.37 where the thrust is smaller due to the higher advance ratio.

9.4.2. TSSP Comparison of RANS and BEM Results

In this subsection, the three random designs that were introduced first in chapter 3 for BEM verification are used again to evaluate the differences in noise between BEM and CFD. The TSSP computed from the BEM and CFD results is plotted against the advance ratio and thrust coefficient in Figure 9.38 and Figure 9.39 respectively. The thrust coefficient is chosen to be plotted against the TSSP since verification showed that the BEM and CFD evaluations have different J - C_T curves.

Interesting to see is that for all the designs, the BEM and CFD results show a similar performance of the propeller in terms of TSSP vs J. The large discrepancy for design 2 in thrust coefficient, shown in Figure 9.12, is only minimally visible when comparing the TSSP vs advance ratio. Both the total, or integrated, loading value of the blade and the loading distribution impact the computed TSSP values. When comparing the TSSP against the advance ratio, the blades are compared at the same geometrical tip Mach numbers. The effect of the dominant thickness source as seen in subsection 9.4.1 appears in Figure 9.38 as well, as the the differences are between the BEM and CFD simulations are small. Only design 2, which has large discrepancies in the loading distributions and integrated loading values shows larger differences between the BEM and RANS results.

Differences between BEM and CFD results are more apparent when looking at the TSSP vs C_T. The general trend difference between the BEM and CFD results for design 1 and 3 can be explained by looking back at the C_T vs J results in Figure 9.12. Since the BEM analysis of design 3 over predicts the C_T compared to the CFD analysis, the BEM analysis matches the C_T of the CFD results at a higher advance ratio, and thus lower tip velocities. Lower tip velocities reduce the noise, and therefore the BEM analysis of design 3 is generally lower

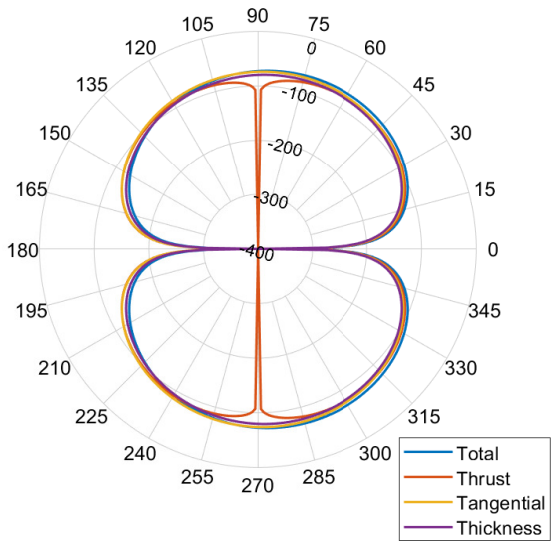

Figure 9.36: Combined noise directivity at J = 0.85

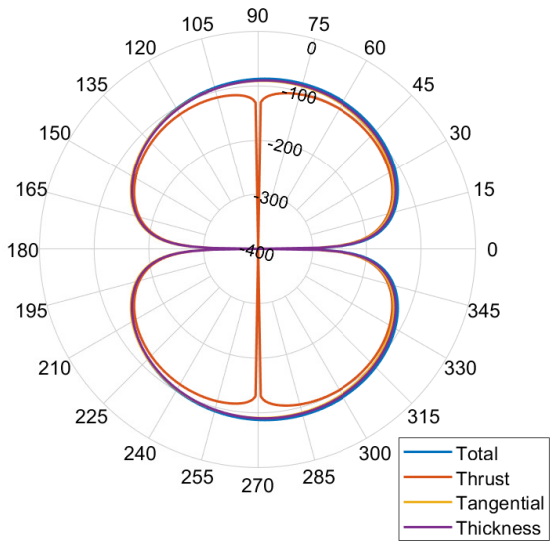

Figure 9.37: Combined noise directivity at J = 1.3

than the CFD curve. The reverse is visible for design 1. The BEM and CFD offset of TSSP for design 1 and 3 is not constant. Differences in loading distributions can contribute to this. Interesting to see is that, looking at the CFD results, design 3 appears to be the best performing propeller in terms of TSSP, whereas design 2 is on-par at lower thrust coefficients, but degrades in performance at higher thrust coefficients. Design 1 performs worse than the other designs, up until a C_T of approximately 0.17, after which design 2 is the worst performing propeller.

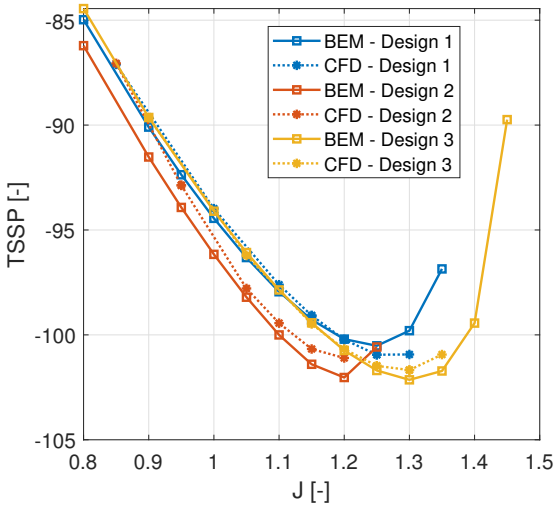

Figure 9.38: TSSP vs J for BEM and RANS for the random designs generated in chapter 3

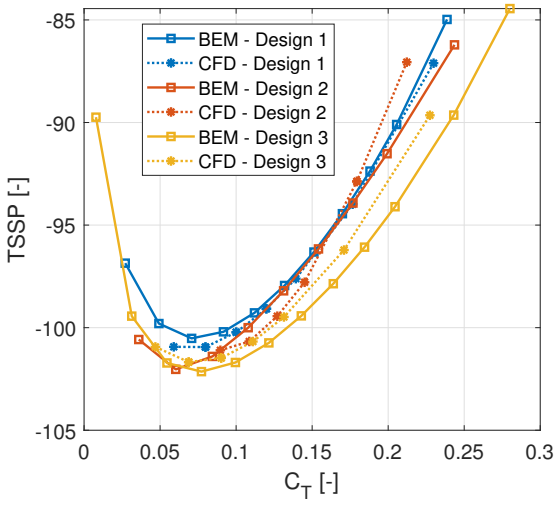

Figure 9.39: TSSP vs C_T for BEM and RANS for the random designs generated in chapter 3

9.4.3. Sensitivity to Number of Harmonics

This section discusses the sensitivity of the TSSP to the number of harmonics. For this verification, the TSSP of the XPROP has been computed using only the first harmonic, the first two harmonics and the first three harmonics. To keep the computational cost low, ideally as few harmonics as possible are computed. The results are shown in Figure 9.40. As is clear from the figure, the first harmonic is very much dominant, and the addition of extra harmonics does not alter the computed TSSP much. The individual TSSP contributions of each harmonic are computed as well at two different advance ratios. In Figure 9.41, the TSSP contribution of

each consecutive harmonic is reduced by 20 dB at an advance ratio of 0.85. At an advance ratio of 1.4, shown in Figure 9.42, the contribution of each consecutive harmonic is even smaller with a reduction of almost 40 dB for each step.

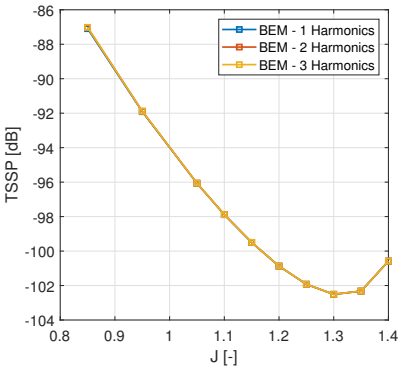

Figure 9.40: TSSP at varying number of harmonics for the XPROP

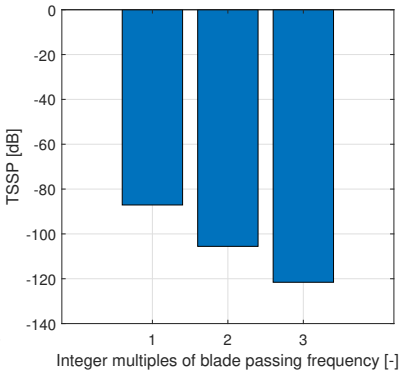

Figure 9.41: TSSP from separate harmonics for the XPROP at $J = 0.85$

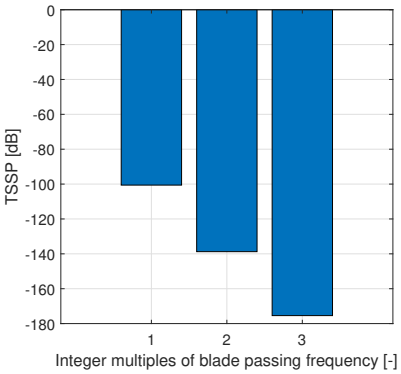

Figure 9.42: TSSP from separate harmonics for the XPROP at $J = 1.4$

Table 9.8 shows the mean difference in TSSP between each subsequent addition of harmonics. The mean TSSP difference between using the first three harmonics and the first 2 harmonics is less than $3 \cdot 10^{-4}$, which is deemed small enough to be neglected. In the remainder of this study, the TSSP is computed with only the first two harmonics.

Table 9.8: TSSP differences w.r.t. the previous step

	Harmonic 1	**Harmonics 1-2**	**Harmonics 1-3**
Mean TSSP [dB]	-98.07	-98.06	-98.06
Δ TSSP [dB]	0	$1.24 \cdot 10^{-2}$	$2.39 \cdot 10^{-4}$

9.4.4. Noise Dependency to Number of Radial Stations

In this subsection the dependency to the number of radial stations is investigated. Since the phase delay due to the addition of sweep to each radial station impacts the computed TSSP, the TSSP can be sensitive to the radial discretisation. For this verification step, the 3 swept blade designs introduced first in the BEM verification are used again. Since the implementation for the CFD result extraction allows for an arbitrary chosen radial discretisation, the dependency study is performed using CFD results. The radial CFD discretisation is set at 50, while the radial BEM discretisation is set at 25. The various radial station settings are presented in Table 9.9.

Table 9.9: Radial Stations used in Noise Dependency Study

Radial Station Setting	**Number of Radial Stations**	h_1/h_i
1	50	1.00
2	25	2.00
3	15	3.33
4	11	4.54

The TSSP results at the various radial settings for designs 1, 2 and 3 are presented in Figure 9.43, Figure 9.44 and Figure 9.45 respectively. In all figures, the spread between the largest number of radial stations and least number of radial stations is less than 1.5 dB. Design 1 and 3 show a consistent trend in the order of TSSP magnitude of each radial setting, in which a finer discretisation slightly increases the computed noise compared to a coarser discretisation. This is different for design 2, which does show a similar trend at the lowest advance ratio, but reverses this order at higher advance ratios.

The relative TSSP differences of each radial station setting relative to 50 radial stations for the three designs are presented in Figure 9.46, Figure 9.47 and Figure 9.48. The differences are presented at the lowest evaluated advance ratio for each design. A second order curve has been fitted through the points to extrapolate to a case

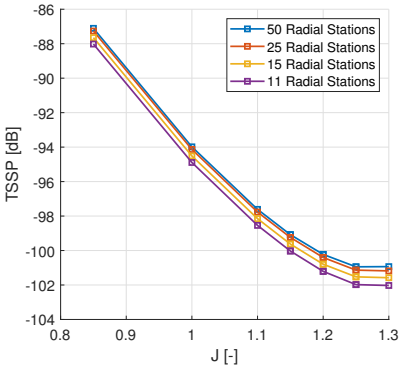

Figure 9.43: TSSP of design 1 computed at a varying number of radial stations

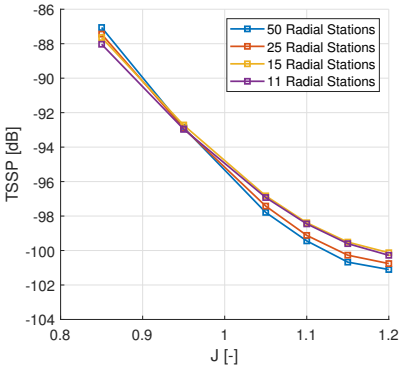

Figure 9.44: TSSP of design 2 computed at a varying number of radial stations

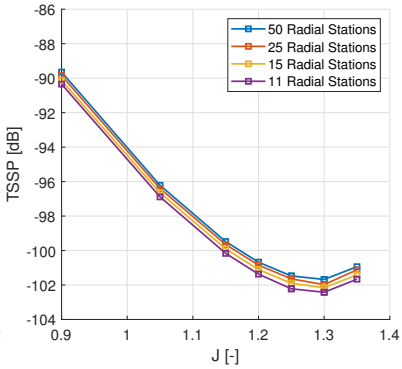

Figure 9.45: TSSP of design 3 computed at a varying number of radial stations

with infinite radial stations. Taking the bounds of the three designs leads to concluding that using 50 radial stations results in a discretisation error between 0.1% and 0.5%. It should be noted that Figure 9.44 suggests that these estimated discretisation errors can differ per advance ratio for a given design.

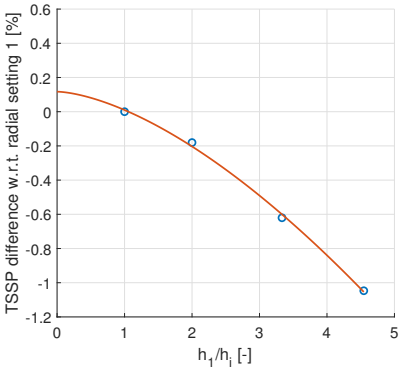

Figure 9.46: Relative TSSP differences for design 1 at a varying number of radial stations at $J = 0.85$

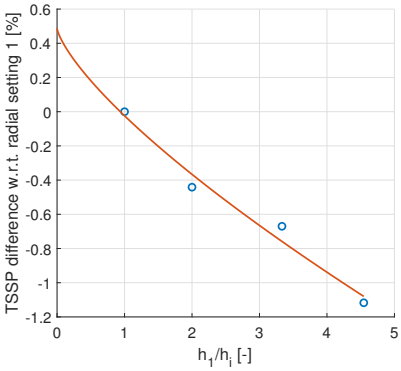

Figure 9.47: Relative TSSP differences for design 2 at a varying number of radial stations at $J = 0.85$

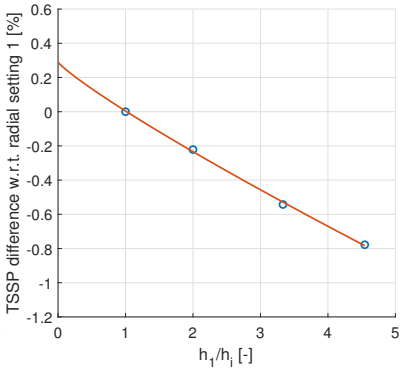

Figure 9.48: Relative TSSP differences for design 3 at a varying number of radial stations at $J = 0.9$

9.5. Parametrisation Error Estimation

In this section, the parametrised XPROP is compared to the original geometry. This is done to get more insight in how well the parametrisation can approximate existing propeller blades. For the XPROP, the Bezier curves are fitted to match the original geometrical distributions. This fitting is not required when randomly generating blades. The geometrical differences are discussed first in subsection 9.5.1, followed by an investigation into any discrepancy in results for the parametrised XPROP and the original blade in subsection 9.5.2.

The original XPROP blade is presented in Figure 9.49, and is created from 25 radial stations. Regarding the parametrisation of the distributions, the number of control points have been minimised while maintaining the ability to capture the general shape and distinct features of the original distributions. The following number of control points are used:

- Twist distribution: 3 control points;
- Chord distribution: 4 control points;
- Sweep distribution: 3 control points.

A last remark is that the spinner of the original XPROP had a curved fairing behind the propeller blade as the nacelle had a smaller diameter than the spinner. This fairing is used in the RANS validation cases, but for the parametrised blades the nacelle diameter has been increased such that no curved fairing is required. The curved fairing and straight fairing are shown in Figure 9.50 and Figure 9.51 respectively.

Figure 9.49: XRPOP Propeller

Figure 9.50: XPROP propeller with (small) curved fairing aft of the spinner

Figure 9.51: XPROP propeller with straight fairing aft of the spinner

9.5.1. Geometrical Parametrisation Errors

The Bezier curves for the XPROP blade are fitted in an optimisation scheme. The built-in non-linear least squares solver from MATLAB was used. During the optimisation routine, the error is computed by taking the difference between the resulting Bezier curve and the known cross-sectional data from the XPROP. The design parameters that are fitted are the twist and chord distribution. The mid-chord sweep for the XPROP is non-zero, but very small. It is therefore not included in this distribution parametrisation error estimation. The geometrical twist and pitch errors are provided next. Note that as the first airfoil section does not start at zero propeller radius, the distributions do not start at zero radius either.

Figure 9.52 shows the original and parametrised twist distribution along the normalised blade radius. Inspection of the curves show that they are very good in agreement. The difference in twist is presented in Figure 9.53. The error oscillates around the zero error line. The maximum absolute error is approximately 0.34 degrees, whether this is negligible and does not alter the results is investigated in subsection 9.5.2.

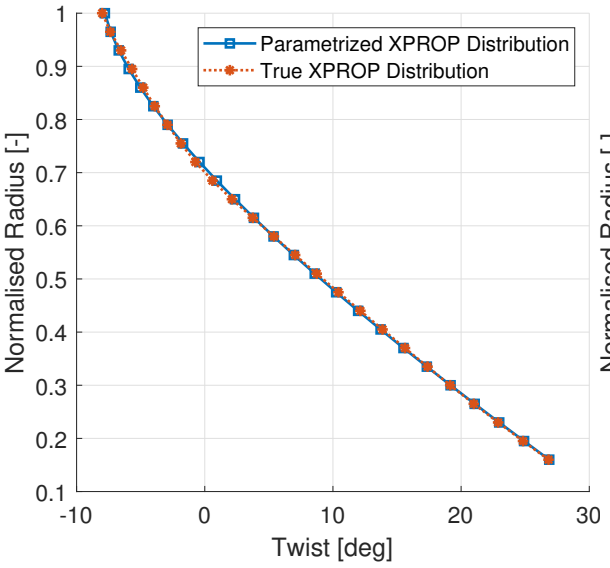

Figure 9.52: Parametrised and original twist distribution of the XPROP

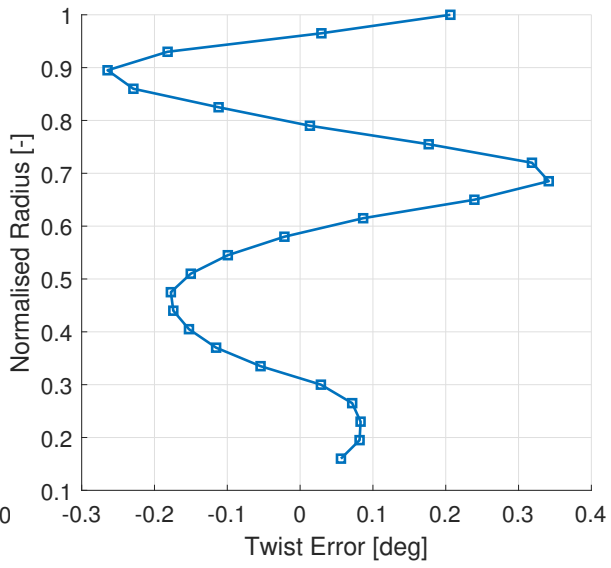

Figure 9.53: Parametrised and original twist distribution difference of the XPROP

The parametrised and non-parametrised chord distributions are shown in Figure 9.54. The normalised chord length is obtained by dividing the chord length by the propeller radius. Similar to the parametrisation of the twist, the two chord distribution show very good agreement. The difference between the two curves oscillates around the zero error line, as shown in Figure 9.55. The maximum absolute chord difference is approximately 0.2 mm, or approximately $1 \cdot 10^{-3}$ for the normalised chord error.

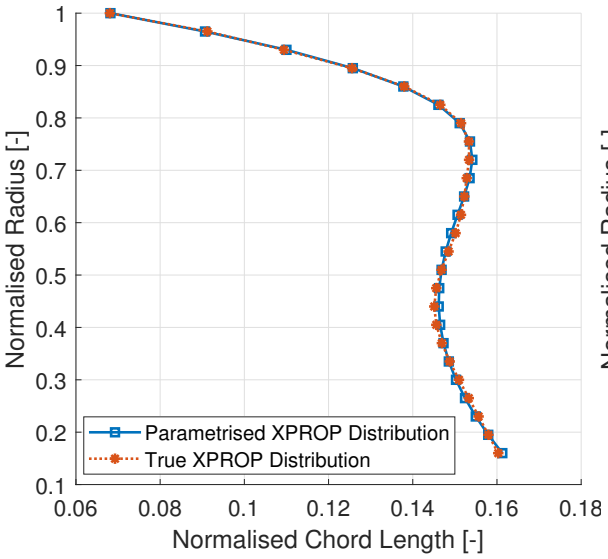

Figure 9.54: Parametrised and original chord distribution of the XPROP

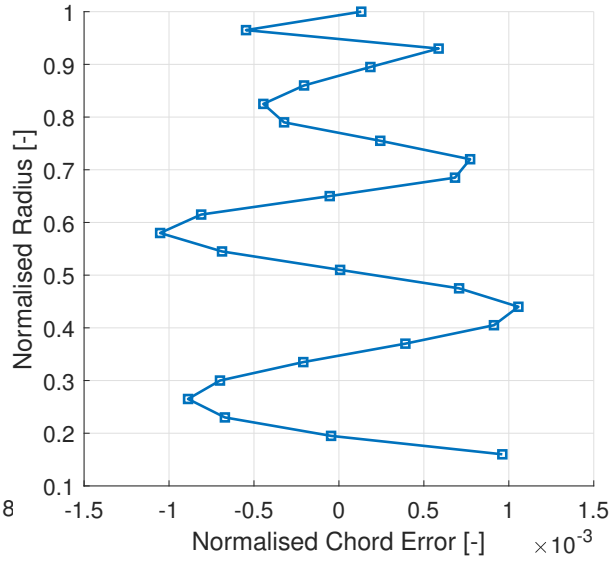

Figure 9.55: Parametrised and original chord distribution difference of the XPROP

9.5.2. Parametrised XPROP Verification

In this subsection, the BEM and CFD results are compared for the parametrised and non-parametrised XPROP blades. The geometrical differences between the parametrised XPROP and the non-parametrised XPROP proved to be very small. The computed results presented in Figure 9.56 and Figure 9.57 show that the geometrical errors are negligible to the computed thrust and power coefficient. For both RANS and BEM computations, the parametrized and non-parametrized curves show excellent agreement. Notable is that the curved fairing extension after spinner that is present with the non-parametrised RANS simulation does not appear to influence the results in a much different way than the straight spinner-nacelle fairing.

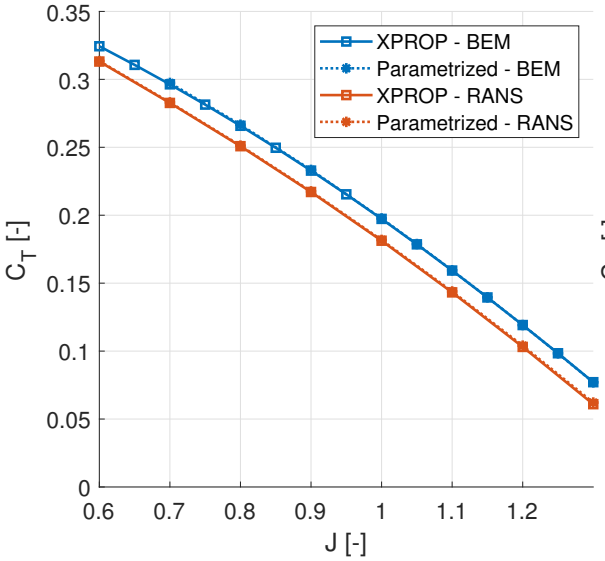

Figure 9.56: Ct Comparison CFD and Experimental Data

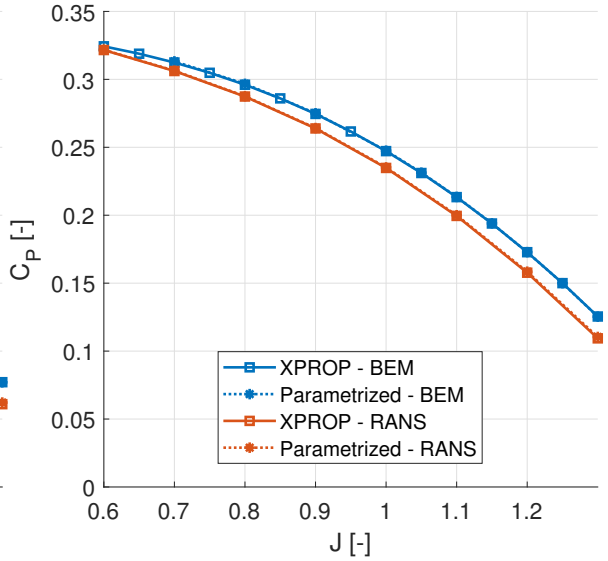

Figure 9.57: CP Comparison CFD and Experimental Data

In agreement with the thrust and power coefficient results, no large discrepancies arise between the parametrised and non-parametrised blades in terms of efficiency. This is shown in Figure 9.58. Regarding the RANS evaluations, a small discrepancy is visible at high advance ratios. The BEM evaluations show near perfect agreement. It is shown that the parametrisation can approximate existing blades well, without large discrepancies in the results. This gives confidence in that the randomly generated blades can approximate feasible designs for real life propellers, at least when neglecting possible structural constraints.

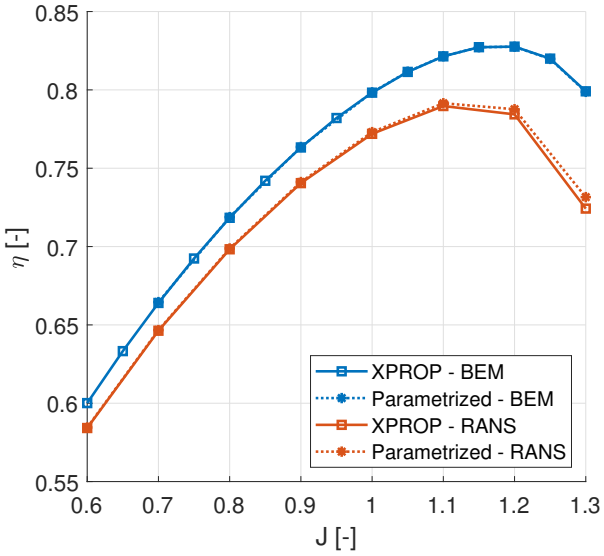

Figure 9.58: XRPOP Propeller

10

Aerodynamic and Aeroacoustic Results

The numerical results are presented and discussed in this chapter. Initially, the boundaries and constraints and operating conditions are discussed in section 10.1. The accuracy of the kriging model is then evaluated in section 10.2. In section 10.3 the results are presented. Here, both the dependency between efficiency and TSSP is investigated, as well as the effect of sweep, pitch angle and advance ratio on the efficiency and TSSP. In the last section, section 10.4, some individual designs from the kriging results are selected and evaluated by CFD, a Pareto front is illustrated and the final conclusions on the numerical results are made.

10.1. Evaluation Set-Up

In this section, first the boundaries and constraints are discussed, followed by a description of the operating conditions on which the blades are evaluated.

10.1.1. Boundaries and Constraints

All blade design and operational parameters have been discussed in chapter 6. In this study, however, not all parameters are investigated. Due to constraints on time and computational resources, only the effects of sweep, pitch angle and advance ratio are investigated. For the sweep a total of 3 control points are used, each with an x and y component. As the first and last control point are fixed such that the distribution spans along the complete radius, and the root is fixed to zero sweep, the number of design variables for sweep comes down to only 3. Along with the advance ratio and collective pitch, the number of design variables is 5 in total.

Although the sweep design variables control the sweep translation directly, the boundaries are based on the translation of the maximum tip sweep. Since the computational domain of the RANS simulations is in a pie shape, care should be taken that parts of the blade do not get too close to the walls. As the number of blades is fixed to six, the domain is shaped as a 60 degree wedge. The boundary for the sweep has therefore been determined such that the tip angle cannot be larger than 20 degrees, and smaller than -20 degrees measured from the root. The maximum translation of the 20 degree tip angle is the constraint used for the sweep translation of the whole blade. Since the distribution is smooth and starts at zero at the root, the constraint ensures that the blade leaves enough room to the walls. The 60 degree wedge shaped domain is slightly rotated such that the blade is centred as much as possible in the domain. Structural limits should be taken into account in future studies to set up more realistic bounds.

The pitch angle is varied between 25 and 60 degrees. Trial and error showed that the performance could be resolved well within these limits. In future studies, possibly more reference data can be used to determine these limits.

10.1.2. Operating Conditions

The ambient conditions at which the results are evaluated are set at sea level conditions in accordance to the international standard atmosphere. These conditions are shown in Table 10.1.

Regarding the constant thrust at which all blades are compared, use is made of the specifications of a reference aircraft to ensure that the set thrust is realistic. The ATR72-500 propeller aircraft is selected as reference, of which the properties are shown in table Table 10.2. Using the known reference properties, the T_C is computed according to Equation 10.1.

Table 10.1: Ambient conditions kriging evaluations

Property	Value	Unit
V	60	m/s
Altitude	0	m
ρ	1.225	kg/m^3
T_s	288.15	K

Table 10.2: ATR72-500 properties [1]

Property	Value	Unit
V	510	km/h
Max. landing mass	21850	kg
D	3.93	m
ρ	0.5489	kg/m^3
Cruise altitude	7620	m

$$T_C = \frac{T}{\rho \cdot V^2 \cdot D^2} \tag{10.1}$$

To compute the thrust coefficient, it is assumed that thrust equals drag, and lift equals weight. Also, the L/D ratio is assumed to be 17. Combining the assumptions and reference properties results in a computed thrust coefficient for the ATR72-500 of approximately 0.0741. Since the ATR72-500 consists of two propellers, this value is halved to obtain the thrust coefficient per propeller. This gives a T_C of approximately 0.0371. Reversing the computation and inserting sea level ambient conditions and a propeller diameter of 0.4064 m results in a thrust of approximately 27N. This thrust is used in the remainder of the results chapter to compare the performance of various blade designs. The blade designs are trimmed by adjusting either the collective pitch angle or both the pitch angle and advance ratio. These cases are discussed in section 10.3.

10.2. Surrogate Model Accuracy

Before the results are discussed, the accuracy of the kriging model is estimated. In total, 1000 propeller designs have been evaluated at various advance ratios and collective pitch angles. To ensure the model could capture the effect of the collective pitch, several propeller designs have been evaluated multiple times for an advance ratio range at different pitch settings. In total, 4324 RANS data points and 25116 BEM data points have been generated for the 1000 propellers. Of these 1000 propellers, 993 have been evaluated successfully.

To validate the accuracy of the model, 8 propellers of which no RANS data was provided during training are evaluated and compared to the actual RANS data. These 8 propellers are evaluated over a range of feasible advance ratios at a random pitch angle. Training of each model takes approximately 2 hours, so combined a total of 6 hours are required to get all three models. Limitations of the available computational resources were approached as training and using the models can take up to 60GB of RAM. The 8 validation propeller designs are visualised in Figure 10.1 to Figure 10.8.

The results presented in this section are obtained after one additional iteration of generating extra data points is performed. The goal of this iteration was to reduce the outliers or extreme points found by the kriging model. Overviews of the errors of both the initial model and iterated model are given in Table 10.3 and Table 10.4 respectively. The errors per design for both cases are provided in Appendix B as well as visualisations for the errors of the initial model. A comparison in results between the two models is given in section 10.3.

As far as the thrust coefficient prediction is concerned, the kriging model performs very well. Visible in Figure 10.9, the largest errors are found for validation design 5 and 7 at the lower limit of their respective advance ratio ranges. The average absolute error of the C_T is in the order of $2.2 \cdot 10^{-3}$, which is deemed small by the author of this study.

Design 2, 5 and 7 show the largest errors in regards of the efficiency, Figure 10.10, and the TSSP, Figure 10.11. The largest error for design 5 appears at the lowest advance ratio for both the efficiency and TSSP,

[1] Source: https://modernairliners.com/atr72andatr42/, accessed on 12-08-2020

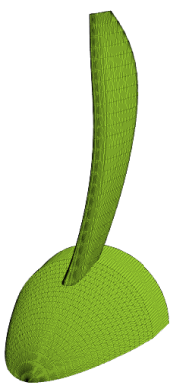

Figure 10.1: Kriging validation propeller design 1

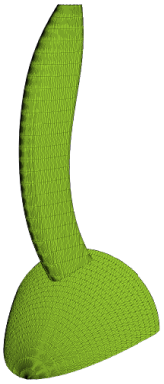

Figure 10.2: Kriging validation propeller design 2

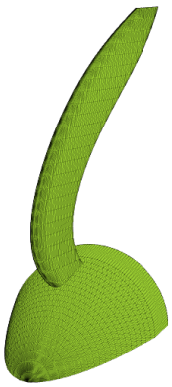

Figure 10.3: Kriging validation propeller design 3

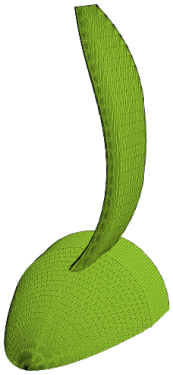

Figure 10.4: Kriging validation propeller design 4

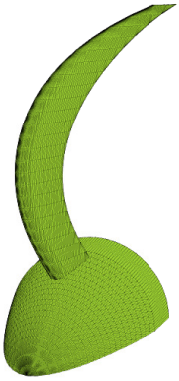

Figure 10.5: Kriging validation propeller design 5

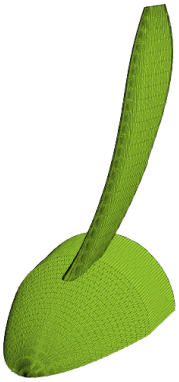

Figure 10.6: Kriging validation propeller design 6

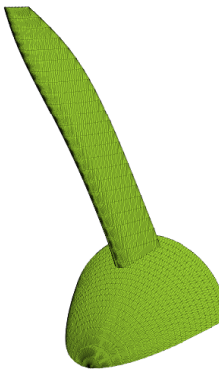

Figure 10.7: Kriging validation propeller design 7

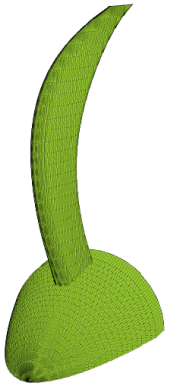

Figure 10.8: Kriging validation propeller design 8

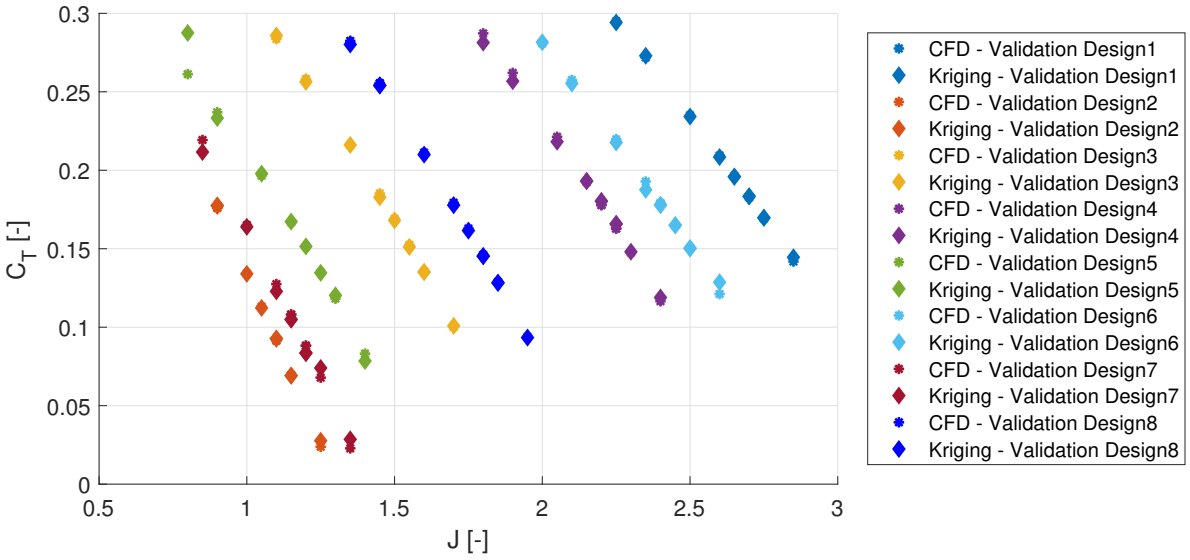

Figure 10.9: Thrust coefficient comparison between Kriging and RANS

while the largest errors for design 2 and 7 appear at the highest advance ratio. Still, the mean errors are sufficiently small to show reasonable similarity between the kriging and CFD results. Looking at the the visual representation of design 5 and 7 in Figure 10.5 and Figure 10.7 makes clear that both designs have the most extreme sweep of the validation blades. The higher the sweep, the more difficult it becomes for the model to predict correct results. This may partially be caused by the problems the BEM analysis appears to have with high sweep and high out of plane blade translation as discussed in section 9.2. Despite of these points, the validation shows satisfactory results of the surrogate model. Design 4 overestimates the TSSP for most part of the computed advance ratio range with an absolute average error of 2 dB. This can indicate that more CFD data points are required.

The validation of the BEM and CFD methods in section 9.3 showed that the CFD method drops in efficiency a little sooner than the BEM method when the advance ratio is increased, this could cause the difference seen between the kriging model and CFD points at the high advance ratios for designs 2 and 7 in Figure 10.10. Since much more BEM data points are provided to the kriging model, its results may sometimes be biased towards the BEM results. However, the results from the BEM verification in section 9.2 show that the efficiency of the CFD results does not always drop sooner than the BEM results. This hypothesis cannot be confirmed.

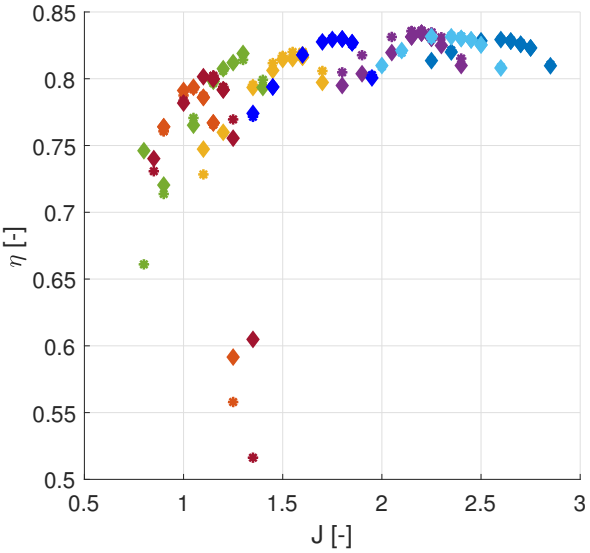

Figure 10.10: Efficiency comparison between Kriging and RANS

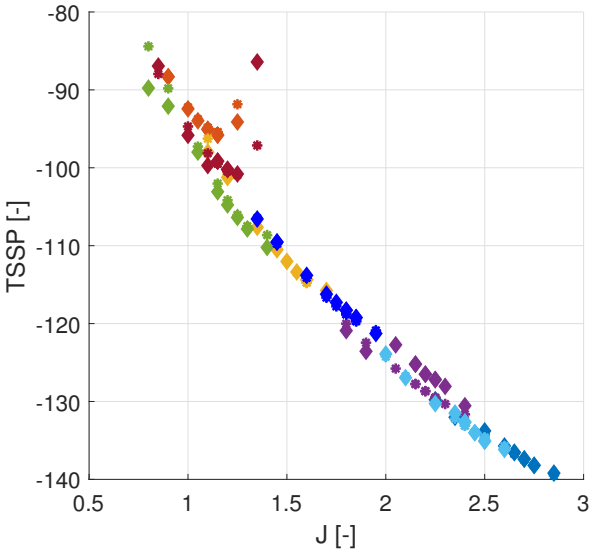

Figure 10.11: TSSP comparison between Kriging and RANS

Table 10.3: Absolute kriging errors for C_T, η and $TSSP$ for the initial kriging model

Property	Min. Error	Max. Error	Mean Error	Standard Deviation
C_T [-]	4.44E-06	2.56E-02	1.46E-03	3.21E-03
η [-]	5.03E-05	8.75E-02	5.58E-03	1.37E-02
$TSSP$ [dB]	5.61E-03	9.40E+00	1.11E+00	1.38E+00

Table 10.4: Absolute kriging errors for C_T, η and $TSSP$ for the kriging model after one additional iteration

Property	Min. Error	Max. Error	Mean Error	Standard Deviation
C_T [-]	8.82E-05	2.63E-02	2.19E-03	3.29E-03
η [-]	4.66E-05	8.86E-02	5.40E-03	1.41E-02
$TSSP$ [dB]	1.32E-02	1.07E+01	8.78E-01	1.45E+00

The additional iteration for extra data points does not show large improvements in the comparison of RANS and kriging data points. Comparing Table 10.3 and Table 10.4 shows that the mean C_T error is slightly increased, while the mean η and $TSSP$ errors are reduced. The differences between outliers in the final results are more visible. These are shown in the next section.

The research sub-question on how well the surrogate model performs compared to RANS evaluations is answered in this section. Based on the validation results, the average absolute kriging errors for C_T, η and TSSP are $2.19 \cdot 10^{-3}$, $5.40 \cdot 10^{-3}$ and $8.78 \cdot 10^{-1}$ respectively. Although not perfect, these are satisfactory results. The kriging model should allow for trends to be detected in relative comparisons between propeller blade designs.

10.3. Kriging Results

After separate models have been trained for the efficiency, thrust coefficient and TSSP, the kriging model can be used to query propeller properties based on design parameters. In theory, the models can be used to explore new designs with sweep parameters on which the models have not been trained. In this study, however, the kriging model is used only to query propeller blade designs which have been used as input of at least one BEM evaluation. The advance ratio and collective pitch however are varied on values which have not necessarily been evaluated at each specific blade design.

For a fair evaluation and comparison between blades, each blade setting has been adjusted such that it operates at a reference T_C of 0.0371 as explained in section 10.1.

For this study, three cases have been evaluated. The collective pitch and advance ratio of each blade have been optimised first such that the maximum efficiency is obtained. Secondly, the collective pitch and advance ratio of each blade have been optimised to obtain minimum noise. Thirdly, the advance ratio is kept constant and only the pitch is varied to obtain the reference thrust. In this last case, the Mach number does not change which eliminates Mach number effects.

This section consists of two parts. First, an overview is given of the results in which the relation between efficiency and TSSP is investigated. The effect of the blade parameters are investigated after that.

10.3.1. General Relation Efficiency and TSSP

Comparing Figure 10.12 with Figure 10.14, and Figure 10.13 with Figure 10.15 shows that the kriging point clouds have become more compact due to the additional iteration. This indicates that less outliers may be present, which makes the results more reliable. The maximum predicted efficiency is reduced from 0.8494 to 0.8441, while regarding the noise the clouds are much more distinct from each other.

The results for the various propeller designs discussed in this study are shown in Figure 10.14 and Figure 10.15 in which lines are sketched roughly following the best design points of each point cloud. The constant advance ratio is based on the average advance ratio of the case for propellers with maximum efficiency, which is $J = 2.1269$.

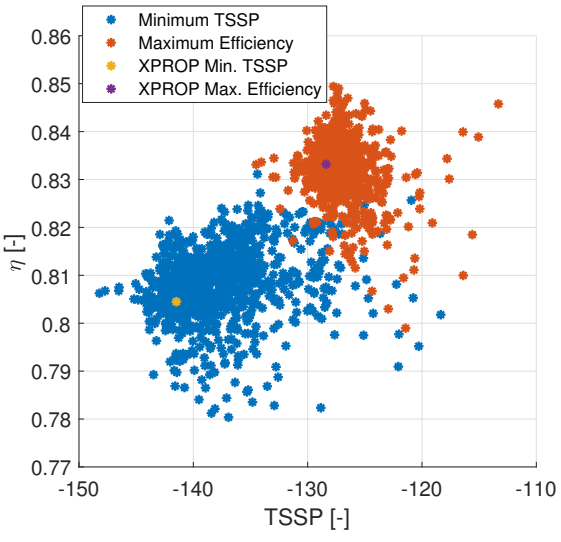

Figure 10.12: TSSP vs Efficiency relation for propeller design points on maximum efficiency and minimum TSSP obtained from the initial kriging model

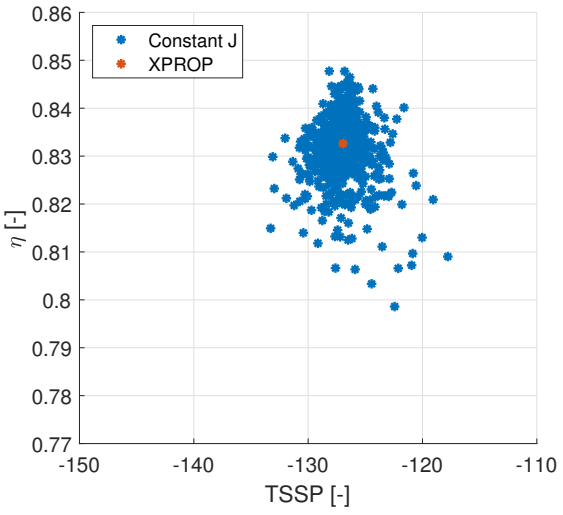

Figure 10.13: TSSP vs Efficiency relation for propeller design points on constant advance ratio obtained from the initial kriging model

The data points for minimum TSSP and maximum efficiency suggest that there clearly is a trade-off between efficiency and TSSP. The highest efficiencies, around 0.844 are obtained when selecting propeller set-

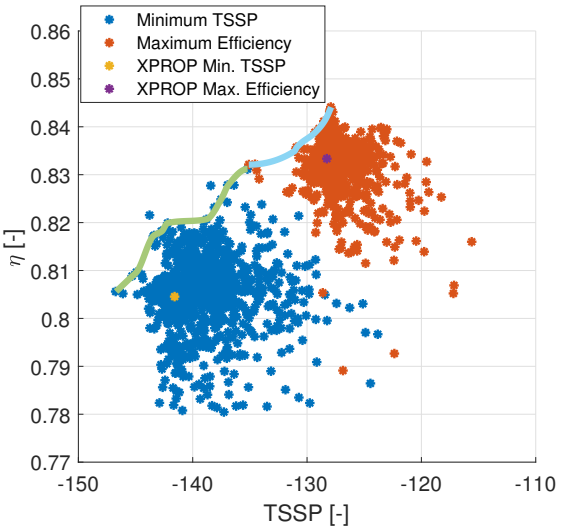

Figure 10.14: TSSP vs Efficiency relation for propeller design points on maximum efficiency and minimum TSSP obtained from the kriging model after an additional iteration

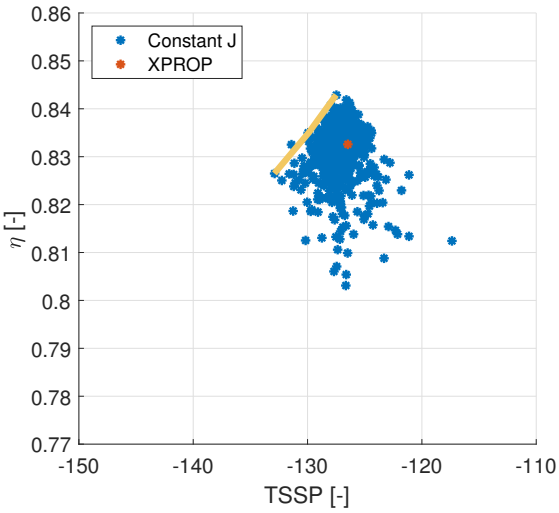

Figure 10.15: TSSP vs Efficiency relation for propeller design points on constant advance ratio obtained from the kriging model after an additional iteration

tings for the highest efficiency. For propellers at the settings of minimum TSSP, the highest efficiency is estimated to be approximately 0.83, although this point is an outlier compared to the other results. The lowest obtained TSSP is around -146 dB at an efficiency of 0.805. Although it is difficult to get a feeling of what the absolute values of the TSSP mean in real conditions, due to the constant thrust, the delta in TSSP is actually the same as the delta of the more subjective Sound Pressure Level (SPL). In Table 10.5, the subjective sound experience in a delta of SPL is summarised. According to this information, a change of 5 dB is already clearly noticeable, and a change of 15 dB 'significant'. This means that serious advancements on noise emissions for aviation can be made by changing the operating conditions. Figure 10.15 shows that the application of sweep can heavily affect propeller noise and efficiency. Ignoring outliers and looking mostly at the dense area in the figure, the efficiency variation due to sweep is approximately 3% point, while the TSSP variation due to sweep is approximately 9 dB. This indicates that for conventional propeller systems which cannot adjust the advance ratio, the application of sweep in blade design can be beneficial.

Table 10.5: Subjective sound experience in a delta of the sound pressure[2]

Sound Awareness	**Change in Sound Pressure (dB)**
Insignificant	1
Just perceptible	3
Clearly noticeable	5
Twice or half as loud	10
Significant	15
Much louder or quieter, four times as loud	20

Optimising propeller designs on both TSSP and efficiency could result in a less distinct relation than seen in the presented random designs in this study, but the general trend of the point clouds in Figure 10.14 suggests that the highest efficiency and lowest noise emissions cannot be achieved at the same time.

To see how some of the extreme design points behave when optimised for a different operating case, several design points have been selected for further investigation. The selected propeller designs are highlighted in Figure 10.16 and Figure 10.17. The selected points all are on the boundary, or pareto front of their case. These boundary points are used since these are predicted to have favourable performance characteristics such as low noise or high efficiency. It is interesting to see how these boundary points behave at different operating settings. All selected individuals are also evaluated using CFD and discussed in section 10.4.

Each design point has been given a label, and an overview of each design point including efficiency and TSSP is provided in Table 10.6. The pitch angle and advance ratio of each selected propeller design point from

[2]Source: https://www.engineeringtoolbox.com/sound-pressure-d_939.html, accessed on 14-08-2020

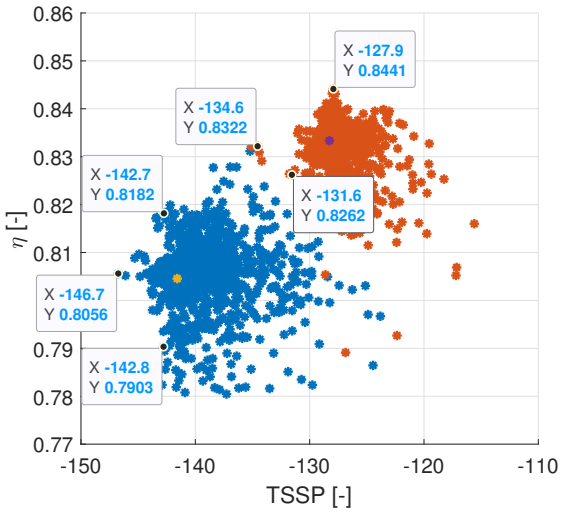

Figure 10.16: TSSP vs Efficiency relation for propeller design points on maximum efficiency and minimum TSSP

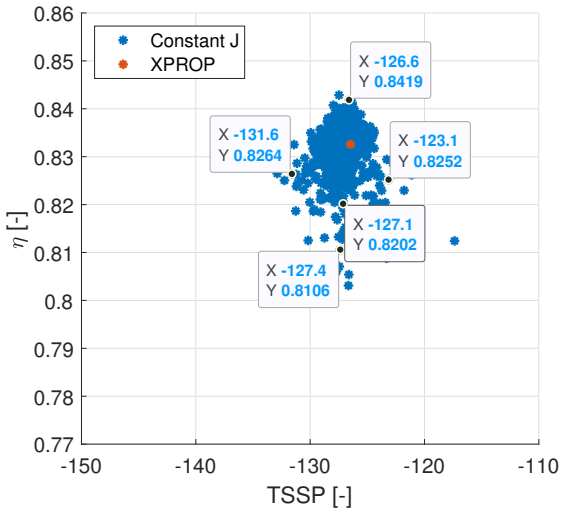

Figure 10.17: TSSP vs Efficiency relation for propeller design points on constant advance ratio

Figure 10.16 are optimised for both the cases of minimum TSSP and maximum efficiency. The goal of this is to see how much the noise can be reduced for an efficient propeller, and how much more efficient a low TSSP propeller design can be in different settings. These relations can be seen in Figure 10.29. The visualisations of each blade at 30 degree pitch angle are presented in Figure 10.18 to Figure 10.28.

Table 10.6: Characteristics of selected design points

Design	**Pitch [deg]**	**Advance Ratio [-]**	η **[-]**	**TSSP [-]**
1	47.50	2.1942	0.844	-127.9
2	52.50	2.4530	0.832	-134.6
3	47.00	2.0505	0.826	-131.6
4	59.50	3.0026	0.815	-143.3
5	59.50	2.9576	0.806	-146.7
6	59.50	2.9618	0.790	-142.8
7	48.10	2.1269	0.811	-127.4
8	48.25	2.1269	0.826	-131.6
9	47.37	2.1269	0.820	-127.2
10	46.97	2.1269	0.825	-123.1
11	46.48	2.1269	0.842	-126.6

Regarding Figure 10.29, interesting to see is that 2 out of the 3 designs selected from maximum efficiency see a large reduction in efficiency when operating at a low noise setting. Design 1 shows that a highly efficient propeller can have low TSSP characteristics at different operating settings. The designs selected from minimum TSSP all have similar noise and efficiency characteristics when operating at the settings for maximum efficiency. Also, these designs are more efficient at their maximum operating setting than 2 out of the 3 selected designs from maximum efficiency.

Figure 10.29 does show that when it is possible to change both the pitch angle and advance ratio during flight, beneficial conditions could be created in terms of noise emissions when flying in the vicinity of inhabited areas or airports. Although it is currently uncommon with fossil fuel propeller systems to be able to change the rotation speed of the propellers during flight, electric engines might be efficient at a range of rotational velocities. By changing both the pitch angle and advance ratio, an aircraft could be efficient during cruise, and silent when approaching an airport. As an aircraft is usually in the vicinity of an inhabited area for only a short amount of time, the efficiency loss when changing the propeller settings to minimum TSSP may have a small impact on the overall fuel consumption of a flight. This should however be part of a trade-off by aircraft and engine manufacturers, airline operators and legislators. The final conclusions on the dependency between efficiency and TSSP are drawn using the CFD evaluations in section 10.4.

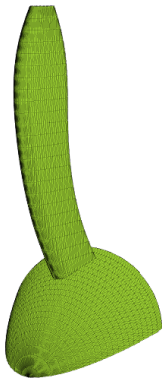

Figure 10.18: Selected propeller design 1

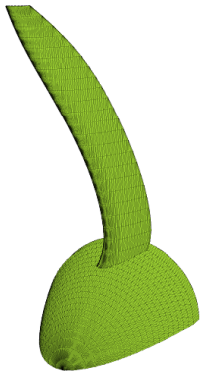

Figure 10.19: Selected propeller design 2

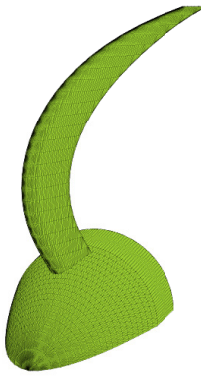

Figure 10.20: Selected propeller design 3

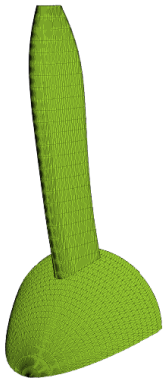

Figure 10.21: Selected propeller design 4

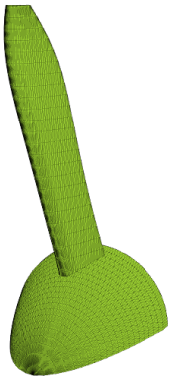

Figure 10.22: Selected propeller design 5

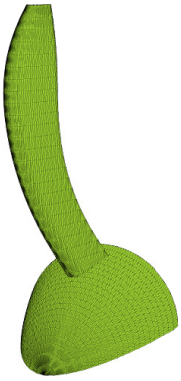

Figure 10.23: Selected propeller design 6

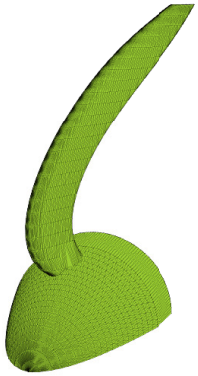

Figure 10.24: Selected propeller design 7

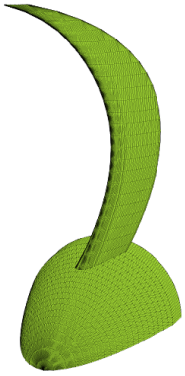

Figure 10.25: Selected propeller design 8

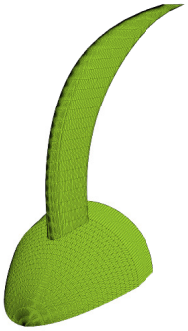

Figure 10.26: Selected propeller design 9

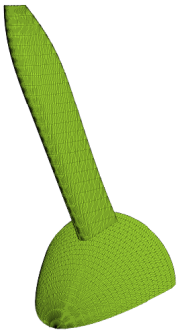

Figure 10.27: Selected propeller design 10

Figure 10.28: Selected propeller design 11

Regarding blade design, something that is not investigated in this study is whether a linear trend between the operating setting of maximum efficiency and operating setting of minimum TSSP is valid to assume. A non-linear trend could, next to the values for maximum efficiency and minimum TSSP, be an interesting differentiator between good and bad blade designs. It is recommended for future studies to look into this.

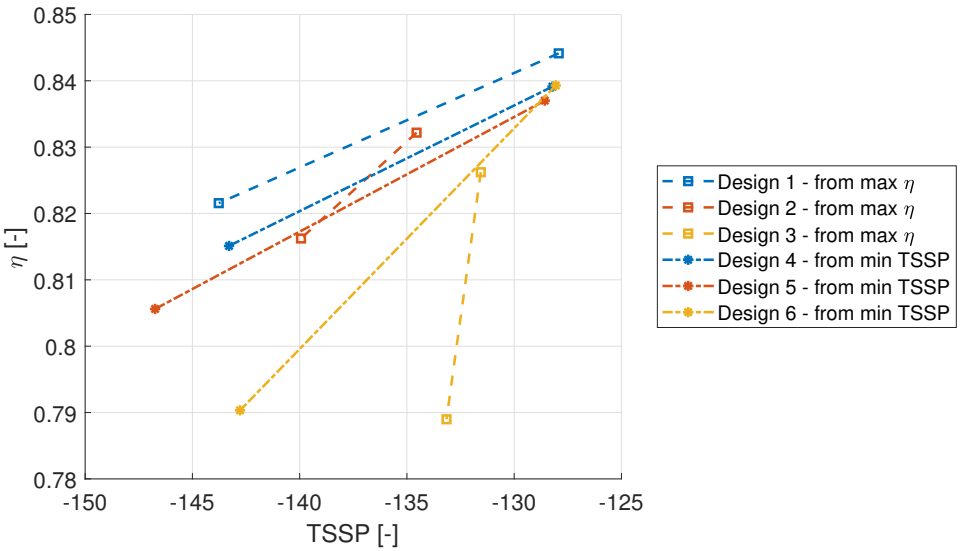

Figure 10.29: Relation of selected individuals for minimum TSSP and maximum efficiency

10.3.2. Blade Parameter Effect on Efficiency and TSSP

In this section the effect of sweep on TSSP and efficiency is investigated. This is done in three cases. In each case, the blades are evaluated at a constant thrust of 27N. To gain more insight into desirable or less desirable sweep distributions, each blade is divided into three segments of equal radial length. The local two dimensional mid chord sweep from the BEM analysis is taken at zero pitch and twist in these comparisons. The sweep is averaged over each segment, and then plotted against the efficiency and TSSP. Segment 1 closest to the root of the blade, segment 2 covers the middle section of the blade, while the third segment is closest to the tip. Contrary to the sweep definition required for the BEM implementation, the sweep in the figures is defined such that backward sweep is positive. In all figures, also black circles are placed to point out designs with favourable characteristics.

In the first case, both the pitch angle and advance ratio are adjusted to obtain the maximum efficiency. In the second case, the pitch angle and advance ratio are adjusted for minimum TSSP. In the third case, the advance ratio is kept constant and only the pitch angle can be adjusted. In all cases some additional markers are placed in the figures for the reader to track blade designs at the three segments. These markers only refer to the same design within a case.

Case 1: Constant Thrust & Maximum Efficiency

In this case both the advance ratio and pitch angle of each blade are optimised to achieve the maximum efficiency at a given thrust of 27N. To save computational time, the smallest step difference for the pitch angle is 0.25 degrees. The advance ratio does not have such a discretisation constraint due to an implementation choice made regarding the interpolation.

The sweep per segment versus the efficiency are shown in Figure 10.30, Figure 10.31 and Figure 10.32. Looking at the optimal trend, the figures suggest to apply a forward sweep of approximately -20 degrees at the root segment. Interestingly, the efficiency degrades with an increasing backward sweep, but at around 20 degrees backward sweep a small efficiency jump is seen. For segment 2, good performing blades are found with a sweep ranging from -20 to 10 degrees, while the best performing blades have forward sweep of approximately -8 degrees. A straight tip yields the highest efficiency, but for sweep angles ranging between -20 and 20 degrees still well performing designs are possible. When the tip sweep is too extreme, the efficiency clearly degrades. A backward swept root segment is not beneficial to the efficiency, while for the middle segment only a backward sweep of more than 10 degrees negatively affects the efficiency. Regarding segment 1 and 2,

reversing the sweep from forward sweep to backward sweep does not provide the same efficiency benefits. This also applies to swept wings of aircraft.

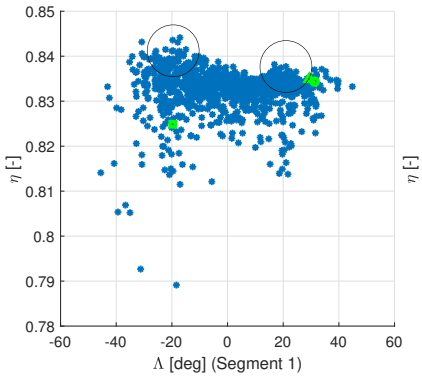

Figure 10.30: Efficiency and sweep relation for segment 1 for case 1

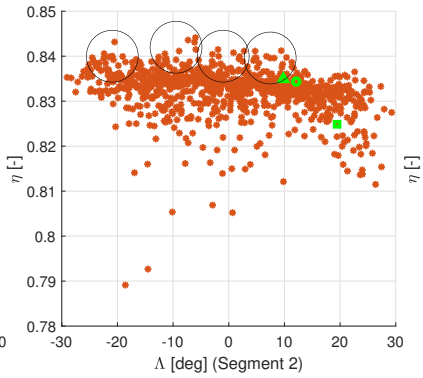

Figure 10.31: Efficiency and sweep relation for segment 2 for case 1

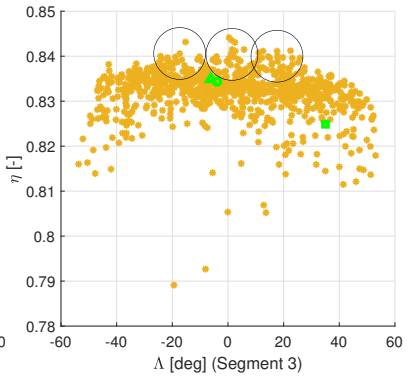

Figure 10.32: Efficiency and sweep relation for segment 3 for case 1

In regards of the TSSP, shown in Figure 10.33, Figure 10.34 and Figure 10.35, trends are less distinct. There are individual designs visible which indicate that there are either outliers or unexplored design areas. For segment 1, the best low noise characteristics are found for designs with sweep angles between -20 and 20 degrees. With more extreme angles, a severe degradation in noise performance is seen. Regarding segment 2, a very broad range of angles can give good performance. Outliers suggest that a high forward sweep between -30 and -15 degrees can result in low noise. Regarding the tip segment, the best noise performance for a forward sweep of approximately -30 degrees. However, high performing blade designs at various intervals ranging from sweep angles of -50 to 50 degrees. Important to note there is a lack of low noise data points at zero tip sweep, this indicates that a straight tip does not give good TSSP performance. The general trend in the figures is that the application of sweep can definitely reduce noise.

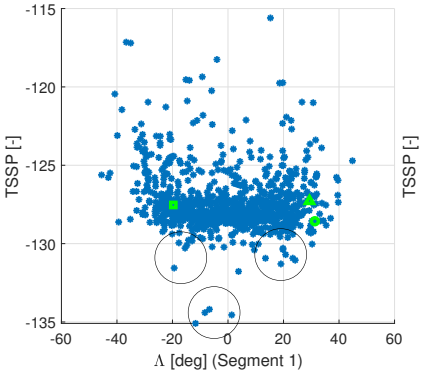

Figure 10.33: Efficiency and sweep relation for segment 1 for case 1

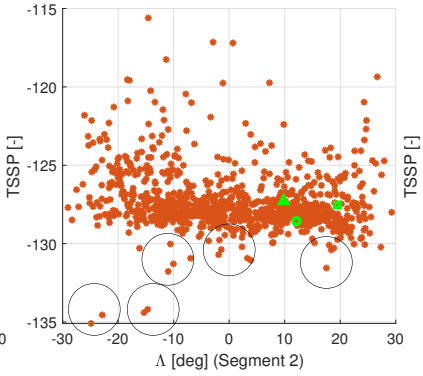

Figure 10.34: Efficiency and sweep relation for segment 2 for case 1

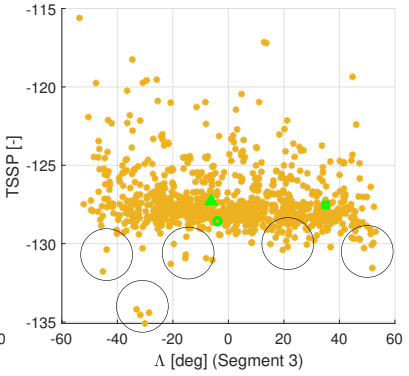

Figure 10.35: Efficiency and sweep relation for segment 3 for case 1

The most conflicting design options appear at segment 3, in which a straight tip is beneficial to the efficiency, while a swept blade reduces noise. Sweep clearly has a large effect on efficiency and TSSP. Ignoring the most extreme outliers, the efficiency can be affected by approximately 1.5% points and the TSSP can be affected by 7.5 dB. This TSSP difference is more than clearly noticeable according to Table 10.5. Sweep can be used to tweak efficiency and noise in the design process. The figures indicate that there are less design options for high efficiency than for low noise. The broad range of possible low noise designs indicates that the blade segment angles relative to each other are more important for low noise blade design than the absolute sweep angles.

Investigating the resulting pitch angles and advance ratios shows no surprises. Regarding Figure 10.36, the pitch angle resulting in the optimum efficiency is mostly found to be 47.5 degrees. In terms of efficiency and tip speed, or advance ratio, the points seem fairly clustered and do not show a very clear dependency as can be seen in Figure 10.37, although the efficiency tends to degrade slightly when the advance ratio is reduced. Figure 10.46 does show a dependency between TSSP and advance ratio. Increasing the advance

ratio, or lowering the tip velocity, generally reduces the TSSP. Following this reasoning the pitch angle will be as large as possible in case 2, since this will reduce the tip velocity and therefore reduce noise. It is expected that for case 2, a similar trend for TSSP and J is visible.

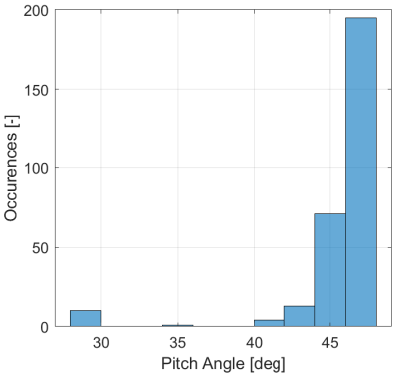

Figure 10.36: Distribution of pitch angles for maximum efficiency

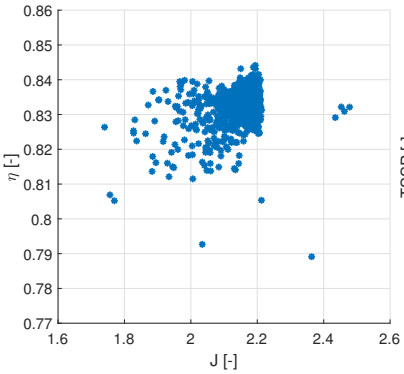

Figure 10.37: Relation between advance ratio and efficiency

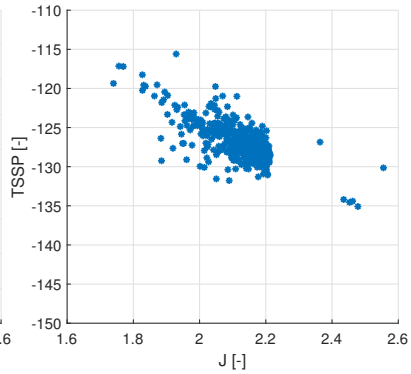

Figure 10.38: Relation between advance ratio and TSSP

Case 2: Constant Thrust & Minimum Noise

In this case both the advance ratio and pitch angle of each blade are optimised to achieve the minimum TSSP at a given thrust of 27N. To save computational time, the smallest step difference for the pitch angle is 0.25 degrees, as was also mentioned in case 1. Although the blades are operated at settings for minimum TSSP, it is still interesting to see how the blades perform in terms of efficiency. Therefore, first the efficiency is discussed again, followed by a discussion on the TSSP.

The sweep per segment versus the efficiency are shown in Figure 10.39, Figure 10.40 and Figure 10.41. Interestingly, in contrast to case 1, a high forward sweep at the root segment results the large majority of worst performing individuals in terms of efficiency. This suggests that when blades that are optimised for high efficiency are operated in conditions to minimise noise, a drastic performance hit may be taken. Still, some well performing individuals with forward sweep are present as well. The best performance is seen at a moderate to high backward sweep of approximately 20 degrees to 40 degrees. Ignoring the highly efficient outlier at segment 2 for zero sweep, Figure 10.40 indicates that a forward sweep up to -20 degrees can be beneficial to the efficiency. Low backward sweep at the middle segment negatively affects the efficiency, but increasing the backwards sweep to 20 degrees can be positive again for the efficiency. Regarding the tip, good performance is seen around -40 degrees forward sweep, zero degree sweep, and a backwards sweep of 40 degrees. However, also many bad performing blades are found at tip angles close to zero and high backwards sweep.

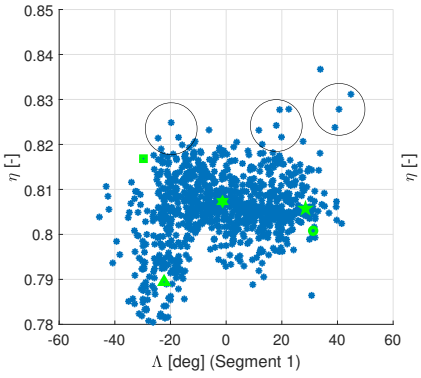

Figure 10.39: Efficiency and sweep relation for segment 1 for case 2

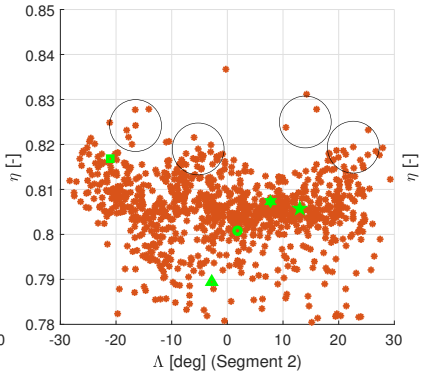

Figure 10.40: Efficiency and sweep relation for segment 2 for case 2

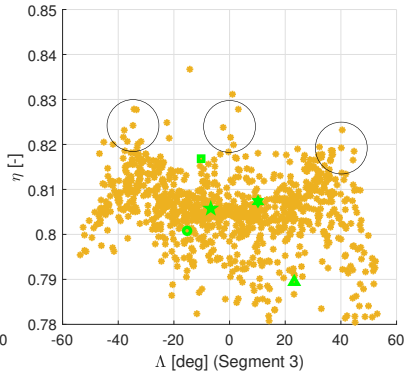

Figure 10.41: Efficiency and sweep relation for segment 3 for case 2

Regarding the computed TSSP, shown in Figure 10.42, Figure 10.43 and Figure 10.44, a large spread can be seen. Looking at the individual points, the most extreme sweep angles at segment 1 lead to higher noise emissions. The best performance is seen for a root segment sweep between -20 and 20 degrees. At the middle

segment, it is also difficult to pinpoint a clear good performing design point. At approximately -10 degrees, some outliers are seen. However, it can be concluded that generally speaking, a middle segment sweep between -15 and 15 degrees can result in quiet blades. Segment 3 indicates a slight preference to a forward sweep between 0 and -20 degrees. A blade with a high backwards swept tip of 40 degrees does seems to take a harsher noise penalty than a blade with a reversed -40 degree forward swept design.

The large spread in the TSSP figures suggests that multiple design philosophies are possible for low noise blade design. Just looking along the -144 dB value on the TSSP axis shows that for each segment, a large range of sweep values could yield low noise blades. The same is true in reverse, almost the complete sweep range can also result in high noise blades. Ignoring the most extreme outliers, a 10 to 15 dB difference can be found between the best and worst designs. Table 10.5 indicates this difference perceived as 'significant'.

Regarding the design philosophy, comparing markers gives some insights into good and bad designs. Starting with the circle and triangle, which are approximately mirrored blade designs. Looking first at the efficiency shows that the circle is approximately 1% point more efficient. The TSSP figures show a much more extreme difference. The circle is amongst the worst performing designs at a TSSP of approximately -135, while the triangle is amongst the best performing designs with a predicted TSSP of approximately -143. This is a difference of 12 dB while differing slightly in efficiency. The circle blade has a backward swept root segment, an almost neutral middle segment and a forward swept tip segment. The triangle design is reversed from this. Just like the circle, the pentagram marker also starts with a backward sweep. However, the middle segment is moderately swept backward, while the tip as a small sweep forward. This design has a TSSP of approximately -142, which is a huge difference with the circle marker. The efficiency difference between the pentagram marker and circle marker is approximately 0.5% point. Interesting to see is also that the square marker has an approximate 1.8% point higher efficiency than the circle, but they differ only 2.5 dB in noise.

A possible reason for some design options being geometrically close to each other while being on the opposite ends of the spectrum of noise performance is the sensitivity of noise to interference and phase delay. A sweep offset causes phase differences of the acoustic pressure along the blade radius. These phase differences can positively or negatively interfere with each other. Both forward and backward sweep result in the phase differences, which explains why both design types can result in approximately the same TSSP. The relative sweep differences between segments may be the driving factor for why sweep can affect noise the way it is presented here. It is recommended for future studies to focus on this phase difference. Integrating the 'sweep rules' of noise cancelling phase interference in a blade design routine as constraints may reduce the number of evaluations required to find a low noise blade design.

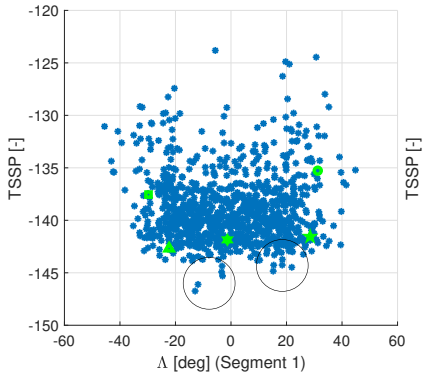

Figure 10.42: Efficiency and sweep relation for segment 1 for case 2

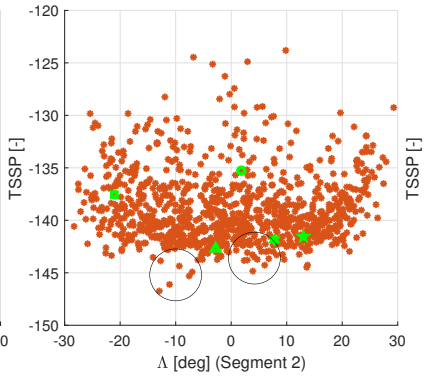

Figure 10.43: Efficiency and sweep relation for segment 2 for case 2

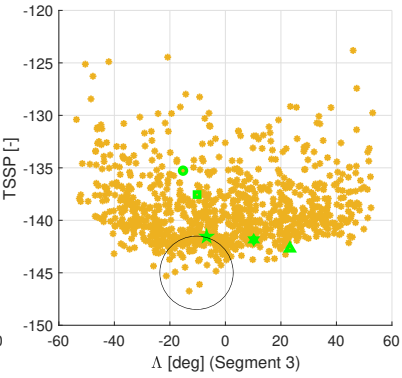

Figure 10.44: Efficiency and sweep relation for segment 3 for case 2

As can be seen in Figure 10.45, most pitch angles are centred around 57 degrees. The pitch angles in this case are higher than the pitch angles found in case 1. This is due to the higher advance ratios required when operating at higher pitch angles to achieve the same thrust. Increasing the advance ratio means lower velocities at the tip of the blade, which reduces noise emissions. This trend is visible in case 1, and it is also visible in this case in Figure 10.47. Given that in this current case the blades are not operating at their optimum efficiency condition, Figure 10.46 shows a large spread.

Case 3: Constant Thrust & Advance Ratio

The advance ratio in this case is kept constant at a value of $J = 2.1269$. This advance ratio is the mean of the advance ratios found in Case 1, when the pitch angle and advance ratio are optimised for maximum efficiency.

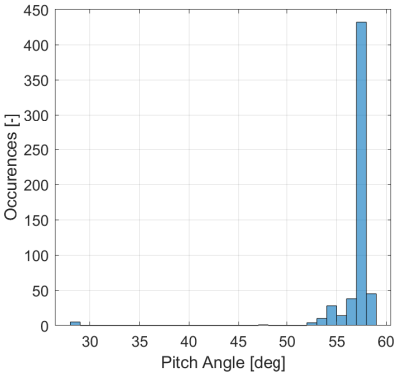

Figure 10.45: Distribution of pitch angles for minimum TSSP

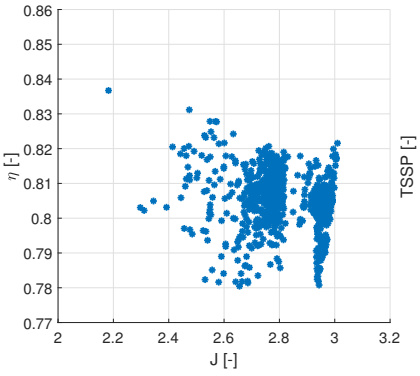

Figure 10.46: Relation between advance ratio and efficiency

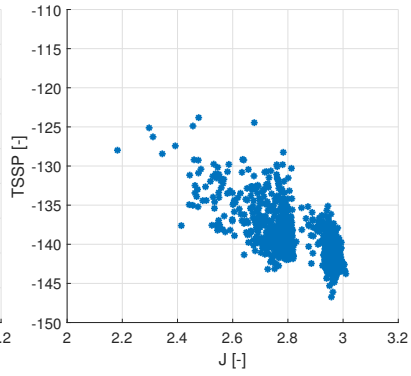

Figure 10.47: Relation between advance ratio and TSSP

The sweep per segment versus the efficiency are shown in Figure 10.48, Figure 10.49 and Figure 10.50.

Similar trends to case 1 are visible. Looking at the trend of the most efficient individuals, the efficiency benefits from a relative high forward sweep in the first segment between approximately -20 and -30 degrees. Segment 2, the middle segment, has the most efficient designs around -20 degrees forward sweep and -8 degrees forward sweep. A small backward sweep could be beneficial, but not as much as the forward swept middle segments. The general trend of both segment 1 and 2 is that a forward sweep results in higher efficiencies than backwards swept wings. Regarding the tip, any high forward or backward sweep results in efficiency penalties. A straight tip seems beneficial, but moderate forward or backward tip sweep can be applied as well for some designs.

As was seen in case 1, reversing the sweep from forward sweep to backward sweep does not provide the same efficiency benefits. Possibly, interactions between the spinner and the blade partly cause this effect. Root effects could be favourable for a forward swept blade. Another explanation can be the constraint of the sweep parametrisation. The parametrisation only allows for straight or banana-shaped blades. A forward swept middle segment can be favourable, but this can only be achieved in the parametrisation if the root segment is also swept forward. It is recommended that an additional control point is added for the sweep parametrisation in future studies to investigate this. It is at least visible that a forward sweep is preferred for both the first and second segment. This can lead to a favourable radial force distribution. When only the pitch angle can be adjusted to get the required thrust, sweep heavily affects the efficiency. Following the most dense trend for efficiency, sweep affects the efficiency in a bandwidth of approximately 1.5% point.

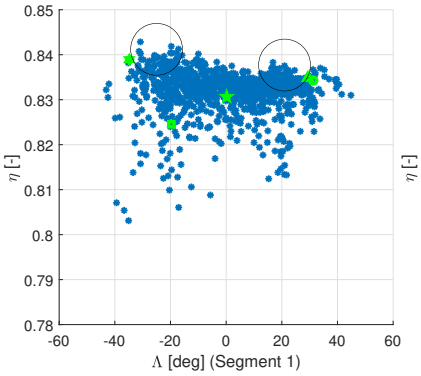

Figure 10.48: Efficiency and sweep relation for segment 1 for case 3

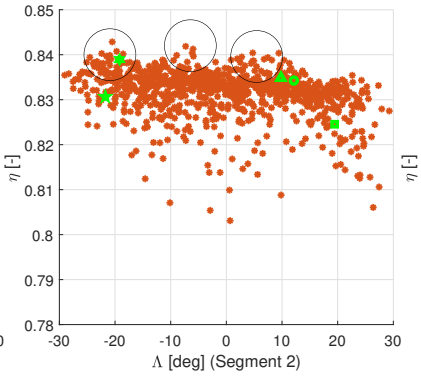

Figure 10.49: Efficiency and sweep relation for segment 2 for case 3

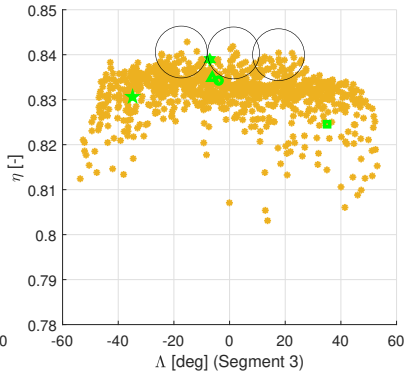

Figure 10.50: Efficiency and sweep relation for segment 3 for case 3

The TSSP performance per segment is presented in Figure 10.51, Figure 10.52 and Figure 10.53. The dense data point band in segment 1 does not indicate a clear trend. Looking at the best individuals does suggest that either a forward or backward sweep of approximately -20 or 20 degrees can yield favourable noise performance. For segment 2 a larger spread can be seen, although the two best performing designs have a forward sweep middle segment between -10 and -15 degrees. Segment 3 does show a more clear trend. Either a high sweep forward or backward is favourable. At around 50 degrees forward or backward sweep, the best TSSP

performance can be seen.

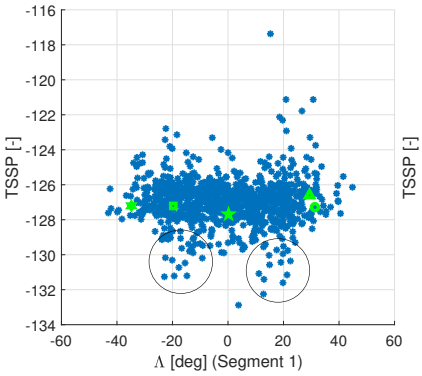

Figure 10.51: Efficiency and sweep relation for segment 1 for case 3

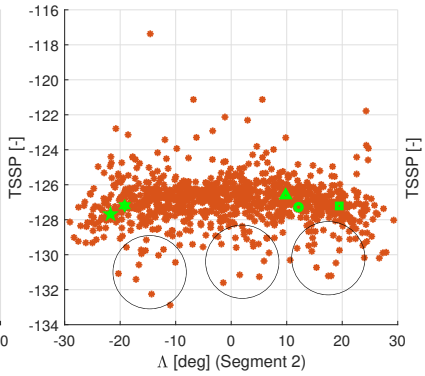

Figure 10.52: Efficiency and sweep relation for segment 2 for case 3

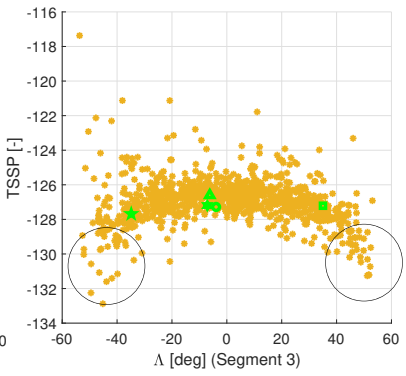

Figure 10.53: Efficiency and sweep relation for segment 3 for case 3

Combining the trends for both efficiency and TSSP, a clear design conflict is present for segment 3. The most efficient blades only have a moderate tip sweep, while the most quiet blades have a high tip sweep. Tip sweep changes the perceived velocity normal to the local spanwise direction, which leads to lower tip loading. While the efficiency benefits from a higher tip loading, this also increases noise emissions. Interesting to see is that while the placed markers vary clearly in terms of efficiency, their noise performance is very similar.

Regarding the TSSP, the bandwidth of the dense points is in the order of approximately 5 dB. This change in sound pressure is clearly noticeable according to Table 10.5.

Lastly for this case, the pitch angles are visualised. Since the advance ratio is kept constant in this case, it is of no use to look at the relation of advance ratio and efficiency and noise. As can be seen in Figure 10.54, most pitch angles are centred around 46.5 degrees in this case. The best designs in Figure 10.55 indicate that increasing the pitch angle may reduce the TSSP, although it should be noted that the worst performing design has the largest pitch angle in this case.

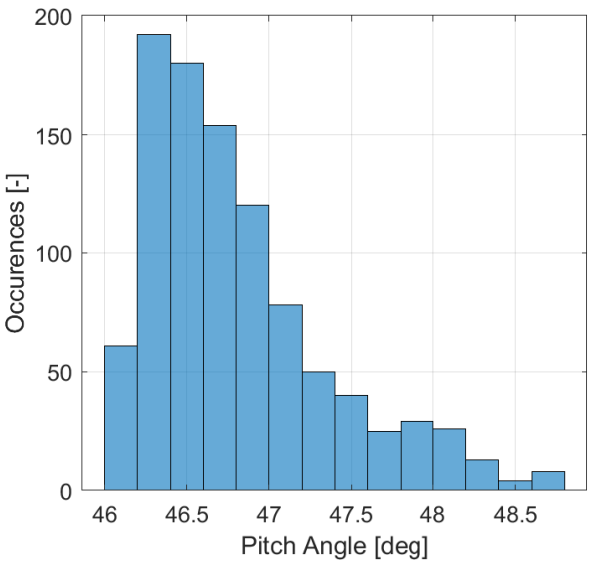

Figure 10.54: Distribution of pitch angles for maximum efficiency

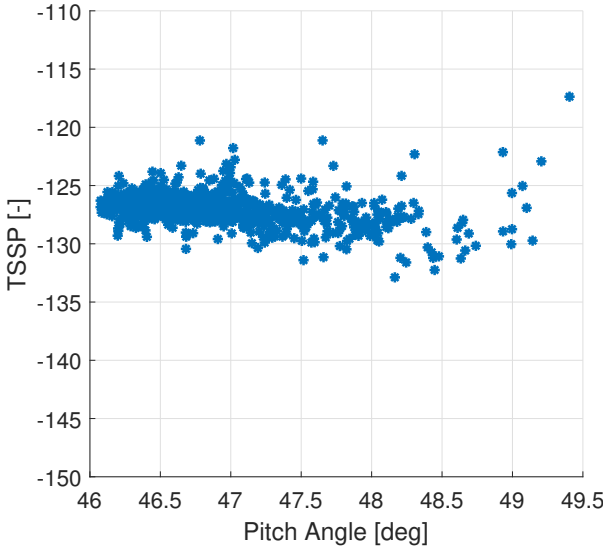

Figure 10.55: Relation between pitch angle and TSSP for a constant advance ratio

10.4. Final Remarks on Numerical Results

In this final section, some last remarks and conclusions on the numerical data are given. The selected designs from Figure 10.29 are evaluated by CFD to check if the conclusions made on the kriging results are correct. This is discussed in subsection 10.4.1. Lastly, in subsection 10.4.2, a Pareto front is presented based on the kriging results.

10.4.1. CFD Check on Selected Designs

In this subsection, the selected designs from subsection 10.3.1 are investigated in more detail. All designs have been evaluated by CFD at the optimal conditions for both TSSP and efficiency as were found by the kriging model. An overview of the evaluated results can be found in Figure 10.56. Designs 7 to 11 were evaluated at a constant advance ratio.

Regarding the designs selected on minimum TSSP and maximum efficiency, differences can be seen in Figure 10.56 compared to the kriging predictions from Figure 10.29. With exception of design 1, the maximum efficiencies are predicted very well by the kriging model. For the minimum efficiency, slightly more designs show discrepencies, but again design 1 shows the largest discrepancy. An overview of the differences between the predicted and computed results is given in Table 10.7, Table 10.8, Table 10.9, and Table 10.10. The thrust is not perfectly predicted, but conclusions regarding the general trends should still be valid.

The harsh penalty for changing the operating settings from the point of maximum efficiency seen in Figure 10.29 for design 2 and 3 are less distinct in Figure 10.56. Still, the gradient is a little steeper than seen for designs 1, 4 and 5. The points of maximum efficiency all lie between 0.826 and 0.836, while the efficiencies at the low noise operating conditions do lie more apart. In this case, design 6 seems the most efficient propeller, and it has the largest penalty in efficiency when operating at low noise conditions. However, a design such as design 1 has an almost similar maximum efficiency, but a much higher efficiency at low TSSP settings compared to design 6. A previous stated hypothesis that the most efficient propellers are not the best low noise designs cannot clearly be confirmed or denied based on the CFD evaluations. But what is clearly visible is that propellers operating at their maximum point of efficiency produce more noise than the minimum possible noise emissions for a given design.

Investigating the slopes, the average gradient is 0.0026, meaning that with every dB change in TSSP, the efficiency will change by 0.26% point. The maximum change in TSSP from the point of maximum efficiency appears to be approximately 13 dB. When design optimisation is performed, this could potentially be increased. From this it can be concluded that for a given propeller design operating at maximum efficiency, the TSSP can be improved by 13 dB for an approximate 3.4% point drop in efficiency by only tuning the pitch angle and reducing the advance ratio. As mentioned before, this may be interesting for propeller aircraft with electric powered propellers since the electric engines may be able to efficiently vary the rpm. Temporarily changing the operating conditions for aircraft or drones when flying over urban areas could reduce the perceived noise by a factor 2 (Table 10.5), with only a small hit in efficiency for a short duration of time.

Interesting is that the designs with a steeper slope seem to have a tendency to have more backwards or forward sweep than the designs with a less steep slope (see Figure 10.18 to Figure 10.28). Although design 2 has a relative small noise reduction between the point of maximum efficiency and minimum TSSP, it does have very good noise performance at the point of maximum efficiency, while having only a slightly lower maximum efficiency than the best performing blade designs. Having both the best TSSP and efficiency performance at the same time does not seem possible.

As was already mentioned regarding Figure 10.29, the linear trend indicated from maximum efficiency and minimum TSSP is not necessarily true. Varying non linear behaviour in terms of efficiency and TSSP when moving to different operating settings could also be a differentiator between good and bad blade designs. It is recommended that this is investigated in future research.

Regarding the designs selected for the constant advance ratio case, shown in Figure 10.56, larger discrepancies are seen between the CFD results and kriging results. From this figure it is more difficult to draw definite conclusions. An approximate 3 dB TSSP improvement can be seen solemnly from the sweep, while an approximate 1.2% point difference in efficiency is visible. It suggested more points at constant J are evaluated in a future study to be able to draw more clear conclusions. Figure 10.15 does show that when being constrained to a fixed advance ratio, the application of sweep can potentially result in a TSSP variation of 9 dB or more between good and bad designs.

10.4.2. Pareto Front

As a final addition to this thesis, a Pareto front for noise and efficiency is presented in Figure 10.57. A Pareto front indicates a trade-off between variables in which better performance of one variable leads to reduced performance of another variable. A rough sketch of the best individuals on the boundaries of the point clouds was already provided in Figure 10.14. In this subsection, a smoothing spline as been fitted through some of the best individuals for the cases of minimum TSSP and maximum efficiency. The points used to fit this spline are also indicated in the figure.

The figure presented here ultimately shows that there clearly is a trade-off to be made during blade de-

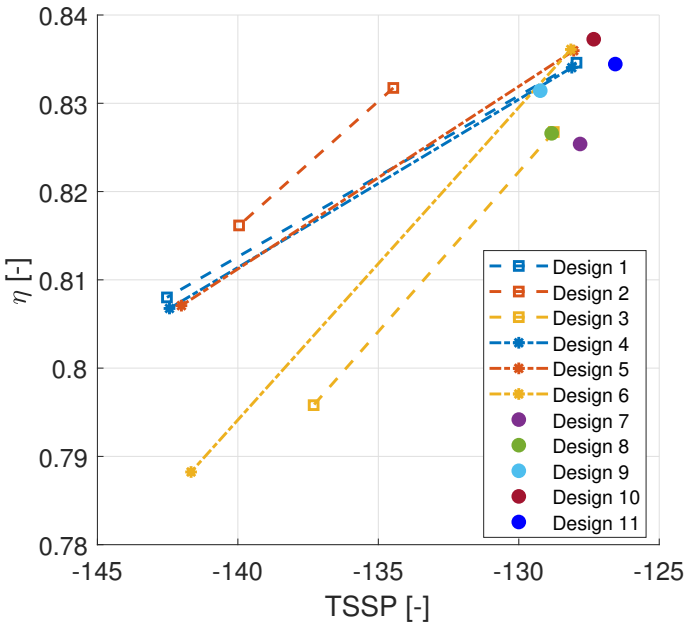

Figure 10.56: Relation of selected individuals for minimum TSSP and maximum efficiency and a constant advance ratio - CFD

Table 10.7: Cmparison of predicted thrust with CFD evaluations

Design	Ref. Thrust [N]	Thrust at Max. η [N]	Thrust at Min. TSSP [N]
1	27	27.16	26.21
2	27	26.93	26.97
3	27	26.92	27.60
4	27	26.81	26.45
5	27	27.36	27.44
6	27	27.55	26.81

Table 10.8: Comparison of predicted TSSP with CFD evaluations

Design	Predicted Max. TSSP [-]	CFD Max. TSSP [-]	Predicted Min. TSSP [-]	CFD Min. TSSP [-]
1	-127.9	-127.9	-143.8	-142.5
2	-134.6	-134.5	-139.9	-140.0
3	-131.6	-128.8	-133.2	-137.3
4	-128.2	-128.1	-143.3	-142.4
5	-128.6	-128.0	-146.7	-142.0
6	-128.1	-128.1	-142.8	-141.7

Table 10.9: Comparison of predicted efficiency with CFD evaluations

Design	Predicted Max. η [-]	CFD Max. η [-]	Predicted Min. η [-]	CFD Min. η [-]
1	0.844	0.835	0.822	0.808
2	0.832	0.832	0.816	0.816
3	0.826	0.827	0.789	0.796
4	0.839	0.834	0.815	0.807
5	0.837	0.836	0.806	0.807
6	0.839	0.836	0.790	0.788

Table 10.10: Comparison of predicted values with CFD evaluations for the case of constant advance ratio

Design	**Ref. Thrust [N]**	**CFD Thrust [N]**	**Predicted TSSP [-]**	**CFD TSSP [-]**	**Predicted η [-]**	**CFD η]-]**
7	27	28.32	-127.4	-127.8	0.811	0.825
8	27	28.01	-131.6	-128.8	0.826	0.827
9	27	26.82	-127.2	-129.2	0.820	0.831
10	27	27.55	-123.1	-127.3	0.825	0.837
11	27	27.50	-126.6	-126.6	0.842	0.834

sign regarding noise performance and efficiency performance. The difference in TSSP between the point of maximum efficiency and minimum TSSP is almost 19 dB, while the difference in efficiency is 3.89% point. Assuming a linear relation, the average slope is 0.0021. This is a slightly less steep slope than seen in the previous subsection, although here the slope is between different blades instead of the same blade operating at varying conditions.

The Pareto front does look steeper towards the low end of the TSSP values. This can indicate that beyond a certain threshold, it becomes more expensive in terms of efficiency to reduce the noise emissions.

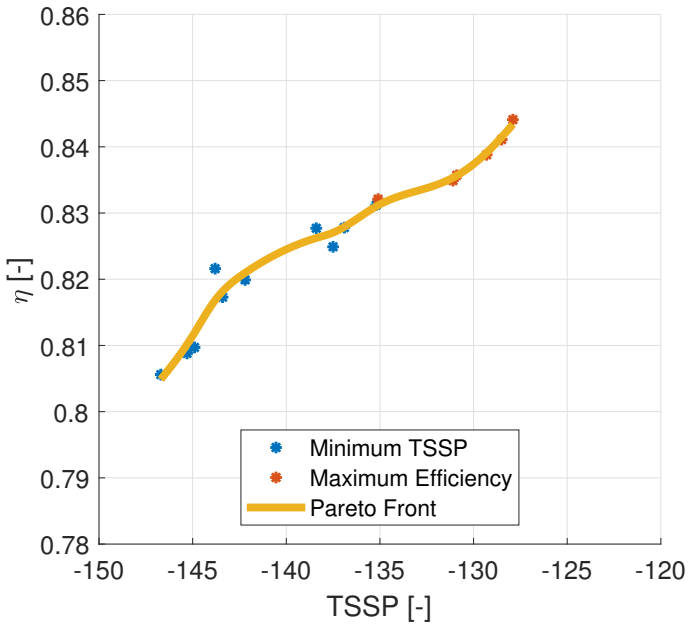

Figure 10.57: Smoothed Pareto front from the boundary points of the minimum TSSP case and maximum efficiency case

IV

Conclusions & Recommendations

11

Conclusion and Recommendations

In this thesis 993 different propeller designs have been successfully evaluated to quantify the dependency between propeller efficiency and noise, and to investigate how pitch, sweep and rotational speed can be used to maximise or minimise one or the other. In this chapter, the conclusions of this work are summarised and recommendations for future work are given.

11.1. Conclusion

The main objective for this thesis was to quantify the dependency between propeller efficiency and propeller noise emissions for an isolated, unducted propeller using a combination of low-order and high-order analysis tools. This objective is met in this study.

For the propeller flow analysis, two methods have been utilised with a varying level of fidelity. The low order method is a new BEM method from Rosen and Gur[8] which deviates from classical methods in that a sensitivity to sweep is incorporated. Comparisons with RANS simulations show that the method can provide reasonable results, but that strong sweep gradients and large out of plane translation can severely degrade the results. For the higher fidelity method, compressible RANS simulations are performed with a Spalart-Allmaras turbulence model. Validation indicates not a perfect agreement with experimental data, especially at higher advance ratios. This discrepancy may partially be caused by the low Reynolds number at which the propeller is operated in the experiment. The noise is computed using the frequency formulation from Hanson. Notable from verification is that the directivity plots indicate that the blade thickness, or volume, seems to dominate the noise emissions at higher advance ratio. However, this observation is not independent of the blade Mach number. The results from BEM and RANS show reasonable agreement.

The results from all tools are combined into one surrogate model by kriging. Comparing the kriging results with CFD evaluations shows that the average absolute kriging errors for C_T, η and TSSP are $2.19 \cdot 10^{-3}$, $5.40 \cdot 10^{-3}$ and $8.78 \cdot 10^{-1}$ respectively. The average values show good agreement, but some outliers were found when selecting some outstanding designs. The additional iteration that was performed did visually result in less outliers and made the point clouds for the case of maximum efficiency and case of minimum TSSP more distinct. The differences seen when selecting individual designs do indicate that more iterations might be required for more reliable results. Despite of this, kriging does show to be able to generate results which closely resemble CFD simulations on blade designs of which no CFD evaluations are provided in the training data.

Pitch and advance ratio are used in this study to achieve the required thrust. Aiming to increase the advance ratio appears more important to low noise emissions than aiming for high pitch angles. Naturally, at higher advance ratios, higher pitch angles are more common. For minimum noise, it is beneficial for the Mach number at the tip to be as low as possible. The pitch angle is for minimum noise is centred around 58, which results in a higher advance ratio than what is seen at the most efficient conditions. Increasing the pitch angle to limit noise emissions reduces the efficiency. A relation between efficiency and noise is found. This relation suggests that for a given blade design, there is a 0.26% point penalty in efficiency for every dB reduction of TSSP by adjustment of the pitch and advance ratio. The results show that adjusting the pitch and advance ratio could potentially reduce the TSSP by up to 13 dB at the cost of 3.4% point efficiency. This means that the perceived sound can be reduced by more than a factor 2 for a given design. As mentioned

before, electrically propelled aircraft could benefit from this finding in that the operating conditions might be temporarily adjusted when flying in urban areas. Since this usually is only for a short duration, the fuel consumption of the overall flight will not increase much while noise emissions are much reduced.

Regarding sweep, it is found that different or even opposite designs can lead to the same results. The kriging results for a constant advance ratio indicate that there is a spread of approximately 9 dB between good and bad designs, while a spread of approximately 3% point is seen in the efficiency. When looking at the CFD evaluations for the case of constant advance ratio, the spread in TSSP is only around 3 dB, while the spread in efficiency is approximately 1.2% point. Regarding design recommendations from the results, the low noise case indicates that many different design options are possible for the reduction of TSSP. It is suggested that mechanism of interference by the phase differences due to sweep is an important factor in noise reduction. Although offloading the tip has benefits for the TSSP in the maximum efficiency case, the minimum TSSP case suggests that the relative sweep differences between segments of the blade may be more leading in good or bad TSSP characteristics. What is consistent in all cases is that a moderate forward or backward sweep of approximately 20 degrees can be beneficial to the TSSP. For the efficiency, the results show a preference for a forward swept root and middle segment, and a straight blade.

Combining the point clouds for the case of maximum efficiency and case of minimum TSSP shows the existence of a Pareto front for noise and efficiency. Between the point of maximum efficiency and minimum noise, a difference of 19 dB is seen, while the difference in efficiency is 3.89% point. The average slope of the front is found to be 0.0021, meaning an efficiency change of 0.21% point is seen for every dB change in TSSP.

To conclude, this study shows that maximum efficiency and minimum noise cannot be obtained at the same time when only adjusting the sweep, pitch and advance ratio. Efficient blades do seem to be able to operate in low noise conditions at the cost of some efficiency. During design, sweep can be an important parameter to tweak the efficiency and TSSP. During propeller operation, noise emissions can be reduced when increasing the advance ratio and pitch angle.

11.2. Recommendations

The following recommendations for future studies are made:

- The BEM method should be reconsidered. A sensitivity to sweep is present, but large out of plane translation of the blade leads to discrepancies. More expensive methods better capable of analysing swept blades should be investigated. Maybe even Euler codes could be feasible.
- An additional control point should be added to the sweep parametrisation. This allows for more variation in the shape for backward and forward sweep, which can shed more light on some effects seen in the presented results in this work.
- More parameters should be included in the investigation of efficiency and TSSP. The framework created for this study already supports parametrisation of the twist, chord length and blade radius. The only limiting factor is computational resources, since much more data points will have to be generated.
- Iterating more on the outliers generated by the kriging model can increase the accuracy and reliability of the overall results.
- In future studies, more focus should be put on the phase delay caused by sweep. Investigating this phase delay can lead to more insights and general design rules to blade design for efficient, low noise propellers.
- Besides generating random blades, an optimisation routine should be added. This may result in a more clear trade-off between efficiency and noise and blade parameters, as relative weights could be included to focus more on efficiency or on noise. This could also shed more light on the on the validity of the assumption of a linear relation between efficiency and noise as is assumed in the results of this study.
- Since this research was centred around isolated propellers, interaction and noise interference effects with wing and body have to be investigated as follow-up before true design guide lines for propellers in real-life applications can be made.

A

Mesh Grid Generation Parameters

The grid generation parameters used in this study are summarised in Table A.1. These values are used for propellers with a diameter of 0.4064 m.

Table A.1: Final mesh grid generation parameters

Parameter	**Value**	**Unit**
Min. Global Cell Size	0.065	mm
Max. Global Cell Size	58.5	mm
Global Growth Rate	1.2	-
Min. Proximity Size	0.13	mm
Max. Proximity Size	1.3	mm
Proximity Cells	3	#
Min. Face Cell Spinner/Blade	0.13	mm
Max. Face Cell Spinner/Blade	1.3	mm
Curvature Normal Angle	7	deg
Min. Face Cell Nacelle Inflation	0.13	mm
Max. Face Cell Nacelle Inflation	7	mm
Max. BoI Blade Cell Size	10.4	mm
Max. BoI Upstream/Downstream Cell Size	20.8	mm
Number of Layers Blade/Spinner	20	#
Number of Layers Extension 1	5	#
Number of Layers Extension 2	4	#
Number of Layers Extension 3	3	#

B

Kriging Validation Error

The errors for each kriging validation design are summarised in the tables in this appendix.

B.1. Kriging Errors Initial Model

Here, the kriging errors of the initial model are presented.

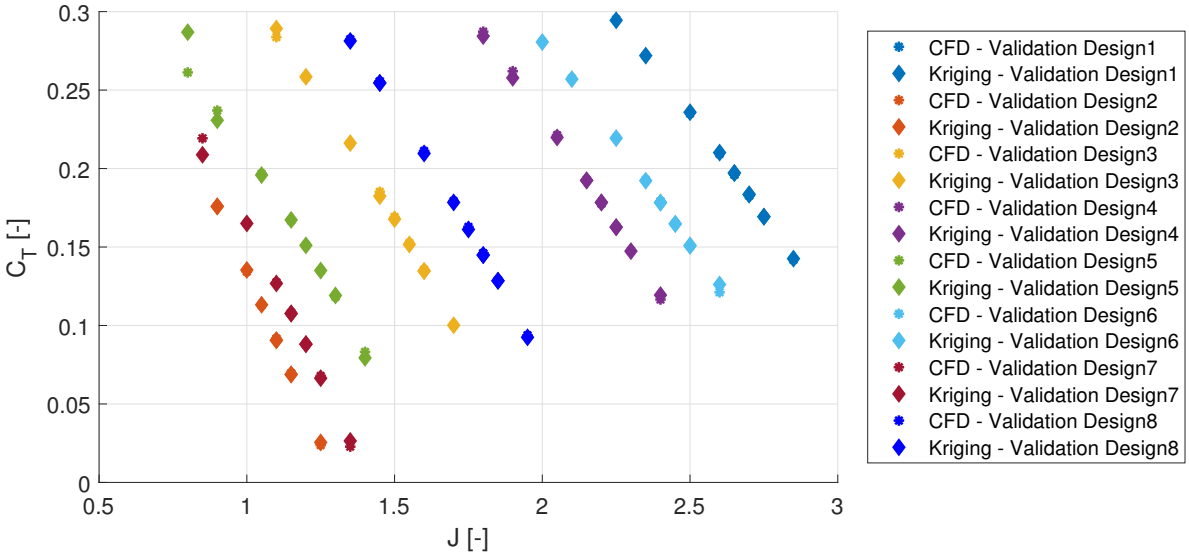

Figure B.1: Thrust coefficient comparison between kriging and RANS for the initial kriging model

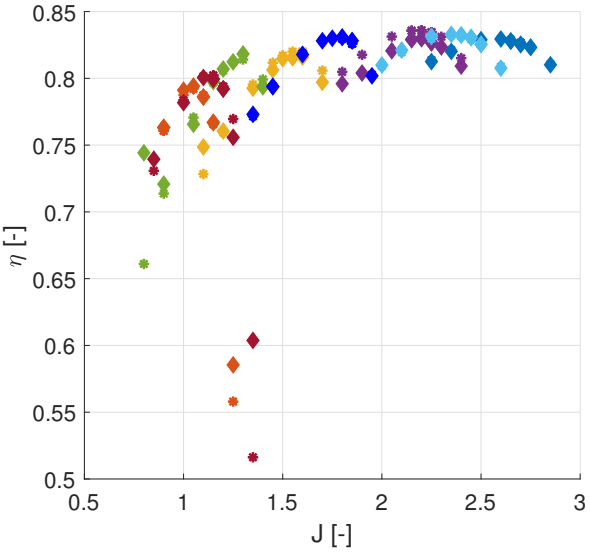

Figure B.2: Efficiency comparison between kriging and RANS for the initial kriging model

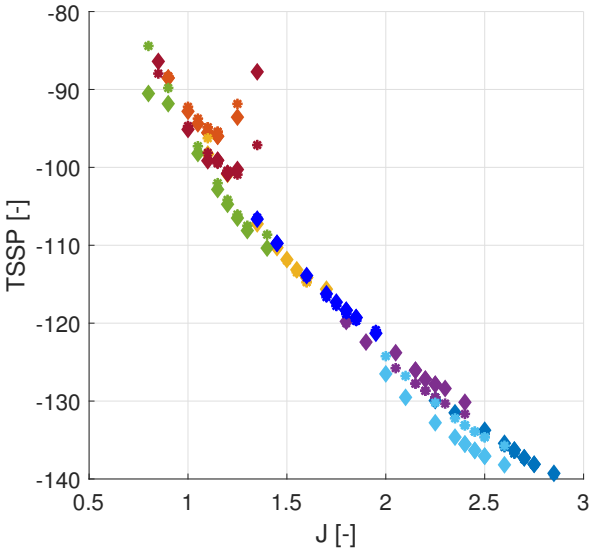

Figure B.3: TSSP comparison between kriging and RANS for the initial kriging model

Table B.1: Absolute C_T errors kriging vs CFD for the initial kriging model

Validation Design	Pitch Angle [deg]	Min. Error	Max. Error	Mean Error	Standard Dev.
1	52.63	4.44E-06	9.84E-04	5.69E-04	3.72E-04
2	27.35	1.20E-04	1.72E-03	7.18E-04	5.33E-04
3	38.60	9.16E-05	5.45E-03	1.44E-03	1.71E-03
4	47.79	1.54E-04	4.24E-03	1.23E-03	1.44E-03
5	33.58	5.07E-05	2.56E-02	4.74E-03	8.72E-03
6	49.93	1.61E-04	5.00E-03	8.23E-04	1.40E-03
7	30.38	1.01E-04	1.05E-02	1.94E-03	3.40E-03
8	41.63	3.90E-04	1.65E-03	1.05E-03	4.13E-04

Table B.2: Absolute η errors kriging vs CFD for the initial kriging model

Validation Design	Pitch Angle [deg]	Min. Error	Max. Error	Mean Error	Standard Dev.
1	52.63	8.75E-05	1.30E-03	6.91E-04	4.81E-04
2	27.35	1.04E-03	2.75E-02	4.75E-03	8.57E-03
3	38.60	1.01E-03	2.02E-02	5.91E-03	5.79E-03
4	47.79	5.96E-03	1.37E-02	8.00E-03	2.35E-03
5	33.58	3.72E-04	8.32E-02	1.34E-02	2.83E-02
6	49.93	1.09E-04	1.63E-03	8.96E-04	4.91E-04
7	30.38	8.51E-04	8.75E-02	1.35E-02	2.81E-02
8	41.63	5.03E-05	2.27E-03	9.67E-04	8.03E-04

Table B.3: Absolute TSSP errors kriging vs CFD for the initial kriging model

Validation Design	Pitch Angle [deg]	Min. Error	Max. Error	Mean Error	Standard Dev.
1	52.63	8.44E-03	4.96E-01	2.71E-01	1.82E-01
2	27.35	2.22E-01	1.71E+00	6.60E-01	4.34E-01
3	38.60	5.61E-03	2.03E+00	5.51E-01	6.11E-01
4	47.79	2.46E-02	1.98E+00	1.41E+00	6.54E-01
5	33.58	4.47E-01	6.11E+00	1.66E+00	1.88E+00
6	49.93	2.27E+00	2.75E+00	2.45E+00	1.19E-01
7	30.38	3.33E-01	9.40E+00	1.61E+00	2.95E+00
8	41.63	2.03E-02	4.92E-01	3.21E-01	1.76E-01

B.2. Kriging Errors Additional Iteration

Here, the kriging errors after one additional iteration are presented.

Table B.4: Absolute C_T errors kriging vs CFD after an additional iteration on the kriging model

Validation Design	Pitch Angle [deg]	Min. Error	Max. Error	Mean Error	Standard Dev.
1	52.63	2.63E-04	2.71E-03	8.08E-04	6.85E-04
2	27.35	3.64E-04	3.85E-03	1.24E-03	1.08E-03
3	38.60	2.71E-04	2.42E-03	1.15E-03	8.25E-04
4	47.79	4.86E-04	5.87E-03	2.67E-03	1.77E-03
5	33.58	3.24E-04	2.63E-02	4.88E-03	8.81E-03
6	49.93	8.82E-05	7.53E-03	1.88E-03	2.40E-03
7	30.38	1.21E-03	7.66E-03	4.54E-03	1.90E-03
8	41.63	3.68E-04	2.24E-03	1.11E-03	5.62E-04

Table B.5: Absolute η errors kriging vs CFD after an additional iteration on the kriging model

Validation Design	Pitch Angle [deg]	Min. Error	Max. Error	Mean Error	Standard Dev.
1	52.63	5.80E-05	1.27E-03	4.94E-04	4.18E-04
2	27.35	1.06E-03	3.36E-02	5.56E-03	1.06E-02
3	38.60	3.87E-04	1.89E-02	5.62E-03	5.50E-03
4	47.79	1.77E-03	1.39E-02	6.14E-03	3.97E-03
5	33.58	9.82E-05	8.51E-02	1.39E-02	2.89E-02
6	49.93	4.81E-05	1.76E-03	8.71E-04	6.33E-04
7	30.38	4.66E-05	8.86E-02	1.37E-02	2.85E-02
8	41.63	1.30E-04	2.52E-03	8.77E-04	8.06E-04

Table B.6: Absolute TSSP errors kriging vs CFD after an additional iteration on the kriging model

Validation Design	Pitch Angle [deg]	Min. Error	Max. Error	Mean Error	Standard Dev.
1	52.63	1.32E-02	5.33E-01	2.06E-01	1.70E-01
2	27.35	1.32E-02	2.27E+00	4.35E-01	7.01E-01
3	38.60	5.25E-02	1.73E+00	5.29E-01	5.31E-01
4	47.79	8.97E-01	3.05E+00	2.05E+00	6.98E-01
5	33.58	3.21E-01	5.35E+00	1.53E+00	1.68E+00
6	49.93	5.86E-02	7.28E-01	3.37E-01	2.11E-01
7	30.38	1.36E-01	1.07E+01	1.75E+00	3.40E+00
8	41.63	1.26E-01	5.20E-01	3.75E-01	1.45E-01

Bibliography

[1] R. Singh, G. Ameyugo, and F. Noppel. *Jet engine design drivers: past, present and future*. Woodhead Publishing Limited, 2012.

[2] F. B. Metzger. A review of propeller noise prediction methodology: 1919-1994. Technical Report June, 1995.

[3] B. Marinus. *Multidisciplinary Optimization of Aircraft Propeller Blades*. PhD thesis, University de Lyon, 2011.

[4] F. Farassat, M. Dunn, A. Tinetti, and D. Nark. Open Rotor Noise Prediction Methods at NASA Langley: A Technology Review. 2009.

[5] O. Gur and A. Rosen. Multidisciplinary Design Optimization of a Quiet Propeller. 3073(May):5–7, 2008.

[6] A. Pagano, L. Federico, M. Barbarino, F. Guida, and M. Aversano. Multi-Objective Aeroacoustic Optimization of an Aircraft Propeller. (September):1–14, 2008.

[7] S. Burger. Multi-Fidelity Aerodynamic and Aeroacoustic Sensitivity Study and Design Optimisation Of Modern Propellers. *Literature Study, TU Delft*, 2019.

[8] A. Rosen and O. Gur. Novel approach to axisymmetric actuator disk modeling. *AIAA Journal*, 46(11):2914–2925, 2008.

[9] T. Sinnige, T. C. A. Stokkermans, D. Ragni, G. Eitelberg, and L. L. M. Veldhuis. Aerodynamic and Aeroacoustic Performance of a Propeller Propulsion System with Swirl-Recovery Vanes. *Journal of Propulsion and Power*, 34(6):1376–1390, 2018.

[10] E. Branlard, K. Dixon, and M. Gaunaa. An improved tip-loss correction based on vortex code results. In *European Wind Energy Conference and Exhibition 2012, EWEC 2012*, volume 2, pages 1079–1087, 2012.

[11] O. Gur and A. Rosen. Comparison between blade-element models of propellers. *Aeronautical Journal*, 112(1138):689–704, 2008.

[12] S. Hickel. AE4202 CFD for Aerospace Engineering - Lecture 06 LES, TU Delft, 2019.

[13] B. Sanderse, S. P. van der Pijl, and B. Koren. Review of computational fluid dynamics for wind turbine wake aerodynamics. *John Wiley & Sons, Ltd*, (December 2009):135–149, 2011.

[14] S. E. Kim and S. H. Rhee. Efficient engineering prediction of turbulent wing tip vortex flows. *CMES - Computer Modeling in Engineering and Sciences*, 62(3):291–309, 2010.

[15] T. C. A. Stokkermans, N. van Arnhem, T. Sinnige, and L. L. M. Veldhuis. Validation and Comparison of RANS Propeller Modeling Methods for Tip-Mounted Applications. *AIAA Journal*, 57(2):566–580, 2018.

[16] B. Magliozzi, D. B. Hanson, and R. K. Amiet. Propeller and Propfan Noise. *Aeroacoustics of Flight Vehicles: Theory and Practice. Volume 1: Noise Sources*, 1:1–64, 1991.

[17] W. M. Dobrzynski, H. H. Weller, J. O. Powers, and J. E. Densmore. Propeller Noise Tests in the German-Dutch Wind Tunnel DNW Executive Data Report. *DFVLR/FAA*, 1986.

[18] Inc. ANSYS. ANSYS Fluent Theory Guide. *Release 15.2*, 15317(November):373–464, 2015.

[19] F. Farassat. Report Moving Bodies With an Application To Helicopter Rotors. *NASA*, (December), 1975.

[20] F. Farassat. Derivation of Formulations 1 and 1A of Farassat. *NASA*, NASA/TM-20(March):1–25, 2007.

[21] C. J. Miller and J. P. Sullivan. Noise Constraints Effecting Optimal Propeller Designs (Technical Memorandum 105369). *NASA Technical Memorandum*, 86967, 1985.

[22] C. F. Wisniewski, A. R. Byerley, W. H. Heiser, K. W. Van Treuren, and W. R. Liller. Designing small propellers for optimum efficiency and low noise footprint. *33rd AIAA Applied Aerodynamics Conference*, (June):1–16, 2015.

[23] D. Ingraham, J. Gray, and L. V. Lopes. Gradient-based propeller optimization with acoustic constraints. *AIAA Scitech 2019 Forum*, (January):1–12, 2019.

[24] P. Yu, J. Peng, J. Bai, X. Han, and X. Song. Aeroacoustic and aerodynamic optimization of propeller blades. *Chinese Journal of Aeronautics*, 33(3):826–839, 2020.

[25] J. S. Carlton. Theoretical methods – propeller theories. In *Marine Propellers and Propulsion*, pages 168–204. Elsevier, 2007.

[26] M. K. Rwigema. Propeller Blade Element Momentum Theory with Vortex Wake Deflection. *International Congress of the Aeronautical Sciences*, pages 1–9, 2010.

[27] S. Hickel. AE4202 CFD for Aerospace Engineering - Lecture 03 Grid Generation, TU Delft, 2019.

[28] Inc. ANSYS. White Paper ANSYS Fluent Mosaic Technology Automatically Combines Disparate Meshes with Polyhedral Elements for Fast. pages 1–8.

[29] H. Schlichting and K. Gersten. *Boundary-Layer Theory*. Springer Berlin Heidelberg, Berlin, Heidelberg, ninth edit edition, 2017.

[30] L. Eça and M. Hoekstra. Discretization Uncertainty Estimation based on a Least Squares version of the Grid Convergence Index. *Proceedings of the Second Workshop on CFD Uncertainty Analysis, Instituto Superior Tecnico, Lisbon, Oct*, (February):1–27, 2006.

[31] D. B. Hanson. Unified Aeroacoustics Analysis for High Speed Turboprop Aerodynamics and Noise. Technical report, NASA, 1991.

[32] D. B. Hanson. Helicoidal Surface Theory for Harmonic Noise of Propellers in the Far Field. *AIAA Journal*, 18(10):1213–1220, 1980.

[33] A. Parry and D. Crighton. Theoretical prediction of counter-rotating propeller noise. *University of Leeds*, 1988.

[34] A. J. Keane and P. B. Nair. *Computational Approaches for Aerospace Design*. 2005.

[35] L. Zhang, J. Zhang, T. Li, and Y. Zhang. Multi-objective aerodynamic optimization design of high speed train head shape. 18(11):841–854, 2017.

[36] N. M. Urban and T. E. Fricker. A comparison of Latin hypercube and grid ensemble designs for the multivariate emulation of an Earth system model. *Computers and Geosciences*, 36(6):746–755, 2010.

[37] A. Singhee and R. A. Rutenbar. Why quasi-Monte Carlo is better than Monte Carlo or Latin hypercube sampling for statistical circuit analysis. *IEEE Transactions on Computer-Aided Design of Integrated Circuits and Systems*, 29(11):1763–1776, 2010.

[38] K. Mizzi, Y. K. Demirel, C. Banks, O. Turan, P. Kaklis, and M. Atlar. Design optimisation of Propeller Boss Cap Fins for enhanced propeller performance. *Applied Ocean Research*, 62:210–222, 2017.

[39] M. G. Fernández-Godino, C. Park, N. Kim, and R. T. Haftka. Review of multi-fidelity models. *Cornell University*, 9 2016.

[40] A. Amrit, L. Leifsson, and S. Koziel. Multi-fidelity aerodynamic design trade-off exploration using point-by-point Pareto set identification. *Aerospace Science and Technology*, 79:399–412, 2018.

[41] Sergios Theodoridis and Konstantinos Koutroumbas. *Pattern Recognition*. Elsevier Inc., 2009.

[42] K. C. Giannakoglou, D. I. Papadimitriou, and I. C. Kampolis. Aerodynamic shape design using evolutionary algorithms and new gradient-assisted metamodels. *Computer Methods in Applied Mechanics and Engineering*, 195(44-47):6312–6329, 2006.

[43] J. Martin and T. Simpson. A Monte Carlo Simulation of the Kriging Model. (September):1–16, 2012.

[44] M. A. Bouhlel, J. T. Hwang, N. Bartoli, R. Lafage, J Morlier, and J. R. R. A. Martins. A python surrogate modeling framework with derivatives. *Advances in Engineering Software*, page 102662, 2019.

[45] T. Sinnige. *Aerodynamic and Aeroacoustic Interaction Effects for Tip-Mounted Propellers*. PhD thesis, Delft University of Technology, 2018.

[46] J. E. Marte and D. W. Kurtz. A Review of Aerodynamic Noise From Propellers, Rotors, and Lift Fans. Technical report, NASA, 1970.